arXiv:1206.0772v2 [astro-ph.HE] 6 Jun 2012

THE STAR-FORMING GALAXY CONTRIBUTION TO THE COSMIC MeV AND GeV GAMMA-RAY BACKGROUND

BRIAN C. LACKI[1,2,3,4], SHUNSAKU HORIUCHI[4,5], AND JOHN F. BEACOM[3,4,5]

Draft version March 6, 2013

ABSTRACT

While star-forming galaxies could be major contributors to the cosmic GeV γ-ray background, they are expected to be MeV-dim because of the "pion bump" falling off below ~ 100 MeV. However, there are very few observations of galaxies in the MeV range and other emission processes could be present. We investigate the MeV background from star-forming galaxies by running one-zone models of cosmic ray populations, taking into account the leptonic emission, including Inverse Compton and bremsstrahlung, as well as nuclear lines (including ^{26}Al), emission from core collapse supernovae, and positron annihilation emission, in addition to the pionic emission. We use the Milky Way and the GeV–TeV detected starbursts M82 and NGC 253 as templates of normal and starburst galaxies, and compare our models to radio and GeV–TeV γ-ray data. We find that (1) Inverse Compton losses off the CMB flatten out the pion bump at high z for normal galaxies, (2) we cannot rule out that starbursts have significant MeV emission if their magnetic field strengths are low, and (3) cascades can contribute to the MeV emission of starbursts if they emit mainly hadronic γ-rays. The star-forming galaxy contribution to the GeV background is uncertain by an order of magnitude, depending on how much of the cosmic star-formation is in starbursts. Our fiducial model predicts that $\sim 1/3$ of the unresolved GeV background is from star-forming galaxies, with comparable contributions from normal and starburst galaxies. About $\sim 2\%$ of the claimed 1 MeV background is diffuse emission from star-forming galaxies; we place a firm upper limit of $\sim 10\%$ contribution based on the requirement that star-forming galaxies do not overpower the observed γ-ray background at any energy. The low star-forming galaxy contribution arises because the observed γ-ray background spectrum is steeply falling with energy, while the star-forming contribution is slowly increasing with energy in the MeV range. A different source class must emit the observed MeV background, if it is real.

Subject headings: gamma rays: diffuse background – gamma rays: galaxies – cosmic rays – galaxies: starburst

1. INTRODUCTION

The origin of the cosmic γ-ray background (Figure 1) remains a mystery. The unresolved extragalactic γ-ray background appears to have a single power law spectrum extending from ~ 50 MeV to 100 GeV, as determined from EGRET and *Fermi*-LAT (Sreekumar et al. 1998; Strong et al. 2004a; Abdo et al. 2010a). There has been much recent debate about the origin of this emission, particularly whether it comes from blazars or star-forming galaxies. The calculated blazar contribution (dominated by the soft Flat Spectrum Radio Quasars at low energies and the hard BL Lacs at high energies; Pavlidou & Venters 2008; Venters & Pavlidou 2011) has a similar spectrum to the γ-ray background and, if they make up most of the unresolved background, the remaining blazars should be resolved fairly easily (Abazajian et al. 2011). Star-forming galaxies are expected to have a "bump" in their emission at around a GeV, because most of their γ-ray emission comes from pion production by cosmic ray protons with a threshold of a few hundred MeV (Prodanović & Fields 2004). In contrast to blazars, very few star-forming galaxies will be resolved with *Fermi* (Pavlidou & Fields 2001). The contribution of both source classes at GeV energies is still unclear. The MeV background potentially is a powerful way of discriminating the two sources: the SED of blazars is expected to be higher at MeV energies, while the SED of star-forming galaxies is expected to be lower (e.g., Stecker & Venters 2011).

At GeV energies, *Fermi* has found that the unresolved extragalactic γ-ray background is a power law $dN/dE \propto E^{-2.41}$ (Abdo et al. 2010a). Before *Fermi*, the GeV γ-ray background was usually attributed to blazars, which dominate the population of detected γ-ray sources (Padovani et al. 1993; Stecker et al. 1993; Salamon & Stecker 1994; Stecker & Salamon 1996; Mücke & Pohl 2000). Abdo et al. (2010b) claim that the *Fermi* source counts are inconsistent with a blazar origin of the unresolved GeV background, although this conclusion has been disputed (Stecker & Venters 2011; compare with Singal et al. 2011 and Malyshev & Hogg 2011), and some estimates find that blazars are a minority of the unresolved GeV background (Dermer 2007; Inoue & Totani 2009). Studies of blazars detected in the flux-limited Australia Telescope 20 GHz survey also find that these blazars contribute a minority of the GeV background, based on an observed γ-ray–radio correlation (Ghirlanda et al. 2011) and *Fermi* image stacking of GeV undetected blazars (Zhou et al. 2011). Other proposed alternatives to a blazar origin for the GeV γ-ray background include dark matter annihilation and decay (e.g., Bergström et al. 2001; Ullio et al. 2002; Bertone et al. 2007), intergalactic shocks (Loeb & Waxman 2000; Miniati 2002; Keshet et al. 2003), non-blazar AGNs (Active Galactic Nuclei; e.g., Inoue 2011a; Teng et al. 2011), galaxy clusters (Dar & Shaviv 1995; Colafrancesco & Blasi 1998), cascades from ultrahigh energy cosmic rays (e.g., Wdowczyk et al. 1972; Coppi & Aharonian 1997; Murase et al. 2012), cosmic

---

[1] Jansky Fellow of the National Radio Astronomy Observatory
[2] Institute for Advanced Study, Einstein Drive, Princeton, NJ 08540, USA; brianlacki@ias.edu
[3] Department of Astronomy, The Ohio State University, 140 West 18th Avenue, Columbus, OH 43210, USA
[4] Center for Cosmology & Astro-Particle Physics, The Ohio State University, Columbus, Ohio 43210, USA
[5] Department of Physics, The Ohio State University, 191 W. Woodruff Avenue, Columbus, OH 43210, USA

rays accelerated by type Ia supernovae (Lien & Fields 2012), and Galactic foreground emission from millisecond pulsars (Faucher-Giguère & Loeb 2010), cosmic rays in the Galactic corona (Feldmann et al. 2012), and unsubtracted diffuse emission (Keshet et al. 2004; Malyshev & Hogg 2011).

Star-forming galaxies are also expected to contribute to the GeV γ-ray background. Supernovae and other processes accelerate cosmic rays (CRs), particularly protons but also other nuclei and electrons; these CRs can then interact with the ambient gas, radiation, and magnetic fields to emit broadband radiation. EGRET only detected the Milky Way and the LMC (Abdo et al. 2010c), but *Fermi* has also detected the SMC (Abdo et al. 2010d), M31 (Abdo et al. 2010e), and the starburst galaxies M82 and NGC 253 (Abdo et al. 2010f), as well as the starburst-Seyferts NGC 4945 and NGC 1068 (Abdo et al. 2010g; Lenain et al. 2010). The TeV telescopes VERITAS (Very Energetic Radiation Imaging Telescope Array System) and HESS (High Energy Stereoscopic System) have also detected M82 and NGC 253 (Acciari et al. 2009; Acero et al. 2009). The GeV emission is thought to come from the inelastic collisions of cosmic ray protons with protons in the interstellar medium (ISM), creating pions which in turn decay into γ-rays, neutrinos, and secondary electrons and positrons. Leptonic processes, particularly Inverse Compton (IC) and bremsstrahlung, may also contribute at lower energies. The sheer number of normal star-forming galaxies indicates that they contribute to the γ-ray background, even though they are individually faint, with pre-*Fermi* estimates placing the contribution anywhere from a few percent to most of the GeV background (Strong et al. 1976; Lichti et al. 1978; Pavlidou & Fields 2002).

A special subset of star-forming galaxies are the less numerous but individually luminous starburst galaxies, which have high star-formation rates and thus high CR energy densities. The high gas densities can enhance the pionic γ-ray emission from starbursts (Torres et al. 2004) so that they are a major component of the GeV γ-ray background (Thompson, Quataert, & Waxman 2007; see also Loeb & Waxman 2006). It is even possible that starbursts are "proton calorimeters", converting the power injected as CR protons into pionic losses (Pohl 1994; Loeb & Waxman 2006; Thompson, Quataert, & Waxman 2007; Lacki et al. 2010), but the extent to which this is true is disputed (Acero et al. 2009; Lacki et al. 2011; Ohm & Hinton 2012), as is the fraction of star-formation in calorimetric galaxies (Stecker 2007; Thompson et al. 2006b; Stecker & Venters 2011). Recent estimates of the star-formation contribution to the GeV γ-ray background find values ranging from 10% to 50% (e.g., Bhattacharya & Sreekumar 2009; Fields et al. 2010; Makiya et al. 2011; Stecker & Venters 2011), with starbursts alone making up 1% to 50% of the GeV γ-ray background (Makiya et al. 2011; Lacki et al. 2011; Stecker & Venters 2011).

Although *Fermi* continues to advance our understanding of the GeV γ-ray sky, very little is known about the MeV γ-ray background. The available data on the MeV background comes from Solar Maximum Mission (SMM; 0.3 - 7 MeV; Watanabe et al. 1999), Imaging Compton Telescope (COMPTEL; 1 - 20 MeV; Weidenspointner et al. 2000), and Energetic Gamma Ray Experiment Telescope (EGRET; 30 - 20000 MeV; Sreekumar et al. 1998; Strong et al. 2004a). Blazars may constitute most of the MeV background (Bloemen et al. 1995; Zdziarski 1996; Giommi et al. 2006; Ajello et al. 2009). Additionally, γ-ray line emission and the accompanying Compton-downscattered continuum emission from type Ia supernovae is expected to contribute (Clayton & Silk 1969; Clayton & Ward 1975; The et al. 1993; Ruiz-Lapuente et al. 2001), but more recent estimates show that supernovae account for only $\sim$ 10% of the MeV background (Iwabuchi & Kumagai 2001; Strigari et al. 2005; Ahn et al. 2005; Horiuchi & Beacom 2010). Other proposed sources include nonthermal electrons in AGN coronae (Inoue et al. 2008), the cores of misaligned radio loud AGNs (Inoue 2011a), the radio lobes of AGNs (Massaro & Ajello 2011), dark matter decay (Olive & Silk 1985), and dark matter annihilation (Ahn & Komatsu 2005). It is not even clear that the observed background is real; it could be caused by detector backgrounds (e.g., caused by incident CRs or radioactive decays in the satellite).

Not only the normalization but the spectral shape of the MeV background is mysterious. We plot energy flux per natural log energy bin in Figure 1 and similar figures; the area under a curve in an energy range in these figures is directly proportional to the power coming out within that energy range[6]. It is clear that the MeV background represents more power than the GeV background. Furthermore, there are spectral breaks at $\sim$ 3 MeV and $\sim$ 20 MeV with unknown origin.

We present here constraints and estimates of the star-forming galaxy contribution to the γ-ray background, with an emphasis on the MeV background. Soltan & Juchniewicz (1999) first suggested that starburst galaxies contribute to the MeV background through their IC emission, by scaling the IC emission from the observed synchrotron radio emission, assuming that starburst magnetic fields were the same as in the Milky Way (see also Soltan & Marcinkowski 2001). Most of the other estimates of the γ-ray background focus on pionic emission above 100 MeV; to the extent that leptonic emission is considered, the Milky Way spectrum is typically assumed. In the meantime, there have been a number of models of the γ-ray emission from NGC 253, M82, and Arp 220 that take into account radio observations (Paglione et al. 1996; Torres 2004; Domingo-Santamaría & Torres 2005; Persic et al. 2008; de Cea del Pozo et al. 2009a; Rephaeli et al. 2009; Lacki et al. 2010). On the observational side, studies of the MeV emission from star-forming galaxies and starbursts in particular are hampered by the very low sensitivity of current MeV instruments. Only weak constraints have been set on the MeV emission from starburst galaxies with OSSE and INTEGRAL (Bhattacharya et al. 1994; Dermer et al. 1997). We model the MeV emission for starburst and normal galaxies, and use the spectral shape to constrain the star-forming galaxy contribution to the MeV background.

In Section 2, we review the MeV emission processes of star-forming galaxies. In Section 3, we present one-zone models of the Milky Way, M82, and NGC 253 that serve as templates for our γ-ray background calculation. In Section 4, we consider the effects of $\gamma\gamma$ cascades in the intergalactic medium on the shape of star-forming galaxy spectra. In Section 5 we present our results for the star-formation contribution to the MeV background, both the calculation of the MeV background and constraints from the spectral shape. We assume $\Omega_M = 0.25$, $\Omega_\Lambda = 0.75$, and $H_0 = 70$ km s^{-1} Mpc^{-1}.

2. REVIEW OF MeV EMISSION PROCESSES

---

[6] Since $\nu I_\nu = E^2 dN/dE = E dN/d\ln E$, the area under the curve as plotted is $\propto \int \nu I_\nu d\ln E = \int E^2 dN/dE d\ln E = \int E dN/dE dE$.

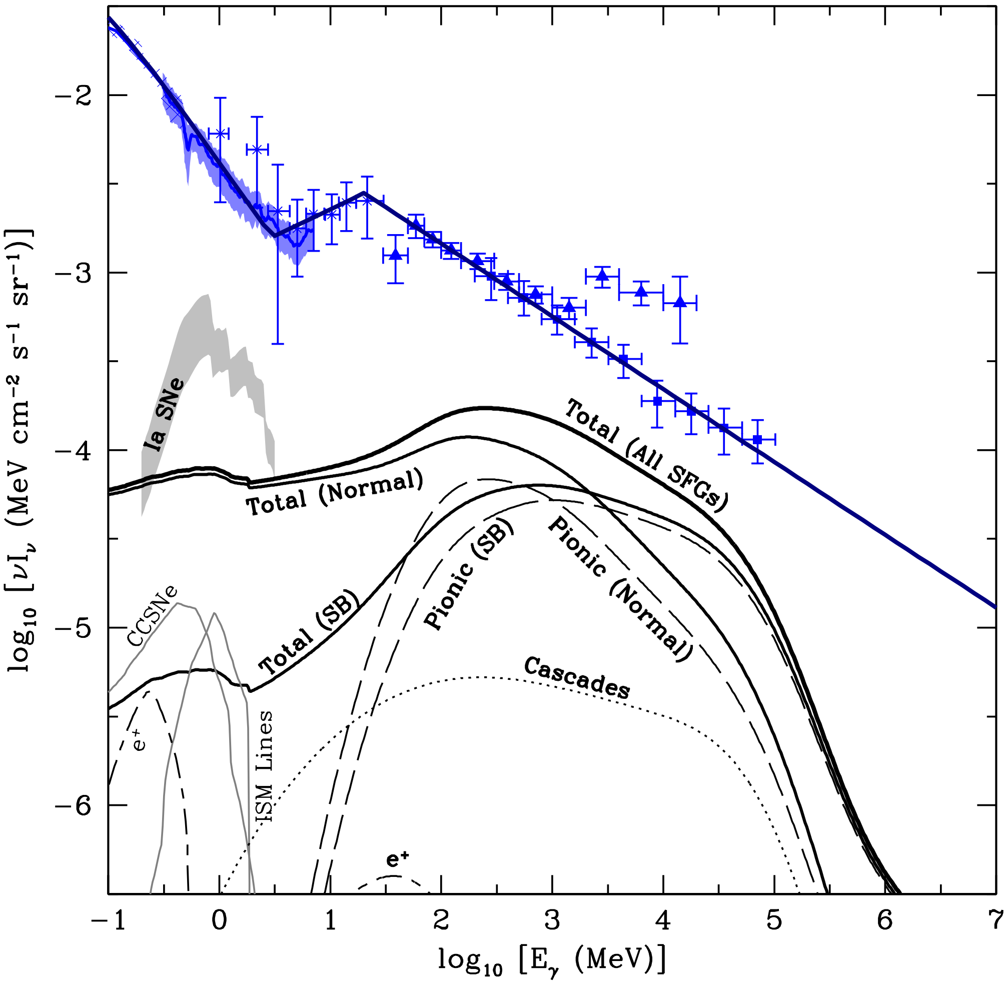

FIG. 1.— The observed unresolved extragalactic γ-ray background (blue) and the predicted γ-ray background from star-forming galaxies with our standard assumptions. Plotted data include the compilation in Gilli et al. (2007) (cross-hatching), SMM (shading), COMPTEL (X's), EGRET (triangles), and *Fermi*-LAT (squares). We show the total predicted background from star-forming galaxies (black, thick solid), the total background from normal galaxies (black solid line, higher at MeV), and the total background from starbursts (black solid line, higher at 100 GeV). We also show various components of the γ-ray background, including the pionic emission (long-dashed) from starbursts and normal galaxies, positron annihilation radiation (long-dashed/short-dashed), nucleosynthetic γ-ray lines and radiation from CCSNe (grey solid), and cascade emission (from starbursts only; dotted). The separate contributions from IC and bremsstrahlung contribution are not shown, but they make up most of the difference between the total and pionic emission. For comparison, the MeV background from type Ia supernovae from Horiuchi et al. (2011) is shown as grey shading. Our fiducial model for the Milky Way is the $h = 2000$ pc single zone model; for starbursts we use the M82 $B = 300\ \mu$G model; and we assume that 15% of the cosmic star-formation rate at all redshifts is in starbursts. However, the actual starburst fraction is highly uncertain and can affect the results at the order of magnitude level.

At MeV energies, corresponding to temperatures $\gtrsim 10^{10}$ K, there are essentially no diffuse, thermal emission processes that can contribute to the γ-ray background. MeV emission from star-forming galaxies therefore either (1) involve non-thermal cosmic rays, or (2) directly comes from nuclear reactions, and sometimes both. We review the known MeV emission processes that correlate with star-formation here.

2.1. *Leptonic CR Emission*

Most of the observed γ-ray emission from galaxies comes from CRs. The GeV-TeV emission is probably pionic, because the injection rate of CR protons exceeds that of the primary CR electrons by a factor $\sim 50-100$ at GeV energies in the Milky Way. Even weak pionic losses as in the Milky Way are sufficient to overwhelm the leptonic emission at these energies (e.g., Strong et al. 2010). However, the kinematics of the pion production process leads to a rapid decline in the pionic luminosity below ~ 100 MeV (the "pion bump"), below which leptonic CR emission dominates. At a minimum, secondary $e^\pm$ accompany pionic γ-rays; their leptonic emission can flatten out the pion bump (Schlickeiser 1982).

Inverse Compton (IC) emission – Inverse Compton arises when a CR $e^\pm$ Compton scatters an ambient photon, boosting its energy in the observer frame. The IC emission is expected to form a broad continuum, because the upscattered photon energy scales as the square of the electron energy (in the Thomson limit). It likely dominates the Milky Way non-thermal continuum at 100 keV (Porter et al. 2008). Below the Klein-Nishina cutoff, electrons of energy E_e will typically upscatter photons of energy ϵ to $4\epsilon E_e^2/(3m_e c^2)^2$. Ambient photons can come from the CMB, far-infrared (FIR) emission from dust, or stellar UV/optical/infrared backgrounds; in the Milky Way, these all have similar energy densities, while in starburst galaxies, the FIR emission dominates. Each of the radiation fields are roughly greybody fields with a temperature T and average photon energy $\sim 2.7kT$.

Therefore typical upscattered photon energies are $E_{\rm IC}^{\rm CMB} \approx 0.32(1+z)E_{10}^2$ MeV, $E_{\rm IC}^{\rm FIR} \approx 2.4(T_{\rm FIR}/20\ {\rm K})E_{10}^2$ MeV, and $E_{\rm IC}^{\rm opt} \approx 480\ {\rm MeV}(T_{\rm opt}/4000\ {\rm K})E_{10}^2$ MeV for electrons of energy $10E_{10}$ GeV upscattering the CMB, FIR, and optical radiation fields. IC from each of the components is expected to have a $\Gamma = \mathcal{P}/2 + 1/2 \approx 2.0 - 2.2$ photon index, if the CR $e^{\pm}$ have a steady-state power law spectrum $E^{-\mathcal{P}}$.

The CMB energy density grows rapidly with redshift. IC upscattering off a strong high-z CMB can take energy away from other cooling processes, essentially quenching the radio luminosity of a galaxy and transferring the power into MeV emission (Carilli & Yun 1999; Murphy 2009). At high energies, the CMB must overcome the Inverse Compton losses off the starlight and the synchrotron losses in the magnetic field. Thus, this effect is only important when $U_{\rm CMB} \gtrsim U_B$, or

$$B \lesssim 3.2\ \mu{\rm G}\ (1+z)^2. \qquad (1)$$

In Milky Way-like galaxies with $B \approx 6 - 10\ \mu$G and starlight energy density $U_{\star} \approx U_B$, the CMB overwhelms the other losses before $z \approx 1$. However, in starburst galaxies with $B \gtrsim 100\ \mu$G, the CMB remains unimportant out to $z \gtrsim 5$. At low electron energies, escape, bremsstrahlung, and ionization losses "buffer" the radio spectrum against the CMB effect to even higher redshift (Lacki & Thompson 2010a).

Finally, CR $e^{\pm}$ can escape into the halos of galaxies, where they cool by Inverse Compton emission. Indeed, Strong et al. (2010) find that about $\sim 30 - 60\%$ of the power injected into CR electrons in the Milky Way is lost to Inverse Compton cooling, with greater IC luminosities for larger halos. The majority of this emission is below 100 MeV in most of their models, although the total ≤ 100 MeV emission is still about a third or less of the total γ-ray emission (Strong et al. 2010). Starburst galaxies are expected to be "electron calorimeters", with most of the $e^{\pm}$ cooling in the starburst disk proper (e.g., Völk 1989), but radio haloes are observed in starbursts, indicating that some CR $e^{\pm}$ reach large heights off the plane (Seaquist & Odegard 1991). We do not consider these haloes further in this work.

Bremsstrahlung – Bremsstrahlung radiation is emitted by CR $e^{\pm}$ when they are deflected by the electric field of a nucleus. A typical bremsstrahlung photon has half the energy of the CR $e^{\pm}$ (Schlickeiser 2002); thus the bremsstrahlung spectrum has the same shape as the CR $e^{\pm}$ spectrum, which is set by the dominant cooling or escape mechanism for CR $e^{\pm}$. The bremsstrahlung loss time of an $e^{\pm}$ with energy $E_{\rm GeV}$ GeV traversing pure hydrogen of number density n is $t_{\rm brems} \approx 40$ Myr $(n/{\rm cm}^{-3})^{-1}$, but the ionization loss time is $t_{\rm ion} \approx 1380$ Myr $E_{\rm GeV}(n/{\rm cm}^{-3})^{-1}[\ln E_{\rm GeV} + 14.4]^{-1}$ where $E_{\rm GeV} = E/{\rm GeV}$ (Strong & Moskalenko 1998). Thus ionization losses therefore quickly softens both the CR $e^{\pm}$ and bremsstrahlung emission spectrum below ~ 400 MeV, independent of density. Likewise, IC and synchrotron losses harden the CR $e^{\pm}$ spectrum at high energies, since they go as $t \propto E^{-1}$. The result is a "bremsstrahlung bump" peaking at a few hundred MeV, where the energy-independent bremsstrahlung losses are most important. Thus, leptonic emission may itself be peaked near 100 MeV, even without hadronic emission. A low energy bremsstrahlung tail can be generated only if the injected electron spectrum is very steep (e.g., Sacher & Schoenfelder 1983).

Synchrotron and other emission from TeV-PeV $e^{\pm}$ – Synchrotron emission from CR $e^{\pm}$ deflected in a galaxy's magnetic field is responsible for the low frequency radio emission of galaxies, but it can also extend to X-rays and γ-rays. At MeV-emitting energies, there are few $e^{\pm}$ injected, but there are no competing cooling processes (IC is suppressed by Klein-Nishina effects). The typical energy of synchrotron photons is 1.2 MeV$E_{\rm PeV}^2 B_{10}$, where $E_{\rm PeV}$ is the $e^{\pm}$ energy in PeV and $B_{10} = B/(10\ \mu G)$ is the magnetic field strength. In the Milky Way, the low magnetic field strength combined with the lack of IC emission observed at $\sim$ PeV energies implies that there is little large scale high-energy synchrotron emission (Aharonian & Atoyan 2000). The magnetic fields of starbursts are constrained to be much higher in starbursts like those in M82 and NGC 253 ($\sim 100 - 300\ \mu$G; e.g., Thompson et al. 2006a; de Cea del Pozo et al. 2009b), so that synchrotron may be important at X-ray (Lacki & Thompson 2010b) and perhaps γ-ray energies. Synchrotron has a photon index of $\Gamma \gtrsim 2.0$, steepening greatly at the tail of the CR $e^{\pm}$ spectrum.

TeV CR $e^{\pm}$ deflected in electrostatic waves will also emit MeV radiation through electrostatic bremsstrahlung, which occurs at higher frequencies for electrons of a given energy (Schröder et al. 2005). The typical electrostatic bremsstrahlung photon energy for an electron of Lorentz factor γ is $\gamma^2\nu_P$ compared to the synchrotron photon energy of $\gamma^2\nu_B$, where ν_P is the plasma frequency, ν_B is the cyclotron frequency, and typically $\nu_P \gg \nu_B$. However, electrostatic bremsstrahlung is only important if the energy density in electrostatic waves reaches the magnetic energy density; since this is not known, we ignore the process for the rest of the work.

2.2. *Positron Annihilation*

Nearly thermalized positrons can annihilate with ISM electrons into 511 keV photons, or they can form positronium atoms which can emit 3-photon annihilation continuum at energies below 511 keV as well as 511 keV photons. A bright source of annihilation radiation is detected from the Galactic Center bulge, with a flux and spatial distribution not consistent with star formation (Weidenspointner et al. 2008a), but additional positron emission is detected from the Galactic disk (Weidenspointner et al. 2008b). The positron generation rate in the Galactic disk is consistent with a nucleosynthetic origin in the fission of isotopes like ^{26}Al produced by massive stars (e.g., Prantzos et al. 2011). We consider this star-formation component of positrons, but not the (dominant in the Milky Way) bulge source of positrons in this paper.

In addition, CR positrons can annihilate while they are still relativistic (in-flight annihilation or IA), although most CR positrons survive to rest. Pionic positrons, produced alongside pionic γ-rays, are injected at energies $\gtrsim 100$ MeV (Beacom & Yüksel 2006). If we approximate the hadronic positron injection spectrum as $Q(E) = Q_0\delta(E - E_0)$ where $E_0 \approx 100$ MeV, and since e^{+} are cooled primarily by ionization (which has a cooling rate roughly independent of energies) at $E \lesssim E_0$, the steady-state low-energy hadronic positron spectrum should have a nearly constant dN/dE. It can then be shown that the annihilation radiation from hadronic positrons is hard, with $dN_{\gamma}/dE \propto E^{-1}(\ln(2\gamma) - 1)$ (Aharonian 2004), so that $\nu L_{\nu} \sim E^2 dN_{\gamma}/dE \propto E(\ln(2\gamma) - 1)$ peaks near 100 MeV.

Watanabe et al. (1999) calculated the 511 keV line contribution to the γ-ray background, but did not include positronium continuum or inflight annihilation.

2.3. *Nuclear γ-Ray Lines*

Nucleosynthetic ISM γ-ray lines – Some radioactive isotopes synthesized in young, massive stars emit nuclear γ-rays when they decay. The ^{26}Al decay line at 1.809 MeV is the brightest γ-ray line above 1 MeV detected from the Galactic plane (Mahoney et al. 1984; Diehl et al. 1995, 2006a). The spatial distribution of the line is correlated with massive star-formation in the Galaxy, including individual star-forming regions such as Cygnus (del Rio et al. 1996; Knödlseder et al. 1999; Diehl et al. 2006a), although older sources may contribute ^{26}Al to the ISM. The only other detection of γ-ray lines above 1 MeV from the diffuse Galaxy are the ^{60}Fe decay lines at 1.173 and 1.333 MeV (Harris et al. 2005; Wang et al. 2007). However, the 1.157 MeV ^{44}Ti γ-ray line has been detected from the Cas A supernova remnant. The injection sites of ^{26}Al and ^{60}Fe are thought to be supernovae with some contribution from Wolf-Rayet star winds (e.g., Knödlseder 1999; Palacios et al. 2005; Limongi & Chieffi 2006), so their yields should scale with massive star-formation rate. However, some processes in old stellar populations, particularly novae, may also synthesize isotopes that emit γ-ray lines (e.g., Jose et al. 1997).

Gamma-ray lines from nuclear decay in the ISM are narrow; Galactic observations of the ^{26}Al line constrain line widths to be less than $\sim$ 3 keV (Diehl et al. 2006b), but the line emission from a redshift distribution of galaxies will be smeared out into a continuum.

The MeV background from these lines was also calculated in Watanabe et al. (1999).

Core collapse supernovae – In addition to the long-lasting radioisotopes visible in the ISM, core collapse supernovae (CCSNe) themselves glow in γ-rays from short-lived isotopes. The CCSNe are powered by the decay chain of ^{56}Ni into ^{56}Co (half-life of 6 days), and then ^{56}Co into ^{56}Fe (half-life of 78 days). Each decay can produce γ-ray lines. However, CCSNe are highly Compton-thick, especially at early times, which downgrades much of the line emission into weaker continuum emission (e.g., Gehrels et al. 1987; Arnett & Fu 1989; Ruiz-Lapuente et al. 2001).

The γ-ray yield and MeV background from CCSNe was calculated by Watanabe et al. (1999), Ruiz-Lapuente et al. (2001), and Iwabuchi & Kumagai (2001).

Besides core collapse supernovae, there will be γ-ray line emission from type Ia supernovae, some of which are "prompt" after the formation of the progenitors. In this sense, some of the type Ia supernova emission can be associated with star-formation. However, including this component would require a distribution of delay times of star-formation, which is beyond the scope of this paper. In any case, the most recent predictions for this background show that it is only $\sim$ 10% of the observed MeV background (Iwabuchi & Kumagai 2001; Strigari et al. 2005; Ahn et al. 2005; Horiuchi & Beacom 2010). We refer the reader to Horiuchi & Beacom (2010) for discussion of the MeV background from type Ia supernovae.

CR de-excitation lines – CRs can also emit γ-ray lines through nuclear interactions with nuclei in the ISM (e.g., Meneguzzi & Reeves 1975; Ramaty et al. 1979). In addition to narrow line components from the excitation of nuclei in the ISM, broader components are expected when CR nuclei themselves are excited. The strongest lines expected are the 4.438 MeV ^{12}C and 6.129 MeV ^{16}O de-excitation lines (e.g., Ramaty et al. 1979). For these lines, the broad component should actually be more luminous than the narrow lines, because CRs have much higher abundances of C and O relative to H and He than the ISM (e.g., Meyer et al. 1998).

CR-excited lines will be much fainter than the pionic emission unless there are many low energy CR nuclei, with only $0.01-0.1$ line $\sim$ MeV photon but $\sim$ 1 pionic photon per $\sim$ 100 MeV$/n$ nucleus if losses are unimportant (Parizot & Lehoucq 2002). A low energy component of CR nuclei, peaking at only a few MeV, is suggested by some CR ionization studies (e.g., Indriolo et al. 2009), but CR-excited nuclear lines have not been detected in the Galaxy (Teegarden & Watanabe 2006). A claimed detection of the 4.438 MeV and 6.129 MeV lines in the Orion star-forming region (Bloemen et al. 1994) later proved spurious (Bloemen et al. 1999).

2.4. *Emission from Discrete Sources*

Star-forming galaxies are unresolved spatially in γ-rays, except for the Milky Way and the Magellanic Clouds. However, in addition to the diffuse γ-ray emission, compact γ-ray sources as observed in the Milky Way may contribute to the total galactic γ-ray luminosity. Many of these sources – including supernova remnants, pulsar wind nebulae, and molecular clouds located near CR accelerators – are directly related to star-formation, and could increase the contribution of star-forming galaxies to the γ-ray background. A study by INTEGRAL indicates that at $\gtrsim$ 1 MeV, most of the Galactic emission is an unresolved diffuse component, unlike at lower energies where point sources dominate (Bouchet et al. 2008). However, given how poorly the MeV regime is understood even in the Milky Way, with even the advanced GALPROP models failing to account for all emission in the $\sim$ 30 MeV range (Strong et al. 2004b; Porter et al. 2008), it is possible that additional MeV emission will come from unresolved discrete sources (c.f., Strong et al. 2000b). We do not consider discrete sources further here, except to note them as a great uncertainty.

2.5. *Brief Summary*

Over much of the range a few hundred keV to a few hundred MeV, IC is expected to be the dominant emission process. This is because it forms a broad continuum; furthermore, both radiation fields and $e^{\pm}$ of the relevant energies (GeV–TeV) are known to be present in star-forming galaxies. Nonthermal bremsstrahlung may be important at $\sim$ 100 MeV, but it appears as a bump in the spectrum that subsides at lower energies. Line emission from CCSNe, positron annihilation, and ^{26}Al may be important from a few hundred keV to an MeV. The tail of the synchrotron spectrum also may be important at a few hundred keV, though its strength is highly uncertain.

3. MODELLING OF γ-RAY SPECTRA

To estimate the MeV - GeV background contribution from normal and starburst galaxies, we need to understand the γ-ray SED of star-forming galaxies – both the spectral shape and the normalization per unit star-formation. Since much of this emission is from CRs, this requires an understanding of CR populations in both normal and starburst galaxies. The CR population is governed by the diffusion-loss equation, which includes terms for CR injection, spatial propagation, cooling, and destruction (see Appendix). However, for the purposes of understanding other galaxies, we can reduce the complicated diffusion-loss equation into a one-zone leaky-box equation, which treats the galaxy (or its starburst core) as one region with an homogeneous environment and CR population.

There are very detailed models of the nonthermal broad-band spectrum of the Milky Way, particularly with the

GALPROP code (e.g., Strong et al. 2010), and several one-zone and 3D models of the starburst galaxies M82 and NGC 253 (Paglione et al. 1996; Domingo-Santamaría & Torres 2005; Persic et al. 2008; de Cea del Pozo et al. 2009a; Rephaeli et al. 2009; Lacki et al. 2011). However, these models use the present CMB; at high z, the strong CMB can increase Inverse Compton losses and change the broadband spectrum. In addition, these models generally do not include positron annihilation or nuclear lines. We therefore run our own models, using the Milky Way as a spectral template for normal galaxies, and M82 or the NGC 253 starburst as a spectral template for starbursts.

3.1. *Procedure for One-Zone Models*

We solve the steady-state, one zone CR propagation equation (leaky box model) using a Green's function described in Torres (2004), which we solve with a code described in Lacki et al. (2010). We include primary nuclei and $e^{\pm}$, secondary (knock-on and pionic) $e^{\pm}$, and higher order pair $e^{\pm}$ from $\gamma\gamma$ annihilation. Our procedure is largely the same as in Lacki & Thompson (2010b), although with several new features: we include positron annihilation, nuclei heavier than hydrogen (both in the primary CRs and the ISM), and nuclear de-excitation lines (as described in the Appendix).

We model star-forming galaxies as disks with radius R and midplane-to-edge scale heights h. The CR injection power is proportional to the supernova rate: a fraction $\eta \sim 0.1$ of the $10^{51} E_{51}$ ergs in supernova kinetic energy goes into primary protons, while a fraction $\xi \sim 0.01$ goes into primary electrons. For the starbursts, we relate the supernova rate directly to the TIR (total infrared: $8-1000\ \mu m$) luminosity, which should scale almost directly with star-formation rate:

$$\Gamma_{\rm SN}^{\rm SB} = 0.036\ {\rm yr}^{-1} \psi_{17} \left(\frac{L_{\rm TIR}}{10^{10.5}\ {\rm L}_{\odot}} \right), \qquad (2)$$

where $\psi_{17} = 1$ is an initial mass function (IMF) dependent constant (Thompson, Quataert, & Waxman 2007; Lacki & Thompson 2010b). Since massive stars dominate both the bolometric luminosity and the supernova rate, the supernova rate inferred from the luminosity should vary by only a few percent for different IMFs (Thompson, Quataert, & Waxman 2007). For the Milky Way, we relate the supernova rate to an assumed star-formation rate:

$$\Gamma_{\rm SN}^{\rm MW} = 0.0084\ {\rm yr}^{-1} \epsilon_{\rm SalA} \psi_{17} \left(\frac{\rm SFR}{{\rm M}_{\odot}\ {\rm yr}^{-1}} \right). \qquad (3)$$

where $\epsilon_{\rm SalA} = \epsilon/(4.9 \times 10^{-4})$ is a conversion between bolometric luminosity and star-formation rate corrected to a "Salpeter A" IMF (Kennicutt 1998; Baldry & Glazebrook 2003), as used for the cosmic star-formation rate in Hopkins & Beacom (2006).[7] From the supernova rate, we get the volumetric power injection for CR protons:

$$\epsilon_{\rm CR,p} = 10^{51} {\rm ergs}\ E_{51} \eta \Gamma_{\rm SN}/(2\pi R^2 h) \qquad (4)$$

and primary $e^{\pm}$:

$$\epsilon_{\rm CR,e} = 10^{51} {\rm ergs}\ E_{51} \xi \Gamma_{\rm SN}/(2\pi R^2 h) \qquad (5)$$

Primary CRs are injected with a $dQ/dq = Cq^{-p}$ power law spectrum, where q is momentum: this is the test-particle approximation, although nonlinear physics in acceleration may alter the injection spectrum at low energies (e.g., Berezhko & Ellison 1999; Ellison et al. 2000; Malkov & O'C Drury 2001; Blasi et al. 2005). The normalization for protons and $e^{\pm}$ is set by:

$$\epsilon_{\rm CR} = C \int_{q_{\rm min}}^{q_{\rm max}} q^{-p} (\sqrt{q^2 c^2 + m^2 c^4} - mc^2) dq, \qquad (6)$$

where m is the rest mass of the accelerated particle, $q_{\rm min}$ and $q_{\rm max}$ are the momenta corresponding to the minimum and maximum kinetic energy particles are injected with, and $\epsilon_{\rm CR}$ is the volumetric power injected in CRs of a given species. We use a minimum injection kinetic energy of 1 MeV; for the protons and nuclei, we use a maximum injection Lorentz factor of 10^6 ($K_{\rm max} \approx 1$ PeV), while for $e^{\pm}$, the maximum injection Lorentz factor is either 2×10^7 ($K_{\rm max} \approx 1$ TeV) for the Milky Way, or a free parameter for the starbursts. With these injection spectra, the ratio of dQ/dq for primary protons and electrons at energies $> m_p c^2$ is approximately:

$$\tilde{\delta} \equiv \frac{C_p}{C_e} \approx \delta \left(\frac{m_p c^2}{K_{\rm min}} \right)^{p-2}, \qquad (7)$$

which is known to be $\sim 50-100$ in the Milky Way (e.g., Ginzburg & Ptuskin 1976; Warren et al. 2005; Strong et al. 2010). The normalization for the nuclei are scaled using the Milky Way CR abundance ratios (see the Appendix).

We run models for hadronic-origin CRs (nuclei, pionic secondaries, and the radiation and $\gamma\gamma$ pair $e^{\pm}$ they generate) and leptonic-origin CRs (primary CR $e^{\pm}$ and the radiation and $\gamma\gamma$ pair $e^{\pm}$ they generate) separately, and scale them by η and ξ respectively. These components are then added together. Diffusive losses are applied to CRs of all species in both the Milky Way and starbursts. Advective losses are also applied in starbursts. CR nuclei experience catastrophic inelastic (including pionic) losses and continuous ionization cooling. CR electrons experience ionization, bremsstrahlung, synchrotron, and IC cooling; CR positrons experience these losses as well as catastrophic annihilation losses. We include secondary $e^{\pm}$ from knock-off processes and pion production in nucleus-nucleus collisions, as well as tertiary $e^{\pm}$ from $\gamma\gamma$ pair production. Secondary nuclei from collisions, however, are not included. We calculate the emission from pionic collisions (both γ-rays and neutrinos), synchrotron, positron annihilation, several of the strongest nuclear lines, IC, and bremsstrahlung. More technical details are given in the Appendix.

The propagated spectra depend on a number of parameters, many of which are poorly constrained in starburst galaxies. The GeV-TeV γ-ray emission, which is pionic in most of our models, constrains the proton acceleration efficiency η. The radio data constrains a combination of the electron acceleration efficiency ξ and B, but there is a degeneracy between these parameters (see the similar discussion in Lacki & Thompson 2010b; also see Persic et al. 2008, de Cea del Pozo et al. 2009a, and Rephaeli et al. 2009). With high B, few $e^{\pm}$ are needed to produce the observed GHz synchrotron radio emission, and the $e^{\pm}$ population in starbursts is dominated by hadronic secondaries. Models with Milky Way values for the proton/electron injection ratio have high B. Models with low B have large ξ and therefore large amounts of leptonic γ-ray emission in the MeV bands. In addition, the wind speed $v_{\rm wind}$, gas scale height h, primary electron cutoff $\gamma_{\rm max}^{\rm prim}$, and diffusive escape time $t_{\rm diff}(3\ {\rm GeV})$ can all influence the CR spectrum. Finally, we add a component of free-free emission with spectrum $S_\nu = S_{\rm ff}(1\ {\rm GHz})(\nu/1\ {\rm GHz})^{-0.1}$, which flattens out the radio spectrum.

---

[7] Hopkins & Beacom (2006) find that for a given bolometric luminosity, a "Salpeter A" IMF has only 77% of the star-formation rate of a standard Salpeter IMF from $0.1-100\ {\rm M}_{\odot}$ used in Kennicutt (1998).

To keep the number of spectral templates for the starbursts to a manageable level, we group models by B. We consider consider magnetic field strengths of 50, 100, 150, 200, 250, 300, and 400 μG for M82 and NGC 253's starburst. For each B, we minimize χ^2 for the sum of radio and γ-ray data for the parameters η, ξ, $v_{\rm wind}$, h, $\gamma_{\rm max}^{\rm prim}$, $S_{\rm ff}(1\ {\rm GHz})$, and $t_{\rm diff}(3\ {\rm GeV})$ (c.f. Crocker et al. 2011b) to select a best model for that B, for both primary electrons and an equal mix of primary electrons and positrons (listed in Table 1). In the Milky Way, most of the parameters are constrained by direct observations and we do not do χ^2 fitting.

To the total γ-ray spectra, we then add in the nucleosynthetic γ-ray lines. The 1.809 MeV line from ^{26}Al is scaled from its Milky Way luminosity using the supernova rate: $L_{1.809} = 1.7 \times 10^{37} {\rm ergs\ s^{-1}} (\Gamma_{\rm SN}/\Gamma_{\rm SN,MW})$ (Diehl et al. 2006a). In the Milky Way, the 1.173 and 1.333 MeV ^{60}Fe lines are observed to have 0.11 photon each for every photon of the 1.809 ^{26}Al lines (Harris et al. 2005). We therefore set $L_{1.173} = 0.11(1.173/1.809)L_{1.809}$ and $L_{1.333} = 0.11(1.333/1.809)L_{1.809}$. Finally, we scale the 1.157 MeV ^{44}Ti γ-ray line directly with the supernova rate: $L_{1.157} = 1.6 \times 10^{38} (M_{Ti-44}/10^{-4}\ {\rm M}_\odot)\ {\rm ergs\ s^{-1}} (\Gamma_{\rm SN}/{\rm yr}^{-1})$, where M_{Ti-44} is the yield of ^{44}Ti per supernova. The ^{44}Ti yield is controversial, because Cas A is bright in the line (Iyudin et al. 1994; see also Vink et al. 2001 for detections of associated X-ray lines) and SN 1987A's emission indicates large yields (e.g., Chugai et al. 1997; Fransson & Kozma 2002; Jerkstrand et al. 2011), but the Galaxy as a whole is faint in 1.157 MeV (The et al. 2006). We assume 10^{-4} M$_\odot$ per supernova, but estimated values range from $10^{-5} - 2 \times 10^{-4}$ M$_\odot$.

In addition, we run a one-zone model of nucleosynthetic e^+ from radioactive isotopes injected as a delta function at 1 MeV, scaled to the positron generation rate in the Galactic disk from Weidenspointner et al. (2008b): $(dQ/dE)_{\rm SN} = 8 \times 10^{42} {\rm s}^{-1} (\Gamma_{\rm SN}/\Gamma_{\rm SN,MW}) \delta(K - 1\ {\rm MeV})/(2\pi R^2 h)$. The γ-ray spectrum is then the sum of the emission from hadronic-origin CRs, the leptonic-origin CRs, the nucleosynthetic e^+, and the nucleosynthetic γ-ray lines.

When we have a best-fit model for each B and primary $e^\pm$ composition, we then use those same parameters run models at redshifts from 0.0 to 4.9 at intervals $\Delta z = 0.1$. The only alteration with redshift is that the radiation field is altered so that the CMB is increased to its value at each redshift. No other evolution of the spectrum shape of each class of galaxies (due to, e.g., increased gas fraction at high z) is considered. Instead, galaxy evolution is assumed only to convert galaxies from being starbursts at high z to normal at low z (see the extensive discussion in section 5.2), besides the increase in cosmic star-formation rate of both kinds of galaxies at high z.

The γ-rays from CCSNe are not added to the models of the individual galaxies (Milky Way, M82, and NGC 253's starburst), since supernovae are rare and transient events. However, we do include them in the γ-ray backgrounds. We assume in our calculations that each CCSN produces 0.07 M$_\odot$ of ^{56}Ni (e.g., Catchpole et al. 1988; Arnett & Fu 1989; Bouchet & Danziger 1993; Hamuy 2003). We include the strongest γ-ray lines from ^{56}Co at 0.847 MeV and 1.238 MeV, with time-averaged luminosities $L_{0.847} = 5.9 \times 10^{36} {\rm ergs\ s^{-1}} (\Gamma_{\rm SN}/\Gamma_{\rm SN,MW})$ and $L_{1.238} = 6.7 \times 10^{36} {\rm ergs\ s^{-1}} (\Gamma_{\rm SN}/\Gamma_{\rm SN,MW})$ (Ruiz-Lapuente et al. 2001). In addition, we include the continuum emission using the spectrum calculated in Ruiz-Lapuente et al. (2001), scaled to the 0.07 M$_\odot$ of ^{56}Ni per supernova.

3.2. *Milky Way*

Introduction – The Milky Way (MW) is the *only* non-active galaxy observed in MeV γ-rays, and only one of a handful of normal (non-starburst, non-active) galaxies observed in GeV γ-rays (with the LMC, SMC, and M31). At low energies, below ~ 50 keV, most of the Galactic X-ray ridge emission is resolved into stellar sources, such as cataclysmic variables (Revnivtsev et al. 2009). The energy region up to 511 keV includes a spectral spike from positron annihilation radiation. This annihilation radiation is concentrated towards the center of the Galaxy, which is not expected if it is correlated with star-formation (see the review by Prantzos et al. 2011). In the energy range from 100 keV to 100 MeV, there appears to be a power law continuum, with $\Gamma \approx 1.5$, thus increasing in luminosity to higher energies. This power law continuum has been interpreted in the past as bremsstrahlung (Schlickeiser 1982; Sacher & Schoenfelder 1983), though it is now believed to be Inverse Compton emission (Porter et al. 2008; Bouchet et al. 2011). However, there also appears to be an excess of γ-rays above the power law detected by COMPTEL in the $\sim 5 - 20$ MeV range towards the inner Galaxy (Strong et al. 2004b; Porter et al. 2008). The Galactic γ-ray luminosity peaks around a GeV, a pionic feature expected from theoretical expectations of CR propagation (e.g., Stecker 1970; Hunter et al. 1997; Strong et al. 2004b). Finally, the emission drops off rapidly as $E^{-2.7}$ to $E^{-2.6}$, continuing to TeV energies in at least some regions of the Galactic Plane (Prodanović et al. 2007; Abdo et al. 2008).

In modeling the Milky Way, we use a radius of 10 kpc. We consider scale heights (midplane to edge) of 1 kpc and 2 kpc. The gas surface density Σ_g is measured to be $\sim 0.0025\ {\rm g\ cm^{-2}}$ in the Solar neighborhood and through much of the Galactic disk (Boulares & Cox 1990; Yin et al. 2009). For the radiation field, we average the maximum metallicity gradient radiation fields of Porter et al. (2008) for $R = 4$ kpc and $R = 8$ kpc, reflecting the fact that much of the star-formation (and therefore CR generation) occurs at $R \approx 5 - 7$ kpc (Yin et al. 2009). In addition, we use a magnetic field strength of 6 μG (e.g., Strong et al. 2000a; Beck 2011), a diffusive escape time of $t_{\rm diff}(E) = 30\ {\rm Myr}\ (E/3\ {\rm GeV})^{-1/2}$ (Connell 1998; Webber et al. 2003), and a maximum primary electron Lorentz factor of $\gamma_{\rm max}^{\rm prim} = 2 \times 10^7$ as inferred from the apparent cutoff in the primary electron spectrum at TeV energies (e.g., Aharonian et al. 2008, 2009).

We assume that the total Galactic star-formation rate is 2 M$_\odot$ yr^{-1}, giving us a supernova rate of 1.6 century^{-1} for the SalA IMF. Estimates of the star-formation rate and supernova rate of the Galaxy span nearly an order of magnitude, though most of the larger ones are from older works (see Table 1 of Diehl et al. 2006a). Recent estimates of the star-formation rate from free-free emission or direct counting of young stellar objects find star-formation rates of $0.9 - 2.2$ M$_\odot$ yr^{-1} (Murray & Rahman 2010) and $0.7 - 1.5$ M$_\odot$ yr^{-1} (Robitaille & Whitney 2010), respectively; therefore, our star-formation rate estimate may be somewhat high. Chomiuk & Povich (2011) compile several star-formation rate estimators for the Galaxy and conclude that it

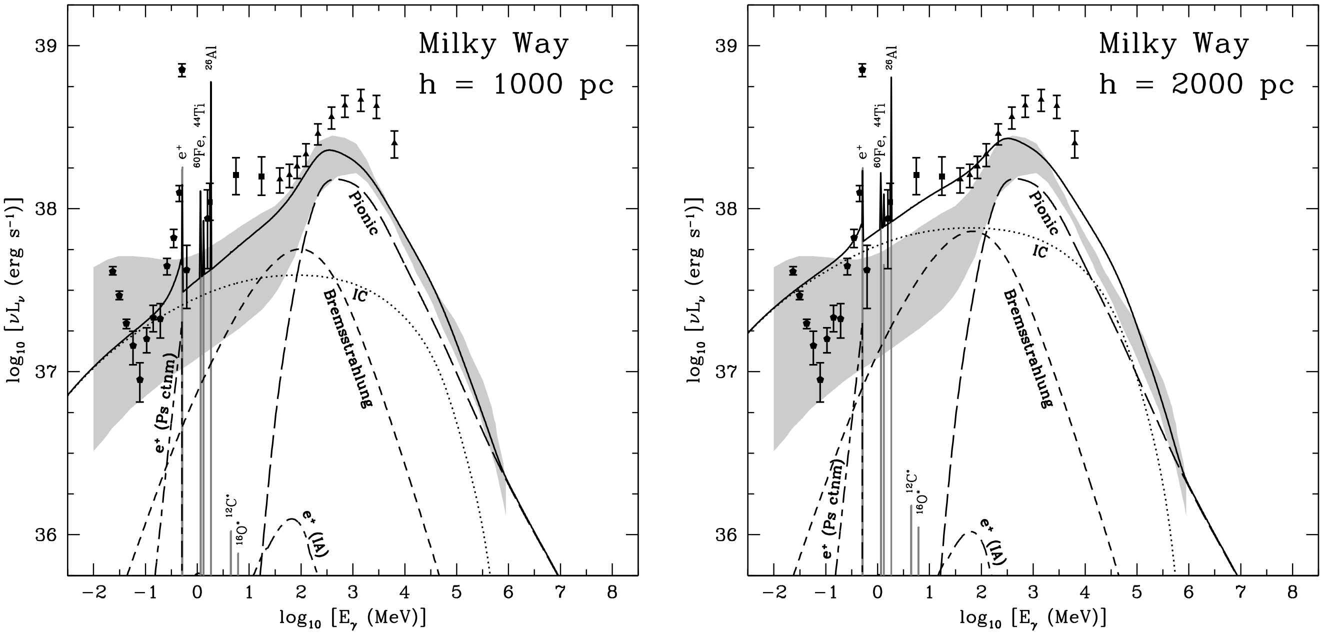

FIG. 2.— The predicted γ-ray luminosity spectrum of the Milky Way (solid), compared to extrapolated observations of the inner Galaxy with SPI (pentagons), COMPTEL (squares), and EGRET (triangles), as well as GalProp models (grey shading; Strong et al. 2010). The different components to the emission are positron annihilation (long-dashed/short-dashed), nucleosynthetic γ-ray lines (grey solid), CR nuclear de-excitation lines (grey solid), bremsstrahlung (short-dashed), IC (dotted), and pionic emission (long-dashed). The excess of GeV emission is an instrumental artifact of EGRET. Note that the predicted positron annihilation rate only includes the contribution from star-formation, but the observed positron emission includes the Galactic Center source. Emission from CCSNe is not included. Also note that the observations, predicted line spectra, and total predicted spectra have different energy binnings; the binning for the total spectrum is $\Delta E/E$ = 3%.

is $\sim 1.9\ M_\odot\ yr^{-1}$ for a Kroupa IMF. For a given star-formation rate, and for stellar masses greater than 1 $M_\odot$ where most of the starlight used to infer the star-formation rate history of the Universe comes from, the IMFs differ by less than 30%. At 10 $M_\odot$, the approximate mass of most supernova progenitors, the IMFs differ by only 13%. The result of 2 $M_\odot\ yr^{-1}$ should thus be applicable for the SalA IMF that we use, to within a factor of < 2. On the other hand, we use the star-formation rate solely to calculate the supernova rate, which is about a factor ~ 1.2 lower than in Diehl et al. (2006a) (estimated from the ^{26}Al γ-ray line).

We set the 1 MeV positron injection rate from radioactive elements for the entire Galaxy to be $8.1 \times 10^{42} s^{-1}$, as determined for the Galactic disk by Weidenspointner et al. (2008a) with their "bulge + thick disk" model. This does not include the positron rate from the bulge, which is substantially higher ($\sim 2 \times 10^{43} s^{-1}$). In using this value for the nucleosynthetic positrons, we assume that CR positrons contribute a minority of this rate, which is verified by our modeling and GALPROP models (Porter et al. 2008).

Comparison with observed γ-rays – We scale our predicted γ-ray spectra by comparing our models' 100 MeV - 100 GeV pionic γ-ray luminosities to the more detailed predictions in Strong et al. (2010). We find using standard acceleration efficiencies (η = 0.1) and our fiducial supernova rate that our models' γ-ray luminosity is too small. We find we must scale up η (and ξ using $\tilde{\delta}$ = 75) the h = 1000 pc γ-ray luminosity by a factor 1.7 and the h = 2000 pc luminosity by a factor 3.3. There could be several reasons for this discrepancy: our supernova rate could be too small by a factor $\sim 2-3$ (but this would contradict current observations), the CR acceleration efficiency could be greater by a factor $\sim 2-3$, or the strength of pionic losses to escape losses for CR nuclei is $\sim 2-3$ times stronger than we calculate (meaning either slower escape or higher gas densities).

To check these reasons for the low γ-ray luminosity, we examine the density and CR luminosity of our models. The average density that CRs experience in our models is 0.24 cm^{-3} in the h = 1000 pc model and 0.12 cm^{-3} in the h = 2000 pc model; CRs observed at Earth are inferred to traverse mean densities of 0.25 cm^{-3} in the Milky Way (Connell 1998; Schlickeiser 2002). The h = 2000 pc model therefore is too γ-ray dim partly because it is too low density; this is not the case for the h = 1000 pc case. The CR luminosity in our models is 5.1×10^{40} ergs s^{-1}; Strong et al. (2010) find CR luminosities of $\sim 7 \times 10^{40}$ ergs s^{-1} for their h = 2 kpc models. Since we are comparing to their γ-ray luminosity, our CR luminosity is $\sim$ 40% too low; after accounting for this, the γ-ray luminosity of the h = 1000 pc model is within 25% of that of the Strong et al. (2010) model. We conclude that the need for the scale factor arises because the CR luminosity is too low in our models, and also because the mean density is too low in the h = 2000 pc model.

The rescaled γ-ray spectra are plotted in Figure 2. Pionic emission dominates the γ-ray emission at most energies above 100 MeV, leading to the observed pionic bump. At MeV energies, the relative strengths of the leptonic emission processes depend on the assumed scale height. In the smaller scale height (1000 pc; left panel in Figure 2) models, CR $e^\pm$ experience higher gas densities than the large scale height models (2000 pc; right panel in Figure 2), but the radiation field is the same. Therefore, bremsstrahlung receives more power in the h = 1000 pc model than the h = 2000 pc model. We find that in the h = 1000 pc models, bremsstrahlung is the most important emission from $\sim 10-100$ MeV and IC is the most important continuum emission at energies below that. In the

h = 2000 pc models, IC is the dominant continuum emission process at energies below 100 MeV, although bremsstrahlung nearly equals it at 100 MeV. This is in accordance with expectations that the truly diffuse Galactic nonthermal continuum in the 100 keV – MeV range is IC emission (Porter et al. 2008; Bouchet et al. 2011). The h = 1000 pc model spectrum is essentially in agreement with GALPROP luminosity spectra within uncertainties, although the h = 2000 pc model has much more leptonic emission (Figure 2; Strong et al. 2010).

In Figure 2, we also plot observations of the inner Milky Way γ-ray spectrum. The shown data are scaled from INTEGRAL SPI (Bouchet et al. 2008), COMPTEL, and EGRET (Porter et al. 2008) data plotted in Türler et al. (2010). These are translated into Galactic luminosities by assuming that CR γ-ray emission is distributed spatially the same as ^{26}Al nuclear line emission (which is associated with massive stars), and using the ratio of the ^{26}Al line flux observed from the same sky region and the Galactic luminosity reported by Diehl et al. (2006a). Comparing the spectral shape of the models with the observed spectrum, we find that the h = 1000 pc model is the better match below 1 MeV (see Figure 2). The IC continuum in the h = 2000 pc model is up to a factor ~ 3 times too high at these energies. Conversely, the h = 2000 pc model is the better match above 1 MeV, with the h = 1000 pc model underproducing flux in the few MeV range by up to a factor ~ 3. Note the GALPROP models from Strong et al. 2010 also fail to reproduce the MeV emission, even considering the uncertainties in halo size. The plotted data above the GeV are from EGRET, and the apparent "GeV excess" is now known to be an instrumental effect (Stecker et al. 2008; Abdo et al. 2009).

We use the h = 2000 pc model as our fiducial model of the Milky Way.

Results for MeV γ-rays – Most of the star-formation associated positron annihilation rate comes from nucleosynthetic positrons. Of the 8.1×10^{42} s^{-1} nucleosynthetic positrons injected in the Galactic disk at 1 MeV, we find that 6.8×10^{42} s^{-1} (83%) survive to low energies. In addition, we find that $7.6 - 7.8 \times 10^{41}$ s^{-1} positrons are injected through pion production, about 40 – 80% of the rate calculated by GALPROP models (Porter et al. 2008). Of these, 5.5×10^{41} s^{-1} (72%) annihilate near rest in the h = 1000 pc model and 4.8×10^{41} s^{-1} (61%) annihilate near rest in the h = 2000 pc model. The remaining positrons either escape or annihilate in flight. Our models indicate that ~ 7% of the disk positrons are hadronic in origin. The luminosity in positronium continuum and the 511 keV line is $\sim 6 \times 10^{36}$ ergs s^{-1}, whereas the νL_ν luminosity of the nonthermal Galaxy at that energy is 4×10^{37} ergs s^{-1} in the h = 1000 pc model and 7×10^{37}ergs s^{-1} in the h = 2000 pc. Therefore positron annihilation near rest associated with star-formation is only ~ 10% of the luminosity of the Galaxy near 511 keV.

The total positron in-flight annihilation luminosity is one half of the luminosity of positrons annihilating at rest, $\sim 3 - 4 \times 10^{36}$ ergs s^{-1}. While by number, most positrons survive to low energy, pionic positrons have much more energy when they are injected than when they are near rest. Therefore, most of the power from pionic positron annihilation comes out near ~ 65 MeV. On the other hand, the other nonthermal Galactic emission is also greater at these energies, with $\nu L_\nu \approx 1.2 - 1.8 \times 10^{38}$ ergs s^{-1} so that in-flight annihilation is just a few percent of the Galactic luminosity at these energies.

The nucleosynthetic γ-ray lines are a significant but minority contributor to the MeV γ-ray luminosity of the Galaxy. The strongest line, 1.809 MeV emission from ^{26}Al, has a luminosity of 1.7×10^{37} ergs s^{-1}. The other nucleosynthetic lines considered (^{60}Fe 1.173 and 1.333 MeV, ^{44}Ti 1.157 MeV) have luminosities of $1.5 - 2.5 \times 10^{36}$ ergs s^{-1}, for a total nucleosynthetic line luminosity of 2.6×10^{37} ergs s^{-1}. The nonthermal luminosity at 1.5 MeV is $\nu L_\nu \approx 4 \times 10^{37}$ ergs s^{-1} for h = 1 kpc and 8×10^{37} ergs s^{-1} for h = 2 kpc. Nucleosynthetic lines therefore make up about ~ 30% of the luminosity at energies around 1 MeV.

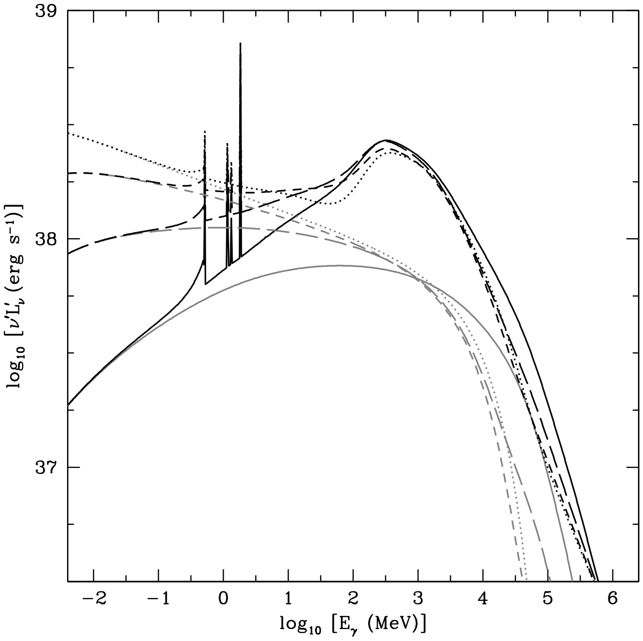

FIG. 3.— Rest-frame evolution of the total (black) and IC (grey) γ-ray spectrum of the Milky Way (with its current physical conditions) placed at different redshifts (0: solid; 1: long-dashed; 2: short-dashed; 4: dotted). At z = 0, the emission falls rapidly as E_γ decreases. But at higher redshift, the stronger CMB enhances Inverse Compton emission in the MeV band until it is at least $\sim 1/2$ of the GeV luminosity, partly flattening the pion bump. To show the differences in spectral shape, we assume the Milky Way's SFR is the same at all z, although it was likely bigger in the past.

More exotic processes, such as synchrotron and nuclear deexcitation lines, are insignificant in our models of the Milky Way.

High z – In Figure 3, we see the effects of the increasing CMB strength at high z: the Inverse Compton component becomes much stronger. This enhances the MeV emission considerably in Milky Way-like galaxies: in fact, at z = 2, the 1 MeV νL_ν luminosity is 76% of the 1 GeV νL_ν luminosity. Thus the enhancement of IC at high z must be accounted for in calculating the MeV background from MW like galaxies.

An interesting effect that occurs in Milky Way-like galaxies at high z is that the fraction of hadronic positrons surviving to rest increases from 60-70% to ~ 87%, enhancing the hadronic positron annihilation rate by ~ 20%. This is because the increased Inverse Compton losses off the CMB grow stronger than escape, so that CR positrons are trapped more effectively in the host galaxy. However, given that hadronic positrons form only a small fraction of the star-formation associated positrons, the total Galactic disk positron annihilation rate is only enhanced by 2%.

3.3. *M82*

Introduction – M82 is a nearby starburst galaxy ($D \approx$ 3.6 Mpc; Freedman et al. 1994), the brightest in the GeV and

TeV γ-ray sky (Abdo et al. 2010f; Acciari et al. 2009), and one of the brightest galaxies observed in the IR (Sanders et al. 2003). The starburst lies in the central regions of the galaxy ($R \leq 250$ pc), where a large amount of gas, infrared emission, and radio emission is observed (Goetz et al. 1990; Williams & Bower 2010). About 2×10^8 $M_\odot$ of gas is observed in the central regions, giving a gas surface density of 0.17 g cm^{-2} (Weiß et al. 2001). M82 is also observed to host a starburst wind, and we consider wind speeds from 0 to 1000 km s^{-1}.

Using the observed TIR luminosity of 5.9×10^{10} $L_\odot$ from (Sanders et al. 2003), we take the supernova rate as 0.067 yr^{-1}, compared to typically quoted values in the literature of ~ 0.1 yr^{-1} with factor $\sim 2-3$ uncertainty (see the summary in Lacki et al. 2011). This corresponds to a star-formation rate of 8.0 $M_\odot$ yr^{-1}.

Essentially nothing is known observationally about M82's MeV emission. It has been detected in 10 - 50 keV X-ray emission by Suzaku and Swift-BAT (Cusumano et al. 2010). Very weak upper limits on the continuum MeV emission exist from non-detections by OSSE (Bhattacharya et al. 1994). Searches for nuclear lines from M82 and NGC 253 with OSSE have also found nothing yet (Bhattacharya et al. 1994). In the two year *Fermi*-LAT catalog, M82 is detected with $\gtrsim 5\sigma$ significance at energies down to 100 MeV, although the *Fermi*-LAT data does not yet go down below that. There are, however, several theoretical models for M82's multiwavelength nonthermal emission, including MeV energies (e.g., Persic et al. 2008; de Cea del Pozo et al. 2009a).

Constraints from radio and GeV-TeV γ-rays – We use the interferometric radio data compiled in Williams & Bower (2010), combined with the original γ-ray data from Abdo et al. (2010f) and Acciari et al. (2009). The combined radio (Fig. 4) and γ-ray (Fig. 5) data constrain the allowed parameter space in M82 significantly, although there are still large degeneracies. We also plot X-ray data on Figure 5, although we do not include it in the fitting. This emission largely comes from discrete X-ray binaries, and even the diffuse emission likely comes from hot thermal gas which would not contribute at MeV energies (e.g., Strickland & Heckman 2007).

The best-fitting $B = 50$ μG model (which has $h = 100$ pc) is a relatively poor fit to the data compared to models with higher B (the total χ^2 for $B = 50$ μG models is ≥ 120, whereas $\chi^2 \gtrsim 70$ for models with higher B). This is because the observed radio emission combined with the assumption of a small magnetic field imply a large number of CR $e^{\pm}$, in turn implying vast amounts of leptonic γ-ray emission which exceed the observed amounts. Although there may be other parameters affecting the emission, the likely explanation is that B is greater than 50 μG in M82.

The best-fit models for other B (100 – 400 μG) all fit M82 with comparable accuracy ($\chi^2 = 70-73$) to each other. The best-fit models all have relatively small scale heights of 30 pc, or in the case of $B = 400$ μG, 10 pc (see Table 1). This is because of the shallowness of the radio spectrum combined with the spectral curvature, which is inconsistent with large amounts of free-free emission (Williams & Bower 2010; Fig. 4). Smaller h for a given Σ_g implies higher gas densities and therefore stronger bremsstrahlung and ionization losses; the smaller h also means the wind-crossing times are shorter for M82 (compare the expectations in Lacki & Thompson 2010b). In all of the $B > 50$ μG models, $S_{\rm ff}(1\ {\rm GHz}) = 0.34-0.45$ Jy for a thermal fraction of ~ 0.04 (compared to ~ 0.06 in Williams & Bower 2010).

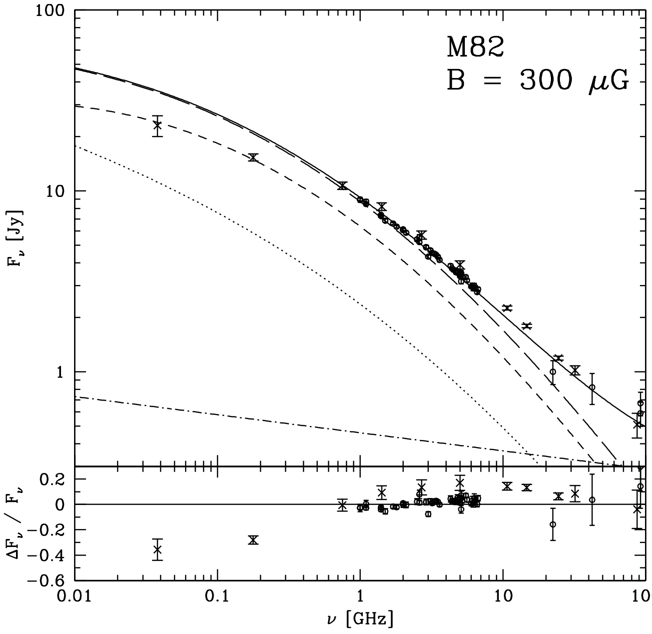

FIG. 4.— Predicted radio spectrum of M82 in the best-fit $B = 300$ μG model with no primary positrons. Plotted lines are total radio emission (solid), total synchrotron emission (long-dashed), synchrotron from secondaries (short-dashed), synchrotron from primaries (dotted), and free-free emission (dash-dotted). Plotted data are the interferometric data compiled in Williams & Bower (2010) (open circles), and data from Klein et al. (1988) (X's). The bottom panel shows the residuals to the radio data. The discrepancy at low frequencies (data at < 1 GHz is not included in our fitting) is probably due to free-free absorption. At high frequencies, thermal free-free emission flattens the spectrum.

The relatively poor γ-ray data do not allow us to discriminate the relative mixture of leptonic and hadronic emission at GeV energies. The GeV emission in $B = 100-150$ μG models is actually dominated by leptonic emission, both bremsstrahlung and Inverse Compton. These models have very high ξ (0.03 – 0.05) and small η (0.009 - 0.03), resulting in high $\tilde{\delta} \approx 1$. However, in order for the flat Inverse Compton continuum to not overproduce the TeV emission, the primary electron spectrum must cut off at $\gamma_{\rm max}^{\rm prim} = 10^6$ to 10^7. The TeV emission is pionic radiation; $v_{\rm wind}$ is 0 and diffusive escape is slow in these models so that the few protons are efficiently converted into γ-rays.

By contrast, in high B models (200 – 400 μG), the GeV-TeV emission is largely pionic. We find $\eta \approx 0.07-0.14$, in line with previous use of $\eta \approx 0.1$. The electron acceleration efficiency is relatively small, shrinking from 0.02 at 200 μG to 0.006 at 300 μG. The best-fit wind speeds are 150 - 300 km s^{-1}, giving comparable advective and pionic lifetimes for protons in M82, as expected from the γ-ray brightness (Lacki et al. 2011). Diffusion is also relatively quick in the $B = 200-300$ μG models, probably to compensate for the best-fit $p = 2.1$ injection slope and steepen the GeV-TeV spectra. The $B = 400$ μG model, in contrast, has $p = 2.3$ and no diffusion.

The $B = 300$ μG model has the highest $\tilde{\delta}$ of the best-fit models for each B, equal to 49. This is the closest to the Milky Way value of 50 - 100, so we adopt it as our fiducial model when needed.

The GeV-TeV results are not significantly affected if we assume that half of the primary $e^{\pm}$ are positrons, instead of all

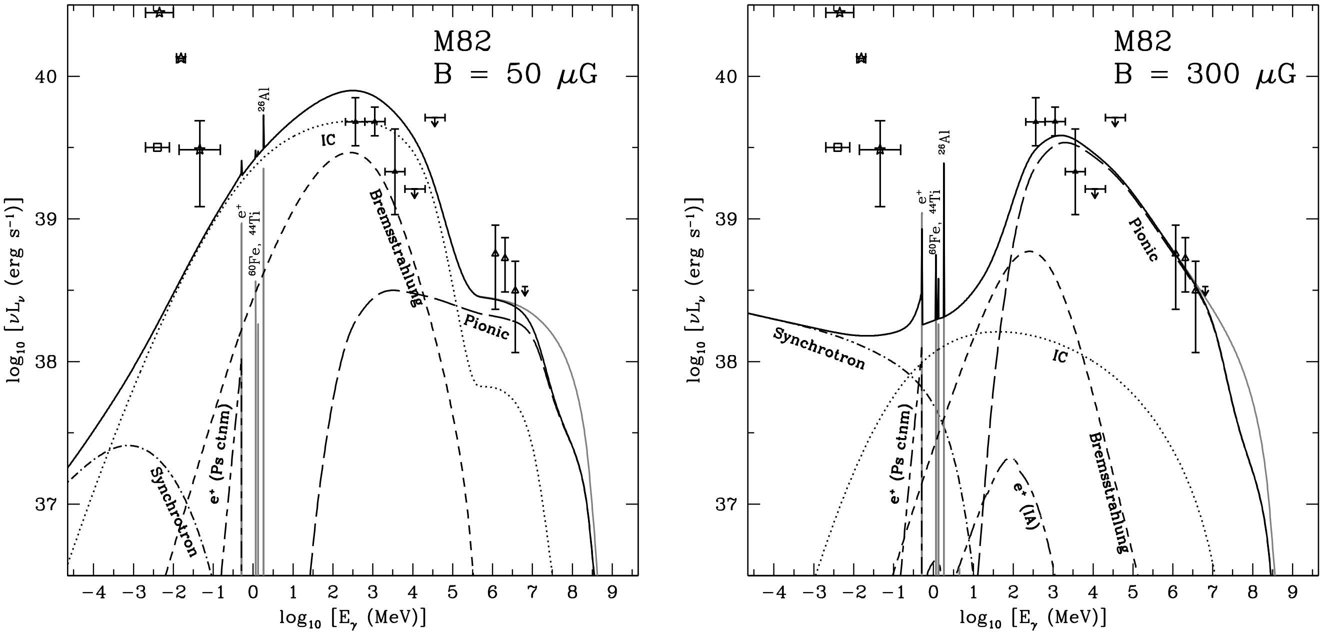

FIG. 5.— The predicted γ-ray luminosity spectrum of M82, compared to X-ray (total, stars: Cappi et al. 1999; Miyawaki et al. 2009; Cusumano et al. 2010; diffuse, square: Strickland & Heckman 2007) and γ-ray (Abdo et al. 2010f; Acciari et al. 2009) observations. The different components to the emission are synchrotron (dash/dotted), positron annihilation (long-dashed/short-dashed), nucleosynthetic γ-ray lines (grey lines), bremsstrahlung (short-dashed), IC (dotted), and pionic emission (long-dashed). The total emission are the solid lines, black including $\gamma\gamma$ absorption on the sightline to Earth and grey without it. The plotted models show the case for when primary $e^{\pm}$ are purely electrons, with no primary positrons. Emission from CCSNe is not included. The X-ray emission mostly comes from X-ray binaries and thermal emission from gas and is not included in our fitting. As in Figure 2, note the different energy binnings for the lines.

of them being electrons.

Results for MeV γ-rays – The main source of MeV γ-ray emission is that from Inverse Compton and bremsstrahlung. In the fiducial model, the MeV emission is $\sim$ 10% of the GeV luminosity (Figure 5, right panel). Because of the small scale heights preferred, meaning high density relative to radiation field, bremsstrahlung is enhanced at expense of Inverse Compton. This concentrates luminosity in the bremsstrahlung bump at 100 MeV and reduces the power available at the lower end of the MeV range. We find that while the 0.1 - 10 GeV luminosity of M82 is 1.4×10^{40} ergs s^{-1} in our fiducial model, the 1 - 100 MeV luminosity is only 2.1×10^{39} ergs s^{-1}. Surprisingly, we find that synchrotron is the dominant source of nonthermal diffuse emission up to 100 keV in our fiducial model. This is because the primary electron spectrum extends to $\gamma = 10^9$ in that model. Considering how little is known about PeV CR $e^{\pm}$, the actual strength of the synchrotron component is highly uncertain.

The low B models have stronger leptonic emission, in some models erasing the pion bump entirely. The larger scale height reduces the importance of bremsstrahlung with respect to IC. Even in these models, the bremsstrahlung bump still causes the peak of the emission to be at 300 MeV (Figure 5). However, the relative dominance of IC emission means that νL_{ν} is only $\sim$ 3 times smaller at 1 MeV than at 300 MeV in the $B = 50$ μG model. In the best-fit $B = 50$ μG model with no primary e^{+}, the 0.1 - 10 GeV luminosity is 3.0×10^{40} ergs s^{-1} while the 1 - 100 MeV luminosity is 2.3×10^{40} ergs s^{-1}.

The positron annihilation radiation is a possible contributor to the γ-ray flux in the 100 - 500 keV range (Figure 6). In models where the primary $e^{\pm}$ are entirely electrons, the nucleosynthetic positrons are the dominant source of positrons. However, even in these models, the relatively calorimetric environment means that there is a large rate of hadronic positrons cooling all the way down to thermal energies: roughly $1/3$ of the positron annihilation radiation in our fiducial model is from pionic e^{+}. Thus starbursts have enhanced positron annihilation radiation associated with star-formation compared to normal galaxies (although non-star-formation processes are relatively weaker). In the fiducial model, the total positron annihilation energy luminosity is 3.7×10^{37} ergs s^{-1} from positronium continuum and 511 keV line emission, plus 7.3×10^{37} ergs s^{-1} from in-flight annihilation radiation. Hence the positron annihilation emission is only $\sim$ 5% of the total MeV band emission; only near 511 keV does it actually dominate.

In models where half of the primary $e^{\pm}$ are positrons, there is a vast positron annihilation rate, especially in low B models which have high ξ. These models have combined positronium and 511 keV line emission luminosities of 3×10^{38} ergs s^{-1} and 5.6×10^{39} ergs s^{-1} for $B = 300$ μG and 50 μG, respectively, with an additional 2.0×10^{38} ergs s^{-1} and 2.5×10^{39} ergs s^{-1} from in-flight radiation. The extraordinarily intense 511 keV line emission in these models may be constrained with future MeV instruments (see Table 2).

Finally, the ^{26}Al and other nuclear lines are a significant contributor to the $\sim$ 1 MeV luminosity of M82. The 1.809 MeV line is the strongest γ-ray line except possibly the 511 keV annihilation line. However, the photon flux is actually small, only $\sim 2 \times 10^{-8}$cm^{-2} s^{-1}. As for the nuclear de-excitation lines, they are completely negligible in M82 and far beyond any proposed detection capability (Table 2).

High z – The CMB has much less of an effect on a starburst like M82 than in the Milky Way because the CMB is subdominant with respect to the high magnetic fields and starlight energy density (synchrotron and IC are the dominant loss processes at high electron energy). We find that even at $z = 4.9$, the MeV emission is enhanced only by at most 24% in our

TABLE 1
BEST-FIT MODELS OF M82 AND NGC 253

B	Prim	Best-fit parameters								
	$e^{\pm}$ [a]	h	p	t_{diff}(3 GeV)	$\gamma_{\mathrm{max}}^{\mathrm{prim}}$	v_{wind}	η	ξ [b]	S_{ff}(1 GHz) [c]	$\tilde{\delta}$
μG		pc		Myr		km s^{-1}			Jy	
					M82					
50	e^{-}	100	2.1	∞	10^6	1000	0.025	0.11	0.91	0.44
	$e^{\pm}$	100	2.1	∞	10^6	1000	0.025	0.11	0.91	0.44
100	e^{-}	30	2.1	∞	10^6	0	0.0088	0.051	0.41	0.34
	$e^{\pm}$	30	2.1	∞	10^6	0	0.0088	0.051	0.41	0.34
150	e^{-}	30	2.1	10	10^7	0	0.025	0.026	0.37	1.9
	$e^{\pm}$	30	2.1	10	10^6	0	0.025	0.025	0.37	2.0
200	e^{-}	30	2.1	1	10^9	150	0.10	0.017	0.42	12
	$e^{\pm}$	30	2.1	1	10^8	150	0.10	0.016	0.41	12
250	e^{-}	30	2.1	1	10^9	300	0.14	0.011	0.34	25
	$e^{\pm}$	30	2.1	1	10^6	300	0.14	0.0093	0.34	30
300	e^{-}	30	2.1	1	10^9	300	0.14	0.0058	0.46	49
	$e^{\pm}$	30	2.1	1	10^6	300	0.14	0.0048	0.45	58
400	e^{-}	10	2.3	∞	10^6	150	0.071	0.023	0.34	24
	$e^{\pm}$	10	2.3	100	10^9	150	0.071	0.024	0.34	23
					NGC 253 Core					
50	e^{-}	50	2.1	10	10^6	1000	0.20	0.19	0.34	2.1
	$e^{\pm}$	50	2.1	10	10^6	1000	0.20	0.19	0.34	2.1
100	e^{-}	15	2.1	100	10^6	150	0.050	0.084	0.20	1.2
	$e^{\pm}$	15	2.1	∞	10^6	150	0.050	0.085	0.19	1.2
150	e^{-}	15	2.1	10	10^6	150	0.071	0.043	0.18	3.3
	$e^{\pm}$	15	2.1	10	10^6	150	0.071	0.043	0.18	3.3
200	e^{-}	5	2.1	0.1	10^8	0	0.10	0.077	0.082	2.6
	$e^{\pm}$	5	2.1	0.1	10^9	0	0.10	0.081	0.076	2.4
250	e^{-}	5	2.1	0.1	10^9	0	0.14	0.050	0.13	5.6
	$e^{\pm}$	5	2.1	0.1	10^9	0	0.14	0.051	0.13	5.5
300	e^{-}	5	2.1	1	10^6	0	0.071	0.026	0.069	5.3
	$e^{\pm}$	5	2.1	1	10^6	0	0.071	0.027	0.062	5.3
400	e^{-}	5	2.1	1	10^6	0	0.10	0.0071	0.16	28
	$e^{\pm}$	5	2.1	1	10^6	0	0.10	0.0072	0.15	28

[a] Denotes whether the primary electrons and positrons in the model are all electrons (e^{-}) or half electrons and half positrons ($e^{\pm}$).
[b] Includes both primary electrons and primary positrons.
[c] Flux of free-free emission at 1 GHz observed at Earth.

fiducial model. In the $B = 50$ μG model, the MeV enhancement at $z = 4.9$ is 65% at 100 keV and less at high energies.

3.4. *NGC 253 Core*

Introduction – NGC 253 ($D \approx 3.5$ Mpc; Rekola et al. 2005) is the only other starburst galaxy detected in both GeV and TeV γ-rays, and is second only to M82 in infrared brightness for starbursts (Sanders et al. 2003). The radio continuum, molecular line, and infrared emission is concentrated in a region with a radius between 125 and 255 pc in radius (e.g., Turner & Ho 1983; Peng et al. 1996; Ulvestad & Antonucci 1997; Ulvestad 2000; Sakamoto et al. 2011); we therefore take the radius of the starburst core to be 150 pc. Since the vertical extent of the radio disk implies a maximum midplane-to-edge scale height of 70 pc (Ulvestad & Antonucci 1997), we consider scale heights of 50, 15, and 5 pc. A variety of measurements give gas masses of $(2-5) \times 10^7$ $M_{\odot}$ (e.g., Mauersberger et al. 1996; Harrison et al. 1999; Bradford et al. 2003; Sakamoto et al. 2011). Using a radius of 150 pc gives us a surface density of $0.07-0.15$ g cm^{-2}; we adopt 0.1 g cm^{-2} here.

While the total infrared luminosity of NGC 253 as a whole is 3.5×10^{10} $L_{\odot}$, only half of that comes from the starburst itself (Melo et al. 2002), so we adopt a luminosity of 1.7×10^{10} $L_{\odot}$. Using the Kennicutt (1998) conversion factor and translating this to a SalA IMF, we get a star-formation rate of 2.3 $M_{\odot}$ yr^{-1} and a supernova rate of 0.020 yr^{-1} (compared to the canonical $0.03-0.1$ yr^{-1}; again, see the summary in Lacki et al. 2011).

Like M82, almost nothing is known about NGC 253's MeV emission from observations. It is not even detected in 10 - 50 keV X-rays by Swift-BAT (Cusumano et al. 2010). Interestingly, OSSE *did* report a detection for NGC 253 in the 100 keV range, which Goldshmidt & Rephaeli (1995) interpreted as IC emission from the halo of NGC 253. However, this detection implies a ~ MeV luminosity many times greater than the GeV luminosity detected by *Fermi*. Furthermore, NGC 253 was not detected in this energy band with the more sensitive Swift-BAT, so we consider it spurious (Cusumano et al. 2010), although it could have been from a transient source. It is interesting, though, that if the detection were typical of starburst galaxies, then starbursts would make up the MeV background. OSSE have provided very weak constraints on the continuum and line emission from NGC 253 (Bhattacharya et al. 1994). In the two-year *Fermi*-LAT catalog, NGC 253 is detected down to 300 MeV (Nolan et al. 2012). A number of theoretical models of the nonthermal emission predict the MeV spectrum (e.g., Paglione et al.

TABLE 2
GAMMA-RAY LINE STRENGTHS

Line[a]	E_γ	Source[b]	M82				NGC 253 Core			
			Low B[c]		High B[d]		Low B[e]		High B[f]	
	MeV		Luminosity ergs s^{-1}	Photon Flux ph cm^{-2} s^{-1}	Luminosity ergs s^{-1}	Photon Flux ph cm^{-2} s^{-1}	Luminosity ergs s^{-1}	Photon Flux ph cm^{-2} s^{-1}	Luminosity ergs s^{-1}	Photon Flux ph cm^{-2} s^{-1}
e^+ annih.	0.511	CR (hadr.)	2×10^{35}	1×10^{-10}	3×10^{36}	3×10^{-9}	2×10^{35}	1×10^{-10}	3×10^{36}	2×10^{-9}
		CR (prim. e^+)	3×10^{39}	3×10^{-6}	1×10^{38}	1×10^{-7}	2×10^{39}	1×10^{-6}	6×10^{37}	5×10^{-8}
		Nucleo.	2×10^{37}	1×10^{-8}	2×10^{37}	1×10^{-8}	5×10^{36}	4×10^{-9}	5×10^{36}	4×10^{-9}
^{26}Al decay[g]	1.809	Nucleo.	7×10^{37}	2×10^{-8}	7×10^{37}	2×10^{-8}	2×10^{37}	5×10^{-9}	2×10^{37}	5×10^{-9}
^{60}Fe decay[g]	1.173	Nucleo.	5×10^{36}	2×10^{-9}	5×10^{36}	2×10^{-9}	2×10^{36}	6×10^{-10}	2×10^{36}	6×10^{-10}
	1.333	Nucleo.	5×10^{36}	2×10^{-9}	5×10^{36}	2×10^{-9}	2×10^{36}	6×10^{-10}	2×10^{36}	6×10^{-10}
^{44}Ti decay[g]	1.157	Nucleo.	1×10^{37}	4×10^{-9}	1×10^{37}	4×10^{-9}	3×10^{36}	1×10^{-9}	3×10^{36}	1×10^{-9}
^{4}He de-ex.	0.429	CR (broad)	7×10^{31}	7×10^{-14}	4×10^{32}	4×10^{-13}	2×10^{32}	2×10^{-13}	1×10^{32}	1×10^{-13}
^{4}He de-ex.	0.478	CR (broad)	9×10^{31}	8×10^{-14}	6×10^{32}	5×10^{-13}	2×10^{32}	2×10^{-13}	1×10^{32}	1×10^{-13}
^{12}C de-ex.	4.438	CR (narrow)	7×10^{33}	6×10^{-13}	6×10^{34}	5×10^{-12}	1×10^{34}	1×10^{-12}	2×10^{34}	2×10^{-12}
		CR (broad)	2×10^{34}	1×10^{-12}	1×10^{35}	9×10^{-12}	3×10^{34}	3×10^{-12}	2×10^{34}	2×10^{-12}
^{16}O de-ex.	6.129	CR (narrow)	4×10^{33}	2×10^{-13}	3×10^{34}	2×10^{-12}	7×10^{33}	5×10^{-13}	1×10^{34}	8×10^{-13}
		CR (broad)	6×10^{33}	4×10^{-13}	4×10^{34}	3×10^{-12}	1×10^{34}	1×10^{-12}	9×10^{33}	6×10^{-13}
^{16}O de-ex.	6.916	CR (narrow)	1×10^{33}	6×10^{-14}	7×10^{33}	4×10^{-13}	2×10^{33}	1×10^{-13}	2×10^{33}	1×10^{-13}
		CR (broad)	2×10^{33}	1×10^{-13}	1×10^{34}	6×10^{-13}	4×10^{33}	2×10^{-13}	2×10^{33}	1×10^{-13}
^{16}O de-ex.	7.115	CR (narrow)	1×10^{33}	6×10^{-14}	8×10^{33}	4×10^{-13}	2×10^{33}	1×10^{-13}	2×10^{33}	1×10^{-13}
		CR (broad)	2×10^{33}	1×10^{-13}	1×10^{34}	6×10^{-13}	4×10^{33}	2×10^{-13}	2×10^{33}	1×10^{-13}
^{12}C de-ex.	15.10	CR (narrow)	1×10^{32}	4×10^{-15}	1×10^{33}	3×10^{-14}	3×10^{32}	8×10^{-15}	4×10^{32}	1×10^{-14}
		CR (broad)	5×10^{32}	1×10^{-14}	3×10^{33}	8×10^{-14}	1×10^{33}	3×10^{-14}	7×10^{32}	2×10^{-14}

[a] "Annih." abbreviates annihilation and "de-ex." abbreviates de-excitation.
[b] "Nucleo." stands for γ-ray lines produced by short-lived radioisotopes produced directly by stellar isotopes, while "CR" stands for γ-ray lines powered by CRs interacting with the ISM. For de-excitation lines, "narrow" stands for the line component produced by the ISM atoms after being hit by a CR, while "broad" stands for the Doppler-shifted line component emitted by the CRs after hitting an ISM atom. For the positron annihilation line, "hadr." stands for hadronic positrons and "prim e^+ stands for primary positrons.
[c] Values for the $B = 50\ \mu$G model of M82 with no primary positrons, except for the "CR (prim. e^+)" row, which refers to the model with primary electrons and positrons.
[d] Values for the $B = 300\ \mu$G model of M82 with no primary positrons, except for the "CR (prim. e^+)" row, which refers to the model with primary electrons and positrons.
[e] Values for the $B = 50\ \mu$G model of NGC 253 core with no primary positrons, except for the "CR (prim. e^+)" row, which refers to the model with primary electrons and positrons.
[f] Values for the $B = 400\ \mu$G model of NGC 253 core with no primary positrons, except for the "CR (prim. e^+)" row, which refers to the model with primary electrons and positrons.
[g] The nucleosynthetic γ-ray lines have exactly the same luminosities and fluxes in the high B and low B models.

1996; Domingo-Santamaría & Torres 2005; Rephaeli et al. 2009).

Constraints from radio and GeV-TeV γ-rays – We find generally similar results for NGC 253's starburst core[8] as we do for M82, which is not surprising given the similar physical conditions in these starbursts (see Table 1).

The radio spectrum for the core of NGC 253 is even flatter than that of M82 (see Fig. 7). In addition to forcing p to 2.1, it forces the best-fit scale heights to be even smaller than for M82: 15 pc for $B = 100-150$ pc and 5 pc for higher B. This is because of the flattening effect of bremsstrahlung and ionization losses on the electron spectrum (c.f., Thompson et al. 2006a). Of course, scale heights of only 5 pc for NGC 253's starburst are not physically realistic. Another possibility, here unexplored, is that CRs are preferentially interacting with gas of higher density than the mean: for example, if they only interact with the dense cores of molecular clouds. If true, this would be the opposite of the apparent situation of the Galactic Center, where the low γ-ray luminosity suggests that CRs avoid the dense cores of molecular clouds (Crocker et al. 2011b).

As with M82, the GeV emission in low B models is mainly leptonic and in high B models it is mainly hadronic. The TeV emission is pionic, requiring the primary $e^{\pm}$ spectrum to cut off at $\gamma_{\rm max}^{\rm prim}$ in low B models. At $B = 50\ \mu$G, the fit is poorer than in the other models, suggesting that $B > 50\ \mu$G in NGC 253's core as well ($\chi^2 = 110$ for 50 μG instead of $70-80$ for higher B), although the difference in fit quality is not as great as in M82. We find that η approaches ~ 0.1 for $B \gtrsim 200\ \mu$G, as expected. However, we find small wind speeds of 150 km s^{-1} in $100-150\ \mu$G models and *no* winds in models with higher B. This may be because h is so small in the high B models, so that even a slow wind rapidly advects CR nuclei out of the starburst; if instead both h and $\langle n \rangle$ are larger in reality, more rapid winds would be allowed. On the other hand, rapid diffusion ($0.1-1$ Myr at 3 GeV) is required in the best-fit models with $B \geq 200\ \mu$G, probably to steepen the pionic γ-ray spectrum from $\Gamma \approx 2.1$ to the observed 2.3.

None of the best-fit models have Milky Way-like values of $\tilde{\delta}$. In fact, all of them with $B \leq 300\ \mu$G have $\tilde{\delta} \approx 1-6$, which would indicate significant power in leptons. The $B = 400\ \mu$G model has $\tilde{\delta} = 28$, about a third of what we would expect in the Milky Way; we adopt it as our fiducial model.

Like M82, the GeV-TeV results are not significantly affected by assuming a mixture of primary electrons and positrons instead of primary electrons.

Results for MeV γ-rays – Much like M82 models, the pionic and bremsstrahlung emission concentrates power at 100 MeV and above, and leptonic emission at lower energies is relatively weak, especially if B is high. The small $\tilde{\delta}$ even in our fiducial model increases the amount of leptonic emission. However, the small scale heights (and thus, high gas densities) selected pushes that leptonic emission into bremsstrahlung. Thus, the 1 - 100 MeV emission is even weaker relative to the pionic emission than in M82. In our fiducial ($B = 400\ \mu$G) model, we find a 1 - 100 MeV luminosity of 2.1×10^{39} ergs s^{-1} and a 0.1 - 10 GeV luminosity of 1.4×10^{40} ergs s^{-1}. The νL_ν luminosity at 1 MeV is just 2% that at 1 GeV.

The low B models of course have stronger MeV emission

---

[8] Throughout the paper, we use the terms "core" and "starburst" for NGC 253 interchangeably, to refer to the modelled regions within 150 pc of its center.

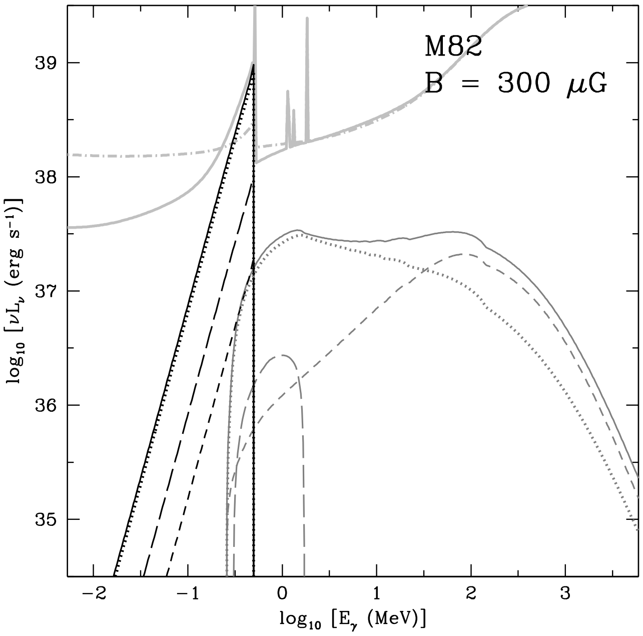

FIG. 6.— The continuum positron annihilation radiation (thin solid), both positronium continuum (black) and in-flight annihilation (grey), for the best-fit $B = 300$ μG model of M82 where half of the primary $e^\pm$ are positrons. The contributions from hadronic e^+ are short-dashed; nucleosynthetic e^+ from supernovae are long-dashed, and the possible primary component is dotted. The supposed primary positron component dominates the low energy e^+ population, although hadronic in-flight radiation dominates over 30 MeV. Nucleosynthetic e^+ dominate over the hadronic e^+ below 1 MeV. For comparison, the total emission from M82 in this model is shown as the thick solid light grey line. Also shown in the total emission for the fiducial $B = 300$ μG model with no primary positrons (thick dot-dashed grey line); the low energy continuum shape is different because a higher $\gamma_{\rm max}^{\rm prim}$ is preferred slightly by our fitting, resulting in a much higher synchrotron contribution.

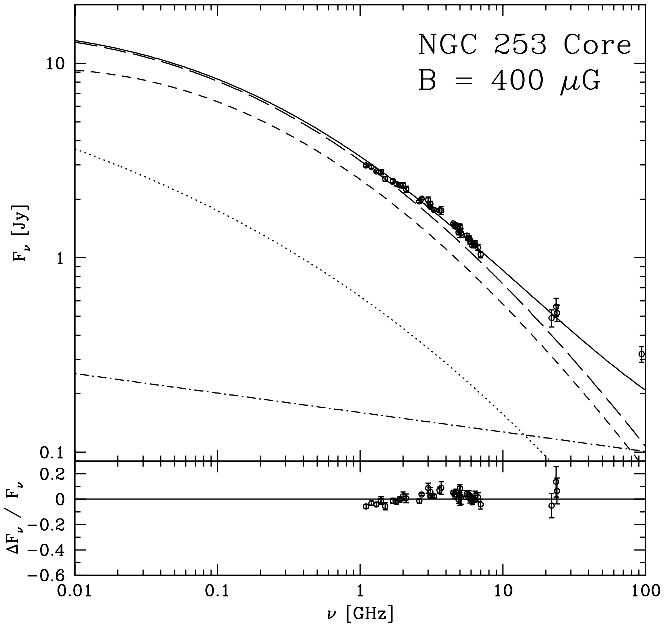

FIG. 7.— Predicted radio spectrum of NGC 253's starburst in the best-fit $B = 400$ μG model with no primary positrons. Plotted lines are total radio emission (solid), total synchrotron emission (long-dashed), synchrotron from secondaries (short-dashed), synchrotron from primaries (dotted), and free-free emission (dash-dotted). Plotted data are the interferometric data compiled in Williams & Bower (2010) (open circles). The bottom panel shows the residuals to the radio data.

(Figure 8): with no primary positrons, the 1 - 100 MeV luminosity is 2.3×10^{40} ergs s^{-1} and the 0.1 - 1 GeV luminosity is 3.0×10^{40} ergs s^{-1}.

Like M82, the higher proton calorimetric efficiency enhances the positron annihilation rate per unit star-formation, with about $1/3$ as many hadronic positrons as nucleosynthetic positrons in our fiducial model. In the fiducial model, positrons annihilating near rest contribute 1.4×10^{37} ergs s^{-1} through positronium continuum and 511 keV line emission, and relativistic positrons contribute an additional 5.5×10^{37} ergs s^{-1}. Thus, positron annihilation does not significantly increase the total MeV luminosity, although it may dominate near 511 keV. Models with primary positrons have much higher annihilation luminosities: for $B = 400$ μG, annihilation near rest produces 1.2×10^{38} ergs s^{-1} and in-flight annihilation produces 1.1×10^{38} ergs s^{-1}; for $B = 50$ μG, annihilation near rest produces 2.7×10^{39} ergs s^{-1}, while in-flight annihilation produces 1.2×10^{39} ergs s^{-1}.

We list the strengths of the γ-ray lines in Table 2. The strongest is the ^{26}Al 1.809 MeV line, with a luminosity of 2.7×10^{37} ergs s^{-1}. None of the lines are expected to contribute significantly to the MeV luminosity of NGC 253, or be detectable with planned instruments. Note that there is significant star-formation outside the starburst of NGC 253 and in the main disk, which will enhance the unresolved line fluxes by a factor $\lesssim 2$ (Melo et al. 2002).

High z – As with M82, the high magnetic field and starlight energy densities limit the influence of the CMB to very high redshifts. At $z = 4.9$, the 100 keV emission of the fiducial model is enhanced by 60% and the 1 MeV emission in enhanced by a third. The CMB has a greater effect in the 50 μG model, enhancing the 100 keV emission by 90% at $z = 4.9$ and the 1 MeV emission by 50%.

3.5. *Brief Summary*

The starbursts of M82 and NGC 253 are more luminous per unit star-formation than the Milky Way at GeV energies, but this is due to strong pion losses for protons, leading to a prominent pion bump in the "high *B*" models. At present, we have essentially no MeV data for starbursts, so we cannot empirically rule out leptonic "low *B*" models with strong MeV emission, though these require strange parameter choices. Compared to the high-*B* starburst models, the Milky Way has a higher MeV/GeV ratio, due to relatively efficient conversion of primary e^- energy into IC and bremsstrahlung radiation. If it is placed at high z, the Milky Way's MeV–GeV spectrum becomes flat from increased Inverse Compton losses off the CMB. We therefore *a priori* do not expect either starbursts (with their prominent pion bumps) or normal galaxies (which are relatively dim at GeV to begin with) to be particularly strong MeV sources.

4. MeV EMISSION FROM INTERGALACTIC CASCADES

Even if the γ-ray spectra of star-forming galaxies were purely pionic, MeV emission is produced during the propagation of γ-rays from distant star-forming galaxies to Earth through the cascade process. About half of the star-formation in the Universe occurs before $z \approx 1$. At these distances, the Universe is opaque above 100 GeV from pair production processes ($\gamma + \gamma \rightarrow e^+ + e^-$) on the infrared Extragalactic Background Light (EBL; Stecker et al. 1992; Gilmore et al. 2009; Finke et al. 2010). The $e^\pm$ have a typical energy comparable

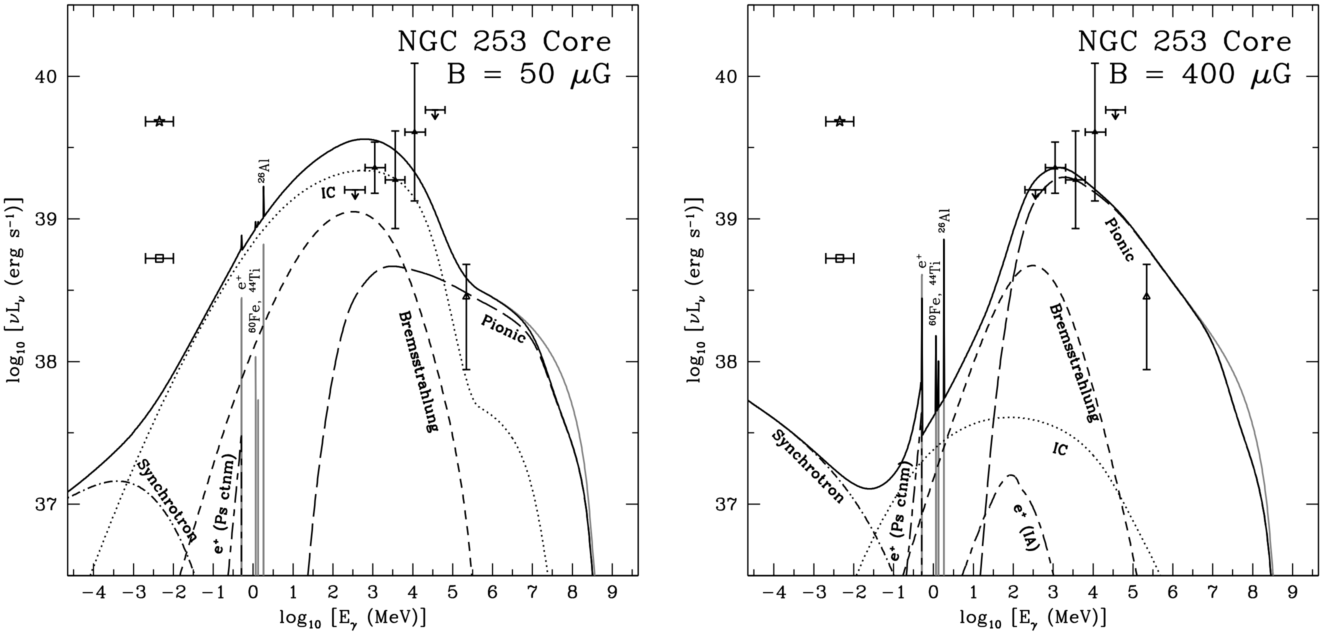

FIG. 8.— The predicted γ-ray luminosity spectrum of NGC 253's starburst, compared to X-ray (Cappi et al. 1999; Bauer et al. 2008) and γ-ray (Abdo et al. 2010f; Acero et al. 2009) observations. The different components to the emission are synchrotron (dash/dotted), positron annihilation (long-dashed/short-dashed), nucleosynthetic γ-ray lines (grey lines), bremsstrahlung (short-dashed), IC (dotted), and pionic emission (long-dashed). The total emission are the solid lines, black including $\gamma\gamma$ absorption on the sightline to Earth and grey without it. The plotted models show the case for when primary $e^\pm$ are purely electrons, with no primary positrons. Emission from CCSNe is not included. The X-ray emission mostly comes from X-ray binaries and thermal emission from gas and is not included in our fitting. As in Figure 2, note the different energy binnings for the different lines.

to the original γ-ray, and cool mainly by Inverse Compton scattering of the CMB.

The typical rest-frame energy of upscattered CMB light is then

$$E''_\gamma \approx 32\,\mathrm{MeV}(1+z)\left(\frac{E_e}{100\,\mathrm{GeV}}\right)^2, \qquad (8)$$

where z is the redshift where the scattering takes place. Thus intergalactic cascades shift energy from TeV bands, where pionic emission can be important, to MeV bands. Normal star-forming galaxies have a pionic spectrum that goes as $E^{-2.7}$, with little γ-ray emission above 100 GeV, so they will contribute little cascade emission. Starburst galaxies, on the other hand, are observed to have hard $E^{-2.2}$ spectra between GeV and TeV energies. Nearly $1/3$ of their $\geq$ GeV luminosity is above 100 GeV and can be affected by the cascade process.

Recently, Broderick et al. (2012) have proposed that plasma instabilities alter the evolution of cascades from bright TeV sources like blazars. These instabilities would effectively stop $e^\pm$ before they could radiate IC, and quench all of the cascade emission. However, the TeV luminosities required for this process are much higher than from M82 and NGC 253. Chang et al. (2012) conclude that only HyperLIRGs would be affected by the plasma instability by assuming that the IR/γ-ray ratio is the same as in M82 and NGC 253. We note that purely proton calorimetric galaxies would be expected to have IR/γ-ray ratios $\sim 2-3$ times higher than M82 and NGC 253's starburst, and so TeV emission from brighter ULIRGs (which are numerous at $z \approx 2$) may not cascade. However, since most star-forming galaxies are relatively faint, we ignore the effects of plasma instabilities.

4.1. *Calculation of Cascade Radiation*

Suppose the star-forming galaxy lies at redshift z_s and emits a spectrum $dN_\gamma^{\rm source}/dE'$ over some time interval. Then the cascade spectrum observed at redshift $z_{\rm obs}$ can be calculated as

$$\frac{dN_{\rm casc}}{dE''_\gamma}(E''_\gamma, z_{\rm obs}) = \int_{z_{\rm obs}}^{z_s} dz \int_0^{E_\gamma(1+z)/(1+z_{\rm obs})} \frac{dN_e}{dz\,dE''_e}\,\frac{dQ_{\rm IC}}{dE''_\gamma}(E''_e, E''_\gamma) \times t_{\rm life}\exp(-\tau_{\gamma\gamma}(E_\gamma, z_{\rm obs}, z))\,dE''_e \qquad (9)$$

where $E''_\gamma = (1+z)E_\gamma$ is the cascade-frame energy, $E'_\gamma = (1+z_{\rm obs})E_\gamma$ is the source-frame energy, and E_γ is the Earth-frame energy. The key ingredients in this calculation are $dN_e/(dE''_e dz)$, the spectrum of pair $e^\pm$ generated in the redshift step z to $z-dz$ from both the primary γ-ray spectrum and the cascade γ-rays at previous redshift steps; $dQ_{\rm IC}/dE_\gamma(E_e, E_\gamma)$, the IC emission at E_γ from one CR $e^\pm$ of energy E_e; $t_{\rm IC}$, the IC cooling time for $e^\pm$; and $\tau_{\gamma\gamma}(E_\gamma, z_{\rm obs}, z)$, the $\gamma\gamma$ optical depth to a photon observed at E_γ from redshift $z_{\rm obs}$ to z.

Accurate source functions for pair production are given in Aharonian et al. (1983) and Böttcher & Schlickeiser (1997). We consider the emission from star-forming galaxies at redshift z_s separately. We then calculate the cascade emission in redshift steps, each from z_i to $z_i - dz$. At each step, the input photon spectrum (in the cascade rest frame) is

$$\frac{dN_\gamma}{dE''_\gamma} = \frac{dN_\gamma^{\rm source}}{dE'_\gamma}\,\frac{1+z_s}{1+z}\exp(-\tau_{\gamma\gamma}(z_{\rm obs}, z)) + \frac{dN_{\rm casc}}{dE''_\gamma}(E''_\gamma, z) \qquad (10)$$

which includes both the attenuated primary spectrum and the attenuated cascade spectrum from previous redshift steps. Within the redshift step, the UV-IR background effectively forms a screen to the γ-rays with optical depth:

$$\Delta\tau_{\gamma\gamma} = \tau_{\gamma\gamma}(E''_\gamma, z_i - \Delta z_i, z_i) \qquad (11)$$

So the generated pairs are calculated as

$$\frac{dN_e}{dz\,dE''_e} = \int \frac{dN_\gamma}{dE''_\gamma}\,\frac{dQ_e(E''_\gamma)}{dE''_e}\,\frac{dt}{dz}\,\frac{1-\exp[-\Delta\tau_{\gamma\gamma}]}{\Delta\tau_{\gamma\gamma}}\,dE''_\gamma, \qquad (12)$$

where $dQ(E''_\gamma)/dE''_e$ is the rate at which pair $e^\pm$ at energy E_e are produced by a photon of energy E_γ, dt/dz puts the redshift step in terms of time. The exponential term guarantees energy conservation even if the Universe is opaque through the redshift step; in the limit of large τ the $dz(dt/dz)(1-\exp(-\tau))/(\tau)$ expression reduces simply to the timescale for photon-photon annihilation.[9] Böttcher & Schlickeiser (1997) give the Aharonian et al. (1983) expression for the rate of $e^\pm$ pair production per high energy photon of energy $\varepsilon_1 m_e c^2$ as:

$$\frac{dQ_e(E''_\gamma)}{dE''_e} = \frac{3}{16}\frac{c\sigma_T}{m_e c^2}\int_{\frac{\varepsilon_1}{4\gamma(\varepsilon_1-\gamma)}}^{\infty} d\varepsilon_2\frac{1}{(\varepsilon_2)^2}\frac{dn_{\rm back}}{d\varepsilon_2}\times \left[\frac{4\varepsilon_1^2}{\gamma(\varepsilon_1-\gamma)}\ln\left(\frac{4\varepsilon_2\gamma(\varepsilon_1-\gamma)}{\varepsilon_1}\right)-8\varepsilon_1\varepsilon_2 +\frac{2(2\varepsilon_1\varepsilon_2-1)\varepsilon_1^2}{\gamma(\varepsilon_1-\gamma)}-\left(1-\frac{1}{\varepsilon_1\varepsilon_2}\right)\frac{\varepsilon_1^4}{\gamma^2(\varepsilon_1-\gamma)^2}\right] \tag{13}$$

where ε_2 is the cascade-frame energy of a background photon in units of $m_e c^2$ and $dn_{\rm back}/d\varepsilon_2$ is the cascade-frame number spectrum of background photons.[10]

The rate of Inverse Compton cascade emission from each pair $e^\pm$ is calculated as

$$\frac{dQ_{\rm IC}}{dE''_\gamma} = cE''_\gamma\int_0^\infty d\epsilon'\frac{dn(\epsilon',z)}{d\epsilon'}\sigma_{\rm IC}(E''_\gamma,\epsilon',E_e) \tag{14}$$

where $dn(\epsilon',z)/d\epsilon'$ is the rest-frame background radiation spectrum at redshift z and rest-frame energy ϵ' (Schlickeiser 2002). The IC cross section is equal to

$$\sigma_{\rm IC}(E_\gamma,\epsilon',E_e) = \frac{3\sigma_T}{4\epsilon'\gamma^2}\left[2q\ln q+(1+2q)(1-q)+\frac{(\Gamma_e q)^2(1-q)}{2(1+\Gamma_e q)}\right] \tag{15}$$

with $q = E_\gamma/[\Gamma_e(E_e-E_\gamma]$ $(1/(4\gamma^2)\le q\le 1)$ and $\Gamma_e = 4\epsilon'\gamma/(mc^2)$ (Schlickeiser 2002).

In the intergalactic medium, electrons and positrons are mainly cooled by Inverse Compton losses and the adiabatic losses from the expansion of the Universe (again ignoring any plasma instability losses). The electron lifetime to Inverse Compton emission is

$$t_{\rm IC}(E''_e) = E''_e\left[\int_0^\infty E''_\gamma\frac{dQ_{\rm IC}}{dE''_\gamma}dE''_\gamma\right]^{-1}, \tag{16}$$

while the loss time due to the expansion of the Universe are simply

$$t_H = [H_0\sqrt{\Omega_M(1+z)^3+\Omega_\Lambda}]^{-1}. \tag{17}$$

The final $e^\pm$ lifetime is then just found as $t_{\rm life}^{-1} = t_{\rm IC}^{-1}+t_H^{-1}$.

4.2. *Results of Cascade Calculation*

The effects of cascades on the spectra of Milky Way-like galaxies is in fact negligible, as expected. However, cascades do have a small but noticeable effect on the spectrum of our high-B M82 spectra, as shown in Figure 9. Cascade emission makes up $\sim$ 10% of the 100 MeV - 10 GeV emission of starburst galaxies at $z = 2$. There is a spectral downturn below 100 MeV, however the intrinsic emission of these models falls even faster because of the pion bump. Thus, the fraction of emission due to cascades peaks near $\sim$ 10 MeV, where it makes up about a third of the observed emission from starbursts.

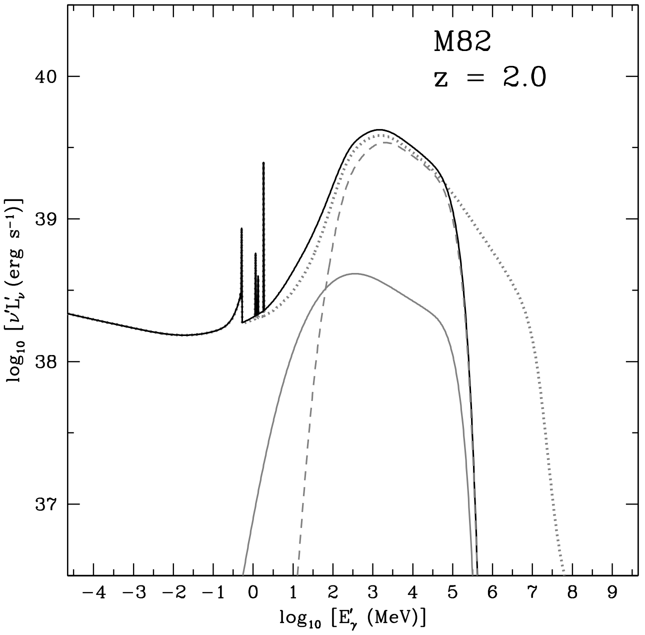

FIG. 9.— The effects of intergalactic cascades on M82's apparent rest-frame spectrum shape, for the fiducial model placed at $z = 2$. The grey dotted line is the unpropagated input spectrum (after absorption within M82 itself), the grey solid line is the cascade emission, and the solid black line is the attenuated plus cascade emission. For comparison, the unpropagated pionic spectrum is shown as a dashed grey line. The cascade spectrum sticks out of the pion bump, but is less strong than the leptonic emission.

We conclude that cascade emission alters the MeV spectrum of starburst galaxies at high z, but nowhere near enough to fill in the pion bump by itself.

5. CONSTRAINTS ON COSMIC MeV EMISSION FROM STAR-FORMING GALAXIES

5.1. *Using the templates to predict the background*

The number density of γ-rays observed at energy E_γ is

$$\frac{dn}{dE_\gamma}(E_\gamma) = \int dt\frac{d^2q_{\rm com}}{dV_{\rm com}dE_\gamma} \tag{18}$$

where $dt = dz/[H_0(1+z)\sqrt{\Omega_\Lambda+\Omega_M(1+z)^3}]$ describes the lookback time, $V_{\rm com}$ is the comoving volume, and $d^2q_{\rm com}/dV_{\rm com}dE_\gamma$ is the injection rate of γ-rays per unit volume per unit observed energy. The number density is converted into a photon flux by multiplying by $c/(4\pi)$. This gives us

$$\frac{d\Phi}{dE_\gamma}(E_\gamma) = \int_0^{z_{\rm max}} dz\frac{c}{4\pi H_0(1+z)[\Omega_M(1+z)^3+\Omega_\Lambda]^{1/2}}\frac{d^2q_{\rm com}}{dV_{\rm com}dE_\gamma}. \tag{19}$$

This expression can also be derived using the photon number luminosity distance. The energy flux per (natural) log bin of energy is $\nu I_\nu = E_\gamma^2 d\Phi/dE_\gamma$.

We calculate the injection rate of γ-rays as

$$\frac{d^2q_{\rm com}}{dV_{\rm com}dE_\gamma} = \frac{\rho_{\rm com}^{\rm SFR}(z)f(z)}{\rm SFR_{model}}\frac{dQ}{dE'_\gamma}[E_\gamma(1+z)](1+z), \tag{20}$$

using $\rho_{\rm com}^{\rm SFR}$ is the star-formation rate per unit volume, $f(z)$ is the fraction of star-formation from galaxies like the model galaxy, dQ/dE'_{γ} is the total source-frame photon generation rate in the model galaxy (after cascades), and $\mathrm{SFR}_{\mathrm{model}}$ is the star-formation rate of the model galaxy. The comoving star-formation rate comes from Hopkins & Beacom (2006).

---

[9] The term comes from the time-averaged mean of the photon flux within the redshift step, which goes as $\int_0^{\Delta\tau} e^{-\tau}d\tau \,/\, \int_0^{\Delta\tau} d\tau$.

[10] Note that formulas 26 and 32 of Böttcher & Schlickeiser (1997) are for electrons only, not for both electrons and positrons (Böttcher, personal communication; Aharonian & Khangulyan, personal communication).

To compare the predicted background to the observed background, we link together fits to the X-ray background and the GeV background. At X-ray energies, Ajello et al. (2008) fit the X-ray background with a double power law, while at GeV energies, Abdo et al. (2010a) fit the GeV background with a single power law. We connect the two with a power law (linear fit in log E and log νI_{ν}) at intermediate energies, which we take to be 3 to 20 MeV by visual inspection. We use the resulting function to represent the strength of the X-ray–γ-ray background:

$$\nu I_{\nu} = \begin{cases} \dfrac{0.102 E_{\mathrm{keV}}^{2}}{\left(\dfrac{E_{\mathrm{keV}}}{29.99}\right)^{1.32} + \left(\dfrac{E_{\mathrm{keV}}}{29.99}\right)^{2.88}} & (E \leq 3\ \mathrm{MeV}) \\ 1.58 \left(\dfrac{E_{\mathrm{keV}}}{3000}\right)^{0.303} & (3\ \mathrm{MeV} \leq E \leq 20\ \mathrm{MeV}) \\ 1.45 \left(\dfrac{E_{\mathrm{keV}}}{100000}\right)^{-0.41} & (E \geq 20\ \mathrm{MeV}) \end{cases} \tag{21}$$

in units of keV $\mathrm{cm}^{-2}\mathrm{s}^{-1}\mathrm{sr}^{-1}$ for a photon of energy E, with $E_{\mathrm{keV}} = E/\mathrm{keV}$ (Ajello et al. 2008; Abdo et al. 2010a). The function is plotted in Figure 1 (and Figures 10, 11, 12) as the solid dark blue line.

5.2. *The question of the starburst fraction of the cosmic SFR*

A large uncertainty is the fraction of cosmic star-formation history that occurs in starburst galaxies. Indeed, discussions of the starburst contribution to the γ-ray background must be clear about what "starburst" even means for these calculations. For this paper, we simply define starburst as having a similar γ-ray SED (and thus, CR propagation environment) as M82 and NGC 253. In particular, it means (1) similar γ-ray to SFR ratios as M82 and NGC 253's core and (2) hard GeV - TeV γ-ray spectra, from winds and pionic losses. At the high end of starburst fraction estimates, Loeb & Waxman (2006) and Thompson, Quataert, & Waxman (2007) argued that most of the star-formation of the Universe was in proton calorimetric galaxies, and thus, the γ-ray background from starbursts is high. Further down in starburst fraction, Stecker (2007) argued that most of the star-formation at $z < 1$ was in normal galaxies, implying a small γ-ray background from starbursts. At the low end, Stecker & Venters (2011) have recently used semi-analytic models which argue that the fraction of cosmic star-formation in pure merger-driven starbursts is very low, $\sim 1-2\%$ at $z = 0$, $\sim 3\%$ at $z = 1$, and $\sim 5\%$ at $z = 4$ (Hopkins et al. 2010).

There are potential issues with each of these approaches. Loeb & Waxman (2006) and Thompson, Quataert, & Waxman (2007) argue that normal galaxies have ~ 10 times more gas at high z than at low z; therefore they should be ~ 10 times more efficient at pionic losses and nearly proton calorimetric. However, at sufficiently high gas surface densities, advective losses may be strong enough to negate this effect. In fact, the Galactic Center has similar gas surface densities ($\Sigma_g \approx 0.03$ g cm^{-2}), but is in fact *fainter* in γ-rays per unit star-formation than the surrounding Galaxy (Crocker et al. 2011a,b). This is apparently because of a strong wind in the region and also because CRs do not appear to be fully sampling the gas (Crocker et al. 2011b). Therefore, normal galaxies at high z may form stars quickly and have large amounts of gas without having M82-like γ-ray spectra (although the pionic γ-ray spectrum will likely be hard because both pionic and advective losses harden the spectrum). However, galaxies at high z appear to lie on the far-infrared correlation (e.g., Appleton et al. 2004; Garn & Alexander 2009; Sargent et al. 2010; Mao et al. 2011), whereas the Galactic Center does not (Crocker et al. 2011a), which is consistent with CRs in high z galaxies interacting with average density gas and radiating before escaping (Lacki et al. 2010).

The predictions of Stecker & Venters (2011) are based on the semi-analytic models of Hopkins et al. (2010) (H10). In these models, galaxies have a normal star-formation mode most of the time, but have a finite probability of merging; when they merge, they enter into a brief (~ 100 Myr) starburst mode of star-formation whose evolution is guided by gas hydrodynamics simulations. The simulations of Hopkins et al. (2010) do not include processes like stellar bars which may feed the lower luminosity starbursts. For example, M82 (the starburst with the largest γ-ray flux) is interacting with its neighbor M81 and has a compact starburst driven by a stellar bar (Telesco et al. 1991), but is not yet merging, so it might not be counted by H10. Also, a normal galaxy with a high enough gas density and weak enough advective losses will become proton calorimetric and will have a starburst-like γ-ray spectrum, even if it is not formally starbursting. Thus defining starbursts purely as ~ 100 Myr long mergers may underestimate the contribution of starburst-like γ-ray emitters. It is nonetheless likely that the strongest compact starbursts like Arp 220, which arise from true mergers, are a small fraction of the cosmic star-formation rate.

Observationally, a number of lines of evidence point to a starburst fraction of $\sim 10\%$, in terms of star-formation mode. The total core-collapse supernova rate within 10 Mpc is $\sim 0.3-2\ \mathrm{yr}^{-1}$ (e.g., Kochanek et al. 2008; Kistler et al. 2011; Li et al. 2011; Horiuchi et al. 2011). The compact starbursts in M82, NGC 253, and NGC 4945 ($D \approx 3.9$ Mpc) have a total supernova rate of $\sim 0.12\ \mathrm{yr}^{-1}$ from their FIR luminosity (Sanders et al. 2003). Further out, there are nuclear starbursts in NGC 4631 ($D = 7.7$ Mpc) with $\Gamma_{\mathrm{SN}} = 0.01-0.06\ \mathrm{yr}^{-1}$ (Golla 1999), and smaller nuclear starbursts in M51, M83, Maffei 2, NGC 2903, NGC 4736, and IC 342 (Kennicutt 1998). Conservatively assuming a total starburst supernova rate of $0.1\ \mathrm{yr}^{-1}$ within 10 Mpc, we find a starburst fraction of $\sim 5-30\%$. Radio and IR luminosity functions can be fit with two populations of star-forming galaxies, identified as normal galaxies and starbursts (Yun et al. 2001). These luminosity functions indicate that starbursts make up $\sim 10-20\%$ of the star-formation rate at $z \approx 0$ (e.g., Yun et al. 2001; Bothwell et al. 2011). Whether these starbursts are all compact and γ-ray bright like M82 is unclear. Rodighiero et al. (2011) find that only 10% of the cosmic star-formation is in starbursts that lie off the "main sequence" of galaxies, a relation between the star-formation rate and stellar mass (see also Sargent et al. 2012). Hopkins & Hernquist (2010) derive a starburst fraction of $\sim 5-10\%$ by using the surface brightness profiles of spheroidal galaxies. In addition to the compact starbursts at $z \approx 0$, there are the submillimeter galaxies (SMGs) observed at $z \gtrsim 2$. There is still some debate whether SMGs are simply disk galaxies with very high star-formation rates or mergers, but they appear to make up 2 - 10% of the cosmic star formation (e.g., Chapman et al. 2005; Dye et al. 2007; Michałowski et al. 2010). With vast amounts of gas, SMGs

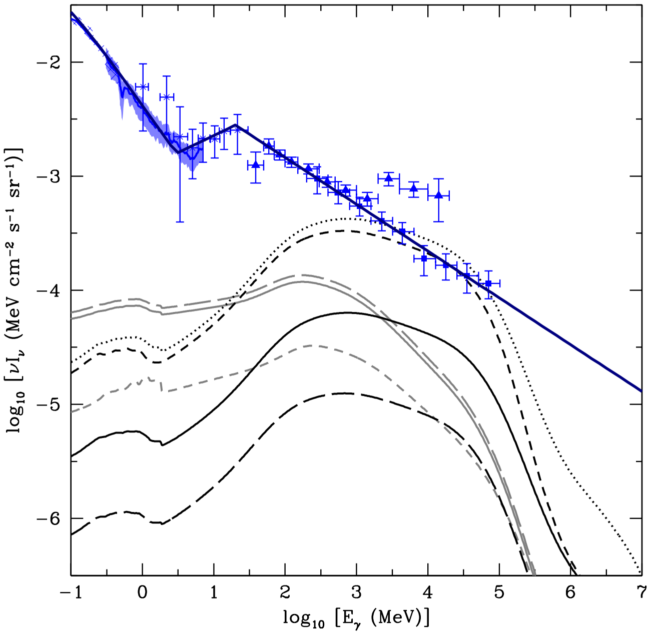

FIG. 10.— The effects of starburst fraction on the predicted γ-ray background. Starbursts (fiducial M82) are in black and normal galaxies (fiducial Milky Way) are in grey. The long-dashed line is the low starburst fraction history, the solid line is the fiducial medium starburst fraction, the short-dashed line is the high starburst fraction, and the dotted line is if all of the star formation is in starbursts. The normal galaxy contribution is only different for the high starburst fraction, whereas the starburst contribution can vary by a factor ~ 30 between the different starburst fractions. The observed γ-ray background is shown in blue.

are likely to have efficient CR proton losses, although their large sizes means that the physical conditions (and therefore leptonic emission) could be different than M82.

In this work, we consider three cases: (1) the low starburst fraction case, calculated by integrating over the Schechter functions given in H10 (similar to the Stecker & Venters 2011 calculation), rising from 1.6% at $z = 0$ to 3.8% at $z = 2$ to 5.1% at $z = 4$ and beyond[11]; (2) a high starburst fraction case as given in Thompson, Quataert, & Waxman (2007); and (3) our fiducial medium starburst fraction case, which is 15% at all redshifts, since that is roughly the geometric mean of the low and high cases and it is fairly close to the ~ 10% that seems to hold at low z. However, without further consideration of the gas evolution in the normal galaxies, we note the fiducial model is not necessarily accurate.

5.3. *The predicted MeV – GeV γ-ray background*

Using the cosmic star-formation rate, assumptions about the contribution of starbursts to the cosmic star-formation history, and our Milky Way and M82 templates, we can tentatively predict the γ-ray background with eqn. 19. We list our results for different galaxy spectral templates and starburst fractions in Table 3.

In general, we find that starburst galaxies have a lot of *absolute* power per unit star-formation at GeV energies, but normal galaxies have much *relative* power per unit star-formation at MeV energies (Figure 1). Using the fiducial/medium starburst fraction history, we find that normal galaxies contribute $\sim 6-15$% of the 0.1 - 10 GeV background. The normal galaxies then contribute $\sim 2-4$% of the 10 MeV background, $\lesssim 2$% of the 1 MeV background, and $\sim 0.1-0.2$% of the 100 keV background (neglecting discrete hard X-ray sources in these galaxies). Note that this drop-off in the γ-ray background contribution by two orders of magnitude is not largely due to the pion bump: as can be seen in Figure 1, νI_ν for fiducial normal galaxies only drops off by a factor ~ 2 from 0.1 to 100 MeV. The discrepancy arises instead because the γ-ray background is steeply falling with energy.

The starburst contribution to the γ-ray background depends on the uncertain contribution of starbursts to the cosmic star-formation rate (§ 5.2 and Figure 10) and, for MeV energies in particular, the magnetic field strengths of the starbursts. We find the starburst contribution at 1 – 100 GeV is only $\sim 0.7-8$% with the low starburst fraction, $\sim 4-41$% with the medium starburst fraction, and from $\sim 16-200$% with the high starburst fraction (Table 3). However, the starburst contribution rapidly falls off at lower energies because of the prominent pion bump: with the medium starburst fraction and the fiducial M82 spectral template, the contribution falls to 2.8% at 100 MeV, 0.4% at 10 MeV, 0.1% at 1 MeV, and 0.01% at 100 keV (again, ignoring discrete sources within the galaxies). Note that the pion bump in high B models does not mean that starbursts are MeV dim per unit star-formation compared to normal galaxies; it arises because starbursts are GeV-TeV *bright* through their higher proton calorimetry fraction. Of course, in the leptonic $B = 50$ μG models, the starburst contribution at MeV energies is much higher: $8-13$% at 100 MeV, $4-6$% at 10 MeV, $1-2$% at 1 MeV, and $0.08-0.3$% at 100 keV or the medium starburst history.

The γ-ray lines, whether from CCSNe, e^+ annihilation from nucleosynthetic positrons, or unstable isotopes in the ISM, do not constitute the majority of the MeV contribution from star-forming galaxies; continuum processes are the dominant source of MeV luminosity of star-forming galaxies. The lines do make up $\sim 1/4$ of the star-forming galaxy contribution at 0.5 MeV and $\gtrsim 10$% from $\sim 0.2-1$ MeV. The fraction of the MeV emission from star-forming galaxies from the transient CCSNe emission peaks at ~ 17% at 0.4 MeV. The exception is in non-standard low B models of starbursts where half of the primary $e^\pm$ are positrons; the large number of primary positrons enhances the positron annihilation flux enormously.

It is interesting that, with the medium starburst fraction history, the fiducial GeV emission from star-forming galaxies has a similar shape to the *Fermi* observed GeV background (Figure 1). We find our fiducial background has a 1 – 30 GeV spectral slope of $\Gamma_{1-30} = 2.40$, compared to 2.41 for the observed background (Abdo et al. 2010a). The predicted and observed spectrum only strongly diverge at energies below those observed with *Fermi*-LAT, where the other backgrounds are measured with different instruments. However, this similarity of the GeV spectra is sensitive to the starburst fraction: for the low starburst fraction, the predicted γ-ray background from star-forming galaxies ($\Gamma_{1-30} = 2.55$) is softer than the observed spectrum; for high starburst fraction, the predicted γ-ray background from star-forming galaxies ($\Gamma_{1-30} = 2.27$) is harder than the observed spectrum (see Figure 10). Thus the apparent similarity may be coincidental.

Summarizing our fiducial results, we find that starbursts and normal galaxies contribute roughly equally to the 1 GeV background (~ 17% each), with starbursts being more important at higher energies, but normal galaxies being much more important at MeV energies.

However, there are a number of caveats with this prediction. Most importantly, we have assumed that there are only two types of galaxies: those like the Milky Way, and those like M82. Essentially, we assume that the only kind of gas density evolution is the evolution of the starburst fraction. However, normal star-forming galaxies like the Milky Way had higher gas densities and star-formation rates (and therefore radiation fields) in the past. Very weak starbursts like the Galactic Center region may have hard TeV γ-ray spectra like M82 and NGC 253, but very low γ-ray luminosities because of winds. Very extreme starbursts like Arp 220 would probably be true proton calorimeters and be even more efficient at producing γ-rays than M82 and NGC 253's core, although these are a small fraction of the cosmic star-formation rate. Submillimeter galaxies have larger gas scale heights; if the CRs samples this gas evenly, Inverse Compton will be enhanced relative to bremsstrahlung. Finally, we have ignored IC emission from $e^{\pm}$ that have escaped normal galaxies, which will increase their MeV emission at low z.

---

[11] Since the H10 luminosity functions are not designed for use at $z > 4$, we use the $z = 4$ starburst fraction at these redshifts.

Comparison with previous predictions – As a check, we can compare our predictions to other recent predictions of the cosmic GeV background.

Using the high starburst fraction history, Thompson, Quataert, & Waxman (2007) predicted that $\sim$ 20% of the Fermi 1 GeV γ-ray background ($\sim$ 10% of the EGRET GeV background) is from starbursts. We in fact predict $\sim 3-9$ times more GeV γ-rays with the T07 starburst history; with the fiducial starburst template, starbursts make up 58% of the *Fermi* 1 GeV background. The difference arises because Thompson, Quataert, & Waxman (2007) assumed much smaller values of η than we find, thus underpredicting the γ-ray luminosity of M82 and NGC 253. Lacki et al. (2011) noted this effect and argued that a high starburst fraction would lead to a $\geq$ GeV starburst contribution of order $\sim$ 50%, more in line with our predictions here.

The pre-*Fermi* calculation of Bhattacharya & Sreekumar (2009) essentially scales the γ-ray luminosity of a galaxy to its TIR luminosity (roughly proportional to the star-formation rate), with different constants of proportionality for normal galaxies and starbursts, an approach comparable to ours. They find the total γ-ray background by integrating over infrared luminosity functions. They find that only $\sim$ 1% of the $\geq$ 0.1 GeV background is from normal galaxies. This is probably because they used the luminosity functions of Lagache et al. (2003), in which normal galaxies make up only a small fraction of the cosmic star-formation rate at high z. (For comparison, the T07 starburst fraction gives us a $\sim$ 2% normal galaxy contribution to the 100 MeV γ-ray background.) They also used a hard $E^{-2.2}$ spectrum for normal galaxies, although that only increases their predictions. They predict the starburst contribution to be $\lesssim$ 6%; the small estimate likely arises because they derive (ultimately from equipartition arguments about M82's radio luminosity from Akyuz et al. 1991, with a volume scaling applied) that $L_{\rm GeV}/L_{\rm IR}$ is only 30% higher for starbursts than for normal galaxies, whereas the *Fermi* observations indicate $L_{\rm GeV}/L_{\rm IR}$ is about 5 - 10 times higher.

Fields et al. (2010) calculated the pionic γ-ray background from normal star-forming galaxies, relating the γ-ray emissivity of a galaxy to its gas mass, which in turn is related to the star-formation rate of a galaxy through the Schmidt Law and empirical trends in the average radius of galaxies. Their varying assumptions about what drives the evolution in the cosmic star-formation rate lead to predictions that normal galaxies are at least $\sim$ 20% and possibly all of the unresolved γ-ray background. Because they used $\mathrm{SFR_{MW}} = 1\ M_{\odot}\ \mathrm{yr}^{-1}$, their normal galaxy contribution to the γ-ray background is twice as large as we would predict. After taking this into account, the "density evolution" case of Fields et al. (2010) gives similar prediction of the normal galaxy contribution as us, while the "luminosity evolution" case with increased gas masses at high z predicts a higher normal galaxy contribution. The increased gas masses might make high-z normal galaxies as proton calorimetric as starbursts, in which case the luminosity evolution case predicts a similar contribution to the GeV background as the "starbursts" in our high starburst fraction model.

Makiya et al. (2011) predicted that $\sim$ 5% of the $\geq$ 100 MeV γ-ray background is from (mostly normal) star-forming galaxies, if the γ-ray luminosity per unit star-formation is the same as in the Milky Way (as we assume). This is somewhat lower than our prediction of $6-17$% of the $0.1-10$ GeV background coming from normal galaxies. They also find that if gas evolution is taken into account, the contribution increases to $\sim$ 10%. By using the Mitaka models of galaxy evolution (Nagashima & Yoshii 2004; Nagashima et al. 2005) and by approximating the starburst galaxy spectrum with the Milky Way spectrum plus a power law, Makiya et al. (2011) also calculated the starburst contribution to GeV background. They found the starburst contribution was small, about 1% of 100 MeV background and a few percent of the 100 GeV background. According to the Mitaka models, starbursts are only a few percent of the $z \approx 1$ star-formation rate (Nagashima et al. 2005), which is of the same order as our low starburst fraction (H10). By comparison, we find using the H10 starbust fraction that starbursts are $\sim 0.6-1$% of the 100 MeV background and $2-4$% of the 1 GeV background, for the fiducial high B models for M82 and NGC 253's core.

Stecker & Venters (2011) performed a similar calculation of the GeV background from star-forming galaxies to Makiya et al. (2011), although they used the H10 galaxy evolution models, and they assumed that starbursts had a soft, Milky Way-like spectrum. They found that normal star-forming galaxies were anywhere between $\sim$ 10% and all of the GeV background depending on how the γ-ray luminosity scales with star-formation rate and/or gas mass. Since they include the effects of gas evolution for normal galaxies, it is natural that their results would be higher than ours. They find a starburst contribution peaking at $\sim$ 1% to the GeV background, which is somewhat lower than our results for an H10 star-formation rate, and dropping off more quickly at high energies than we predict because of the soft γ-ray spectrum they used.

Overall, given the differing methods of other calculations and some large uncertainties in the input parameters (particularly the starburst fraction), our results are broadly consistent with previous predictions.

We also note that Chakraborty & Fields (2012), concurrently to our paper, have recently presented a calculation of the γ-ray background from IC and pionic emission from normal galaxies.

5.4. *Constraints from spectral shape*

The star-forming galaxy contribution to the GeV γ-ray background remains unclear, despite the detection of several star-forming galaxies (both normal and starburst) by *Fermi*. In addition, our predictions rely on assumptions about the star-formation rate of the model galaxies, and the Milky Way

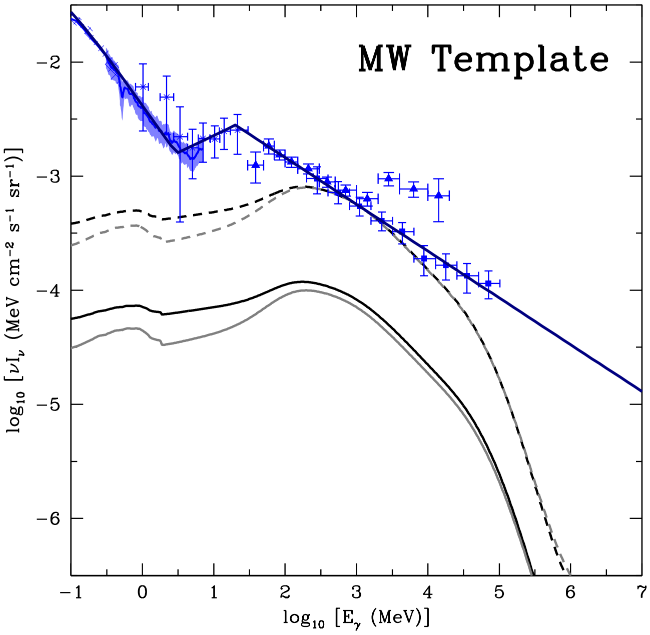

FIG. 11.— Predicted γ-ray background from normal galaxies (solid) using our medium starburst fraction with the $h = 1000$ pc (grey) and the $h = 2000$ pc (black) models, as compared with the observed γ-ray background (blue). Also shown are the spectrum normalized to fit the observed background (dashed). Another large component at energies below 100 MeV and a component at energies above 10 GeV are needed to get the shape of the background correct.

needs an additional scaling factor to match its known γ-ray luminosity. However, star-forming galaxies obviously contribute $\leq 100\%$ of the GeV background. Assuming we know the SED of star-forming galaxies from MeV to GeV energy ranges, we can therefore set an upper limit on the star-forming galaxy contribution to the MeV background by normalizing the SED so it touches but never exceeds the GeV background.

Table 4 lists the maximum fractions of the observed MeV background using different models normalized to the observed GeV background at $E_{\rm norm}$.

The shape of the normal galaxy γ-ray SED is incompatible with normal galaxies being the majority of the MeV background, even with the increased leptonic emission from the CMB at high z. The shape of the spectrum constrains normal galaxies to be a half or less of the 100 MeV background, $\lesssim 25\%$ of the 30 MeV background, $\lesssim 10-20\%$ of the 10 MeV background, and $\lesssim 10\%$ of the 1 MeV background. Note that even these values require the normal galaxy contribution to be scaled up by a factor $\sim 6-25$. The discrepancy in shape is shown in Figure 11: there is a large hump of additional energy near 10 MeV that normal galaxies cannot explain.

For starburst galaxies, the MeV contribution is typically even smaller, although the exact fraction of the MeV background depends on the magnetic field strength. The contribution from starbursts does not need to be multiplied by much (factor $\lesssim 2$) to account for the GeV background, as long as the starburst fraction is high; with the medium starburst fraction, the emission must be scaled up by a factor $\sim 2-7$ to reach the GeV background. In high B (hadronic) models, starbursts are less than $3-5\%$ percent of the 30 MeV background and only $\lesssim 2\%$ of the 10 MeV background (black lines in Figure 12). Only a fraction of one percent of the 1 MeV background could be nonthermal emission from high B starburst galaxies. Low B (leptonic) models have larger allowed MeV

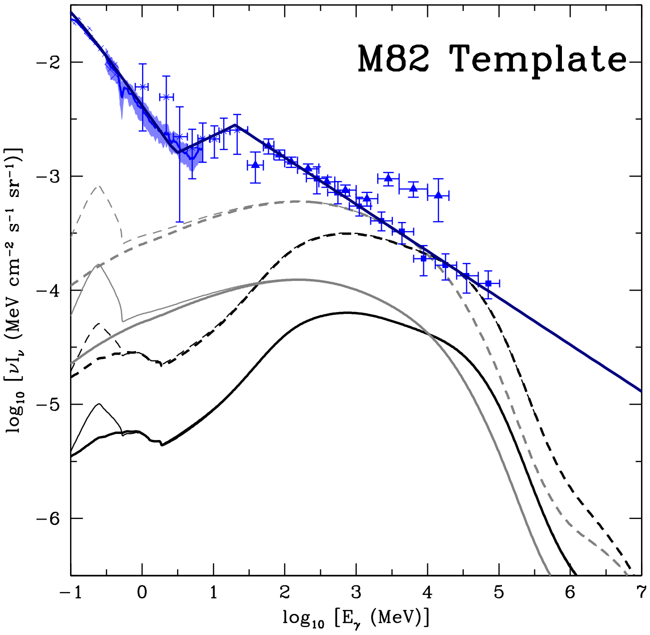

FIG. 12.— Predicted γ-ray background from starbursts (solid) using our medium starburst fraction with the $B = 300$ μG (black) and $B = 50$ μG (grey) best-fit models of M82. The thick lines assume that primary $e^\pm$ are all electrons, while the thin lines are if the primary $e^\pm$ are half positrons, half electrons. The observed γ-ray background is shown in blue. The dashed lines are the predicted spectra normalized to fit the observed background. Below 10 GeV, another very large component is needed to get the shape of the background correct.

fractions, but still make up a small minority of the MeV background: $\lesssim 15-25\%$ of the 30 MeV background, $\lesssim 10-20\%$ of the 10 MeV background, and $\lesssim 3-8\%$ of the 1 MeV background (grey lines in Figure 12). Including inflight positron annihilation radiation from primary positrons increases the 1 MeV contribution, but not enough to be a major contributor of the background. As Figure 12 shows, starbursts cannot be the main source of the MeV background either.

We therefore conclude that star-forming galaxies cannot make up a significant portion of the MeV background, even if the overall γ-ray production efficiency is much higher than we suppose. Either (1) some other source of MeV emitters is needed, (2) some unknown emission process make star-forming galaxies much brighter in MeV emission than we expect (and much brighter per unit star-formation than the Milky Way appears to be), or (3) the claimed cosmic MeV background is incorrect.

6. CONCLUSIONS

The origin of the MeV background remains mysterious, assuming the claimed intensity of the background is correct. Star-forming galaxies are an attractive source for the GeV background because they are ubiquitous, the physics is at least partly understood (especially in the Milky Way), and several have now been detected by *Fermi* and TeV telescopes. However, most of their GeV emission is likely pionic, and therefore rapidly falls off below ~ 100 MeV; hence this process cannot be responsible for the MeV background. We have considered possible processes that can provide MeV emission, including (1) leptonic Inverse Compton and bremsstrahlung emission produced by CR $e^\pm$ in star-forming galaxies, (2) γ-ray line and positron annihilation radiation, and (3) intergalactic cascades that shift energy from the TeV band to the

MeV-GeV band. The IC is expected to be most important in normal, quiescent galaxies like the Milky Way, because CR protons escape more easily and thus primary CR electrons are more important; furthermore, the growing strength of the CMB radiation field will strengthen IC losses in high z normal galaxies. Intergalactic cascades, conversely, will be more important for starburst galaxies which are observed to have hard spectra extending to the TeV.

We have modeled the Milky Way and the starbursts M82 and NGC 253 placed at various redshifts. From these models, we have assembled the expected spectrum of the γ-ray background, taking into account redshift and intergalactic cascades. Our primary results are:

- The MeV emission of normal galaxies is greatly enhanced by the increased energy density of the CMB at high z. This increases Inverse Compton losses at the expense of other radiation and cooling mechanisms like synchrotron. As a result, the pion bump of normal galaxies is "filled in" at high z (Figure 3).

- Starburst galaxies have relatively low MeV emission compared to their strong GeV emission. The relatively strong proton losses imply a strong pion bump, since there is more power in CR protons than in CR $e^{\pm}$. Cascade emission increases the MeV emission by a factor $\lesssim 2$, nowhere near enough to fill in the pion bump. This conclusion can be altered in "low B" models of starbursts, in which the GeV emission comes mostly from Inverse Compton emission (Figures 5 and 8).

- We find with our "medium" starburst fraction (15% of star-formation at all z) that star-forming galaxies are $\sim 1/3$ of the GeV γ-ray background, with roughly equal contributions from normal galaxies and starbursts (Figure 1). However the effective starburst fraction is highly uncertain and depends on gas evolution in normal galaxies. As the fraction of cosmic star formation in starbursts approaches unity, the observed GeV γ-ray background is produced or even exceeded (Figure 10). Starbursts dominate the γ-ray background at high energies, while normal galaxies dominate at low energies.

- In our fiducial model, star-forming galaxies make up only $\sim 1-2\%$ of the 1 MeV background and $\sim 4\%$ of the 10 MeV background (Figure 1). Much of this emission is IC from normal galaxies, but there are also important contributions from γ-ray lines from CCSNe, positron annihilation, and ^{26}Al decay.

- To account for the uncertainties in γ-ray luminosity normalization, we derive more robust limits on the MeV contribution from the spectral shape of star-forming galaxies. According to these constraints, normal galaxies could make at most half of the 100 MeV background, 25% of the 30 MeV background, and 20% of the 10 MeV background (Figure 11). However, reaching these limits requires the normal galaxy background to be multiplied by a factor ~ 10. Similarly, high B starbursts could make up at most $\sim 15\%$ of the 100 MeV background, 5% of the 30 MeV background, and 2% of the 10 MeV background. If the starburst emission is leptonic ($B \approx 50\ \mu$G), these fractions could be higher, with $\sim 10-20\%$ of the 10 MeV background allowed to be from starbursts (Figure 12).

In short, while star-forming galaxies can (and according to our models, do) provide a substantial fraction of the GeV γ-ray background, they are a minor contributor of the MeV background. The reason why the MeV background cannot be explained by star-forming galaxies is simply that the γ-ray background is *very steep*: a lot more power is required at MeV energies than at GeV energies. Thus, even if star-forming galaxies do have enough luminosity at GeV energies, and even if the spectrum is flat at MeV energies (as is the case for normal galaxies), this is insufficient for the observed background.

Thus, there must be some other explanation for the MeV background. The simplest explanation would be some other source that peaks at MeV energies. But this just again raises the mystery of why the MeV-GeV γ-ray background appears to be a featureless power law if there are different sources responsible at different energies (Stecker & Venters 2011). It is possible this is sheer coincidence. Indeed, something like this happens at GeV energies in our fiducial model: normal galaxies with soft spectra are most important at energies below a few GeV, while starbursts with hard spectra are most important above a few GeV; the sum is a nearly featureless power law with $\Gamma = 2.4$, as observed. Likewise, current blazar models of the γ-ray background invoke a coincidence with soft Flat Spectrum Radio Quasars at low energies and hard BL Lacs at high energies (e.g., Venters & Pavlidou 2011). We should also keep in mind that the featureless power law in Figure 1 is actually for the currently unresolved background. The distinction between unresolved and resolved sources is an experimental one (see the huge sensitivity gap in Figure 13 between COMPTEL and *Fermi*-LAT), not necessarily one with fundamental astrophysical significance. The resolution of sources is much better at GeV energies than MeV energies, and the *resolved* γ-ray blazars would add a large component on top of the unresolved background. Finally, the reported MeV background could simply be incorrect (due to detector backgrounds) or Galactic in origin.

Our conclusions can be evaded if there are extremely high amounts of low energy CRs below the pion production threshold, or extremely large contributions from discrete MeV sources. IC emission from escaping $e^{\pm}$ in the halos around normal galaxies can increase the MeV emission, but since the IC emission is a broad continuum extending to GeV energies, the spectral shape constraints imply that this emission does not make up all of the MeV background. Low energy spikes of CR electrons can enhance the bremsstrahlung and IC emission, but can be constrained with synchrotron radio. An extreme enhancement of MeV nuclei might even increase the nuclear line emission enough to alter the SED, although the ionization rate from these nuclei should also be extreme. Discrete sources are not expected to be dominant, based on observations of the Milky Way, so a new significant MeV source population would have to scale non-linearly with star-formation rate.

There are several indirect tests of our predictions. The relatively strong MeV contribution of normal galaxies arises from increased Inverse Compton losses on the CMB, which comes at the expense of other losses – particularly radio. Thus at high z, it has long been expected that galaxies should be faint compared to expectations from their infrared luminosities (Carilli & Yun 1999; Murphy 2009). In contrast, observations indicate that galaxies lie on the empirical $z = 0$ infrared–radio correlation to relatively high z (e.g., Appleton et al. 2004; Garn & Alexander 2009;

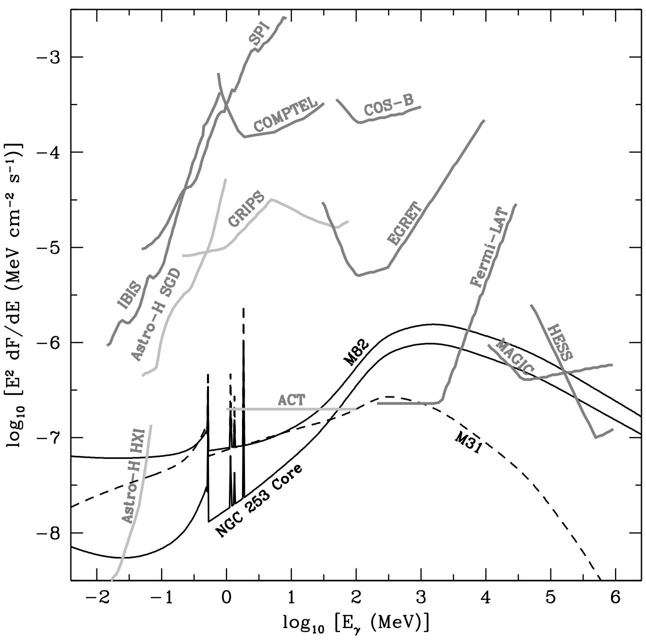

FIG. 13.— Fiducial spectra of M82 and NGC 253's core (black solid) and M31 (black dashed) compared to existing (grey) and proposed (light grey) γ-ray instruments. Even with a 10^3 increase in MeV sensitivity over COMPTEL, detection of these galaxies will be difficult. The sensitivity curves assume exposure times of 10^6 seconds and that $\Delta E = E$, with data taken from Kanbach et al. (2004), Tajima et al. (2005), Bloser et al. (2006), and Greiner et al. (2011). The proposed MEGA instrument would have a similar sensitivity as GRIPS.

Sargent et al. 2010; Mao et al. 2011), or even are radio-bright (e.g., Kovács et al. 2006; Vlahakis et al. 2007; Murphy 2009; Ivison et al. 2010; Michałowski et al. 2010). At high *z*, these observations probe galaxies with high star-formation rates and possibly more starburst like, where the effects of the CMB are expected to be weak. However, new instruments like JVLA and eventually SKA may probe Milky Way–like galaxies, and determine the effects of the stronger CMB.

Further measurements extending the hard X-rays and the high energy γ-rays towards the MeV range may prove constraining for the starbursts. *Fermi*-LAT should ultimately reach down to 30 MeV. At these energies the pion bump should fall off in the high *B* models, but the leptonic emission peaks in the low *B* models. Thus *Fermi*-LAT can help constrain *B* in the nearest starbursts. Further *Fermi*-LAT data will resolve out additional blazars (Abazajian et al. 2011), which would constrain the true contribution of star-forming galaxies to the GeV background and limit their contribution to the MeV background. In the hard X-ray regime, measurements of the 10 - 100 keV luminosity of starbursts would limit their IC emission, helping constrain *B*, and synchrotron emission, which can be significant to $\sim$ 1 MeV in some of our models.

Better MeV instruments may also help us understand the emission mechanisms of γ-rays in this energy range within the Milky Way, particularly the contribution of discrete sources. As noted in section 3.2, both GalProp models and our own models (especially the h = 1000 pc model) fail to predict all of the emission around $\sim$ 10 MeV (Figure 2). The discrepancy is poorly understood, and implies there is something we do not know about galactic MeV emission. The discrepancy by itself cannot explain the MeV background – the Milky Way is less luminous at 10 MeV than at 1 GeV, unlike the background – but it may increase the predicted background by a factor of a few.

However, direct measurements of the 1 - 30 MeV emission of star-forming galaxies beyond the Milky Way and possibly the Magellanic Clouds seem far off. In Figure 13, we plot the fiducial models of M82 and of NGC 253's core compared to the sensitivities of current (grey) and possible future (light grey) γ-ray instruments. In X-rays and GeV-TeV γ-rays, the highly sensitive instruments we have now allow detection of these starbursts. However, COMPTEL, the best instrument over much of the MeV band, is about three orders of magnitude behind *Fermi*-LAT. Nor would proposed next-generation instruments like MEGA (e.g., Bloser et al. 2002, 2006) or GRIPS (Greiner et al. 2011) be able to detect the nonthermal emission from M82 or NGC 253. But even a MeV instrument as sensitive as *Fermi*-LAT, such as ACT (Milne et al. 2002; Boggs 2006), might not detect M82 and NGC 253 from 1 - 10 MeV: the pion bump in the fiducial model means that these galaxies are much fainter in the MeV band than in the GeV band. We also consider M31 by scaling the Milky Way fiducial model to the star-formation rate of M31 (1 $M_\odot$ yr^{-1}; Williams 2003) and using a distance of 780 kpc (Stanek & Garnavich 1998). While M31 has a softer MeV-GeV spectrum, it also has a much lower γ-ray spectrum to begin with, so it too is difficult to detect at MeV energies. Thus, vastly more powerful MeV telescopes are required to directly observe the MeV emission of individual star-forming galaxies; such improvements may be feasible with new γ-ray optics technologies, as in Habs et al. (2012).

The origin of the MeV (and GeV) background can be tested by the anisotropies in the background (Zhang & Beacom 2004). Normal galaxies are expected to have a very weak anisotropy signal (Ando & Pavlidou 2009), while blazars have strong anisotropy signals (Ando et al. 2007). The signal for starbursts has not yet been calculated, but is probably stronger than normal galaxies; anisotropies in the submillimeter associated with submillimeter galaxies have been detected (Amblard et al. 2011). At GeV energies, the strength of the star-forming background is highly sensitive to the starburst fraction; more proton-calorimetric galaxies are brighter in γ-rays. Thus, there might be strong anisotropies in the GeV contribution from star-forming galaxies if starbursts dominate. In the MeV, however, normal galaxies are expected to dominate, and these have very weak anisotropy signals. A future MeV experiment could therefore search for the star-forming galaxy contribution by looking for a uniformly distributed component to the MeV background. Further studies of the starburst contribution to background anisotropies, and a better treatment of galaxy evolution, is necessary to evaluate this effect.

In short, the sheer power of the MeV background as reported requires many luminous sources, and star-forming galaxies simply are not bright enough to be its origin. How the MeV and GeV backgrounds join up so seamlessly is unclear, since star-forming galaxies seem to make up at least $\sim$ 20% and plausibly a majority of the GeV background. Future MeV instruments must be improved, possibly by many orders of magnitude, to solve the riddle of its source.

Note – As we were completing this paper, we became aware of the paper by Chakraborty & Fields (2012) that calculates the contribution of Inverse Compton γ-rays from normal galaxies to the γ-ray background.

We thank Felix Aharonian, Markus Böttcher, Brian Fields, Dmitry Khangulyan, Kohta Murase, Vasiliki Pavlidou, and especially Todd Thompson for discussions. For the second half of this project, BCL was supported by a Jansky fellowship from the National Radio Astronomy Observatory. The National Radio Astronomy Observatory is operated by Associated Universities, Inc., under cooperative agreement with the National Science Foundation. For the first half of this project, BCL was supported in part by an Elizabeth Clay Howald Presidential Fellowship from the OSU. SH is supported by the Center for Cosmology and Astro-Particle Physics (CCAPP) at the OSU. JFB was supported by NSF CAREER Grant PHY-0547102 and NSF Grant PHY-1101216.

APPENDIX

General approach – Our approach to one-zone models is ultimately based on the extensive discussion in Torres (2004), and is described in detail in Lacki et al. (2010) and Lacki & Thompson (2010b).

The population of CRs in galaxies is governed by the diffusion-loss equation:

$$-D\nabla^2 N(E) + \frac{N(E)}{\tau(E)} - \frac{d}{dE}[b(E)N(E)] - Q(E) = -\frac{\partial N(E)}{\partial t} \tag{1}$$

where D is the spatial diffusion constant, $b(E)$ is the sum of all of the energy loss rates, $Q(E)$ is the CR injection rate for CRs at the energy E, $\tau(E)$ includes all catastrophic and escape losses, and $N(E)$ is the CR energy spectrum (see also Strong et al. 2007). Our steady-state one-zone models assume the CR population has no time or spatial dependence within the modeled region, so that the diffusion-loss equation reduces to the leaky box equation:

$$\frac{N(E)}{\tau(E)} - \frac{d}{dE}[b(E)N(E)] - Q(E) = 0. \tag{2}$$

This may be solved by the Green's function method described in Torres (2004).

CR nuclei heavier than hydrogen – In order to estimate the strengths of the CR de-excitation nuclear lines, we treat primary helium-4, carbon-12, and oxygen-16 ions in addition to protons, electrons, and positrons. However, secondary nuclei are not included.

We normalize these nuclei by the ratio of their rigidity spectra with CR protons' rigidity spectrum, comparing at equal rigidities. For our momentum power law spectra $dQ/dq = Cq^{-p}$, it can be shown that

$$\frac{C_i}{C_p} = \frac{(dQ/dR)_i}{(dQ/dR)_H}\left(\frac{Z_i}{Z_p}\right)^{p-1}, \tag{3}$$

where $R = qc/(Ze)$ is the rigidity, and Z is the electric charge of the nucleus ($Z_p = 1$). The ratio of the helium-4 and hydrogen rigidity spectra is assumed to be 8, as observed in the Milky Way (Webber & Lezniak 1974; Webber et al. 1987). The abundances of carbon and oxygen are then normalized to helium-4 using the values in Meyer et al. (1998).

Heavier nuclei can interact with gas in the ISM and not only produce pions, but undergo nuclear reactions as well. To calculate these lifetimes, we use a modified version of the inelastic cross sections of Letaw et al. (1983). The cross section for interactions of CR nuclei and ISM protons is

$$\sigma_{\rm inel}^{pZ}(E) = 45A_{\rm CR}^{0.7}[1+0.016\,\sin(5.3-2.63\ln A_{\rm CR})][1-0.62e^{-K/200\,{\rm MeV}}\sin(10.9(K/{\rm MeV})^{-0.28})]\ {\rm mb} \tag{4}$$

for CRs with an atomic mass $A_{\rm CR}$ and kinetic energies K above 10 MeV. For interactions between CR nuclei and ISM helium nuclei, we replace the $A_{\rm CR}^{0.7}$ term with $[4^{0.35} + A_{\rm CR}^{0.35} - 1]^2$ to get a cross section $\sigma_{\rm inel}^{\alpha Z}(E)$, by analogy with the Glauber rule. The lifetime of a CR nucleus to nuclear reactions is then

$$t_{\rm nuclear} = [(\sigma_{\rm inel}^{pZ}(E)n_H + \sigma_{\rm inel}^{\alpha Z}(E)n_{\rm He})\beta c]^{-1}, \tag{5}$$

where βc is the speed of the CR.

Pionic emission from nuclei – While pionic cross sections for proton-proton collisions are given in Kamae et al. (2006), no cross sections are given for proton-helium or helium-helium collisions in that reference. Since the helium is expected to be a minor contributor to the pionic emission ($\sim$ 10%), we scale the proton-proton cross sections using the Orth & Buffington (1976) approximation:

$$\sigma_\pi^{ZZ}(E_Z) = \sigma_\pi^{pp}(E_Z/A_{\rm CR})[A_{\rm CR}^{3/8} + A_{\rm ISM}^{3/8} - 1]^2 \tag{6}$$

which is applied to the differential cross sections for production of pionic γ-rays, $e^\pm$, and neutrinos.[12] Roughly speaking, this rule takes into account that nuclei are not transparent to hadronic interactions, with some of the nucleons being shadowed by the others.

Nuclear lines – Nuclei colliding with each other can excite nuclei; the de-excitations then generate γ-ray lines in the rest-frame of the emitting nucleus. There are three different cases: a CR nucleus can hit an ISM proton and become excited, a CR proton can hit an ISM nucleus and excite it, and a CR nucleus can penetrate a dust grain. Excited CR nuclei will generate a broad continuum as their Doppler shift smears out the γ-ray line, whereas excited ISM nuclei will generate a narrow line. We neglect the dust grain case, but it would generate an even narrower line as energy losses in the dust grain dampened the nuclear recoil.

Following Meneguzzi & Reeves (1975), we calculate the line emissivity of CR nuclei on ISM p/α collisions as

$$\frac{dQ}{dE} = \frac{1}{2}\sum_{k,i} n_k \int dE' \int_{E''_{\rm min}}^{E''_{\rm max}} dE'' \frac{dN_i}{dE'}(E') c\sigma_{ki}(E') \frac{E''}{\gamma_i' E^2}\delta(E'' - E_L), \tag{7}$$

---

[12] The Orth & Buffington (1976) approximation is also used by the GALPROP code for simulations of the Milky Way (Moskalenko & Strong 1998).

where the emissivity is in units of ph $\mathrm{cm}^{-3}\ \mathrm{s}^{-1}\ \mathrm{ergs}^{-1}$ (contrast with Meneguzzi & Reeves (1975), where it is photons per ISM hydrogen atom per steradian), $E''_{\rm min} = E/(\gamma(1+\beta))$ and $E''_{\rm max} = E/(\gamma(1-\beta))$.

For the line emissivity of CR p/α on ISM nuclei, we use

$$\frac{dQ}{dE} = \sum_{k,i} \frac{n_k}{2\Delta E_L} \int dE' \sigma_{ik}(E') c \beta'_i \frac{dN_i}{dE'}(E') \times (|E - E_L| \leq \Delta E_L). \tag{8}$$

For simplicity, we assume the nuclear line has a line half-width of ΔE_L, which we take to be 40 keV. Since we are interested in the cosmic background, redshift will smooth out narrow features in any case, so the exact line width is not that important.

We use the line cross sections from (Kozlovsky et al. 2002). Included lines are 429 and 478 keV lines from ^{4}He (broad components only since the projectile and target are both the same), 4.438 MeV and 15.1 MeV lines from ^{12}C (where the 4.438 MeV line can be created in collisions with ^{14}N and ^{16}O as well because ^{12}C is created in the collision), and 6.129 MeV, 6.916 MeV, and 7.115 MeV lines from ^{16}O. The 4.438 MeV ^{12}C line is generally expected to be the strongest (Ramaty et al. 1979).

Bremsstrahlung – In this paper, our models use the bremsstrahlung cross sections from Strong et al. (2000a). An electron with kinetic energy K_e interacts with an atom of number Z and atomic mass N, produces a photon with energy $k m_e c^2$, and leaves with a kinetic energy $K_e - k m_e c^2 > 0$. We include the effects of hydrogen and helium in the ISM; metals have a negligible effect on the total cross section. Strong et al. (2000a) consider three regimes for the electron kinetic energy: 10 keV - 70 keV, 70 keV - 2 MeV, and more than 2 MeV. They also consider the Fano-Sauter limit when $E_\gamma \approx K_e$, because the other approximations to the bremsstrahlung cross section drop off too quickly. We use the Fano-Sauter limit when it gives a bigger cross section than the other approximations, although we find in practice this only happens when $k m_e c^2$ is very nearly K_e.

The bremsstrahlung loss time is then calculated by directly integrating up the cross sections:

$$-\frac{dE}{dt} = c \sum_j n_j \int_0^E dE_\gamma \frac{E_\gamma}{m_e c^2} \frac{d\sigma_j(E_\gamma, E_e)}{dk} \tag{9}$$

(Schlickeiser 2002).

Positron annihilation – Positrons have a small but significant probability of annihilating in-flight, before thermalizing. The positron annihilation cross section is given as

$$\sigma_{\rm ann} = \frac{2\pi r_0^2}{\tau^2(\tau-4)} \left((\tau^2 + 4\tau - 8) \log \frac{\sqrt{\tau} + \sqrt{\tau-4}}{\sqrt{\tau} - \sqrt{\tau-4}} - (\tau+4)\sqrt{\tau(\tau-4)} \right) \tag{10}$$

where $\tau = 2(1+\gamma)$ (e.g., Beacom & Yüksel 2006; Vietri 2008). Then the in-flight annihilation time is $(n_e \sigma_{\rm ann} \beta_e c)^{-1}$, where n_e is the number density of both free and bound electrons.

The inflight annihilation spectrum is then

$$\frac{dQ_{\rm ann}(\epsilon_\gamma)}{d\epsilon_\gamma} = \frac{3\sigma_T^2 c n_e}{8\gamma_+ p_+} \left[\left(\frac{\epsilon_\gamma}{\gamma_+ + 1 - \epsilon_\gamma} + \frac{\gamma_+ + 1 - \epsilon_\gamma}{\epsilon_\gamma} \right) + 2\left(\frac{1}{\epsilon_\gamma} + \frac{1}{\gamma_+ + 1 - \epsilon_\gamma} \right) - \left(\frac{1}{\epsilon_\gamma} + \frac{1}{\gamma_+ + 1 - \epsilon_\gamma} \right)^2 \right]. \tag{11}$$

where $\epsilon_\gamma = E_\gamma/(m_e c^2)$, $p_+ = \sqrt{\gamma_e^2 - 1}$, and $\gamma_+ \geq (1 - 2\epsilon_\gamma + 2\epsilon_\gamma^2)/(2\epsilon_\gamma - 1)$ (e.g., Aharonian 2004).

Positrons are more likely to cool by ionization and annihilate after thermalizing than at relativistic speeds. Positrons are conveyed towards rest in energy space at a "speed" $|dE/dt|$. The rate at which positrons annihilate at low energies in equilibrium is therefore $Q_+^{\rm surv} = dN/dE \times |dE/dt| \times f_{\rm surv}(E)$, where $f_{\rm surv}(E)$ is the probability that positrons survive cooling to rest without being catastrophically lost (through inflight annihilation or escape). We take our lowest energy bin (with kinetic energy K_0 = 100 keV) and assume $f_{\rm surv}(K_0) = 1$ to calculate the positron annihilation rate as

$$Q_+^{\rm surv} = \frac{dN}{dE}(K_0) b(K_0). \tag{12}$$

Note that this is not the rate at which positrons are injected at all energies: positrons can escape the system through diffusive and advective losses at high energy and avoid annihilation, or annihilate in-flight.

Annihilation at rest can either occur through direct annihilation or through positronium formation. Direct annihilation leads to two 511 keV line photons. Positronium formation, which occurs $f_{\rm Ps} \approx 90-95\%$ of the time in the Milky Way, also leads to two 511 keV line photons about 1/4 of the time. We arbitrarily assume a line half-width of $\Delta E = 5$ keV (which will be smeared out for galaxies at different z anyway) to calculate the 511 keV annihilation line from CR positrons as:

$$\frac{dQ}{dE} = \frac{(1 - 3 f_{\rm Ps}/4) Q_+^{\rm surv}}{2\Delta E} \tag{13}$$

We assume $f_{\rm Ps} = 0.9$ for this work. Positronium annihilates into three photons with a continuum distribution of energies below 511 keV 3/4 of the time. The positronium continuum spectrum is given in Ore & Powell (1949) and Guessoum et al. (1991):

$$\frac{dQ}{dE} = \frac{6}{(\pi^2 - 9) m_e c^2} \left[\frac{\epsilon(1-\epsilon)}{(2-\epsilon)^2} + \frac{2(1-\epsilon)}{\epsilon^2} \log(1-\epsilon) - 2\frac{(1-\epsilon)^2}{(2-\epsilon)^3} \log(1-\epsilon) + \frac{2-\epsilon}{\epsilon} \right] \times \frac{3 Q_+^{\rm surv} f_{\rm Ps}}{4}, \tag{14}$$

where $\epsilon = E/(m_e c^2)$ and we have already taken into account that each annihilation produces three photons.

$\gamma\gamma$ *Absorption* – At TeV energies, $\gamma\gamma$ absorption process may become important. This process converts γ-rays into $e^{\pm}$, which can radiate in Inverse Compton (Inoue 2011b) or synchrotron (Lacki & Thompson 2010b). The interior γ-ray photon density is calculated using the uniform slab model, where the absorbing and emitting regions are cospatial:

$$N_{\gamma} = \frac{Q_{\gamma} h}{c\tau_{\gamma\gamma}(h)}[1 - \exp(-\tau_{\gamma\gamma}(h))] \tag{15}$$

where Q_{γ} is the rate at which γ-rays are injected per unit volume, h is the midplane-to-edge scale height, and $\tau_{\gamma\gamma}(h)$ is the midplane-to-edge optical depth to $\gamma\gamma$ absorption. To calculate $\tau_{\gamma\gamma}(h) = h \int n(\epsilon)\sigma_{\gamma\gamma}(\epsilon, E_{\gamma})d\epsilon$ for a radiation field $n(\epsilon)$, we use the approximation for the $\gamma\gamma$ cross sections $\sigma_{\gamma\gamma}(\epsilon, E_{\gamma})$ given in Aharonian (2004). The spectrum of these pairs is then calculated using the Aharonian et al. (1983) source functions.

For the Earth-observed spectrum, we again use a uniform slab model, but substitute the galaxy radius R for h, since the Milky Way, M82, and NGC 253 are all viewed nearly edge-on:

$$F_{\gamma}^{\oplus} = F_{\gamma}^{\mathrm{unabs}}[1 - \exp(-\tau_{\gamma\gamma}(R))]/\tau_{\gamma\gamma}(R). \tag{16}$$

where $F_{\gamma}^{\mathrm{unabs}}$ is the unabsorbed γ-ray flux.

Finally when constructing the background, we assume that a galaxy is typically observed face-on. This means that the sightline within the disk will typically have length of order $\sim h$. However, the radiation field of a galaxy extends out to a distance $\sim R > h$. Thus γ-rays in the halo of the galaxy/starburst may be absorbed by the $\gamma\gamma$ process. The pair $e^{\pm}$ in the halo will not radiate in bremsstrahlung; though they will radiate IC and possibly synchrotron, depending on how far out the magnetic field extends. To be conservative we do not include any emission from these halo $e^{\pm}$. Instead, we apply the uniform slab model with sightline h to the galaxy itself, and then treat the halo as a foreground screen of length R:

$$F_{\gamma}^{\mathrm{back}}(E_{\gamma}) = F_{\gamma}^{\mathrm{unabs}} \frac{1 - \exp(-\tau_{\gamma\gamma}(h))}{\tau_{\gamma\gamma}(h)} \exp(-\tau_{\gamma\gamma}(R)), \tag{17}$$

where we assume the radiation field is constant out to a radius R.

REFERENCES

Abdo, A. A., et al. 2008, ApJ, 688, 1078
Abdo, A. A., Ackermann, M., Ajello, M., et al. 2009, Physical Review Letters, 103, 251101
Abdo, A. A., et al. 2010a, Physical Review Letters, 104, 101101
Abdo, A. A., et al. 2010b, ApJ, 720, 435
Abdo, A. A., et al. 2010c, A&A, 512, A7
Abdo, A. A., et al. 2010d, A&A, 523, A46
Abdo, A. A., et al. 2010e, A&A, 523, L2
Abdo, A. A., et al. 2010f, ApJ, 709, L152
Abdo, A. A., et al. 2010g, ApJ, 715, 429
Abazajian, K. N., Blanchet, S., & Harding, J. P. 2011, Phys. Rev. D, 84, 103007
Acero, F., et al. 2009, Science, 326, 1080
Acciari, V. A., et al. 2009, Nature, 462, 770
Agaronyan, F. A., Atoyan, A. M., & Nagapetyan, A. M. 1983, Astrophysics, 19, 187
Aharonian, F. A., & Atoyan, A. M. 2000, A&A, 362, 937
Aharonian, F. A. 2004, *Very high energy cosmic gamma radiation : a crucial window on the extreme Universe*, (River Edge, NJ: World Scientific Publishing)
Aharonian, F., Akhperjanian, A. G., Barres de Almeida, U., et al. 2008, Physical Review Letters, 101, 261104
Aharonian, F., et al. 2009, A&A, 508, 561
Ahn, K., Komatsu, E., Höflich, P. 2005, Phys. Rev. D, 71, 121301
Ahn, K., & Komatsu, E. 2005, Phys. Rev. D, 72, 061301
Ajello, M., Greiner, J., Sato, G., et al. 2008, ApJ, 689, 666
Ajello, M., et al. 2009, ApJ, 699, 603
Akyuz, A., Brouillet, N., & Ozel, M. E. 1991, A&A, 248, 419
Amblard, A., Cooray, A., Serra, P., et al. 2011, Nature, 470, 510
Ando, S., Komatsu, E., Narumoto, T., & Totani, T. 2007, MNRAS, 376, 1635
Ando, S., & Pavlidou, V. 2009, MNRAS, 400, 2122
Appleton, P. N., et al. 2004, ApJS, 154, 147
Arnett, W. D., & Fu, A. 1989, ApJ, 340, 396
Baldry, I. K., & Glazebrook, K. 2003, ApJ, 593, 258
Bauer, M., Pietsch, W., Trinchieri, G., Breitschwerdt, D., Ehle, M., Freyberg, M. J., & Read, A. M. 2008, A&A, 489, 1029
Beacom, J. F., Yüksel, H. 2006, Physical Review Letters, 97, 071102
Beck, R. 2011, Space Sci. Rev., 135
Berezhko, E. G., & Ellison, D. C. 1999, ApJ, 526, 385
Bergström, L., Edsjö, J., & Ullio, P. 2001, Physical Review Letters, 87, 251301
Bertone, G., Buchmüller, W., Covi, L., & Ibarra, A. 2007, JCAP, 11, 3
Bhattacharya, D., et al. 1994, ApJ, 437, 173
Bhattacharya, D., & Sreekumar, P. 2009, Research in Astronomy and Astrophysics, 9, 509
Blasi, P., Gabici, S., & Vannoni, G. 2005, MNRAS, 361, 907
Bloemen, H., et al. 1994, A&A, 281, L5
Bloemen, H., et al. 1995, A&A, 293, L1
Bloemen, H., et al. 1999, ApJ, 521, L137
Bloser, P. F., Andritschke, R., Kanbach, G., et al. 2002, New Astron. Rev., 46, 611
Bloser, P. F., Ryan, J. M., McConnell, M. L., et al. 2006, Chinese Journal of Astronomy and Astrophysics Supplement, 6, 010000
Boggs, S. E. 2006, New Astron. Rev., 50, 604
Bothwell, M. S., et al. 2011, MNRAS, 832
Böttcher, M., & Schlickeiser, R. 1997, A&A, 325, 866
Bouchet, P., & Danziger, I. J. 1993, A&A, 273, 451
Bouchet, L., Jourdain, E., Roques, J.-P., Strong, A., Diehl, R., Lebrun, F., & Terrier, R. 2008, ApJ, 679, 1315
Bouchet, L., Strong, A. W., Porter, T. A., et al. 2011, ApJ, 739, 29
Boulares, A., & Cox, D. P. 1990, ApJ, 365, 544
Bradford, C. M., Nikola, T., Stacey, G. J., Bolatto, A. D., Jackson, J. M., Savage, M. L., Davidson, J. A., & Higdon, S. J. 2003, ApJ, 586, 891
Broderick, A. E., Chang, P., & Pfrommer, C. 2012, ApJ, 752, 22
Cappi, M., et al. 1999, A&A, 350, 777
Carilli, C. L., & Yun, M. S. 1999, ApJ, 513, L13
Catchpole, R. M., Whitelock, P. A., Feast, M. W., et al. 1988, MNRAS, 231, 75P
Chakraborty, N., & Fields, B. D. 2012, arXiv e-prints
Chang, P., Broderick, A. E., & Pfrommer, C. 2012, ApJ, 752, 23
Chapman, S. C., Blain, A. W., Smail, I., & Ivison, R. J. 2005, ApJ, 622, 772
Chomiuk, L., & Povich, M. S. 2011, AJ, 142, 197
Chugai, N. N., Chevalier, R. A., Kirshner, R. P., & Challis, P. M. 1997, ApJ, 483, 925
Clayton, D. D., & Silk, J. 1969, ApJ, 158, L43
Clayton, D. D., & Ward, R. A. 1975, ApJ, 198, 241
Colafrancesco, S., & Blasi, P. 1998, Astroparticle Physics, 9, 227
Connell, J. J. 1998, ApJ, 501, L59
Coppi, P. S., & Aharonian, F. A. 1997, ApJ, 487, L9
Crocker, R. M., Jones, D. I., Aharonian, F., Law, C. J., Melia, F., & Ott, J. 2011a, MNRAS, 411, L11
Crocker, R. M., Jones, D. I., Aharonian, F., Law, C. J., Melia, F., Oka, T., & Ott, J. 2011b, MNRAS, 413, 763
Cusumano, G., et al. 2010, A&A, 524, A64
Dar, A., & Shaviv, N. J. 1995, Physical Review Letters, 75, 3052

de Cea del Pozo, E., Torres, D. F., & Rodriguez Marrero, A. Y. 2009a, ApJ, 698, 1054

de Cea del Pozo, E., Torres, D. F., Rodriguez, A. Y., & Reimer, O. 2009b, arXiv:0912.3497

del Rio, E., et al. 1996, A&A, 315, 237

Dermer, C. D., Bland-Hawthorn, J., Chiang, J., & McNaron-Brown, K. 1997, ApJ, 484, L121

Dermer, C. D. 2007, ApJ, 659, 958

Diehl, R., et al. 1995, A&A, 298, 445

Diehl, R., et al. 2006a, Nature, 439, 45

Diehl, R., et al. 2006b, A&A, 449, 1025

Domingo-Santamaría, E. & Torres, D. F. 2005, A&A444, 403.

Dye, S., Eales, S. A., Ashby, M. L. N., Huang, J.-S., Egami, E., Brodwin, M., Lilly, S., & Webb, T. 2007, MNRAS, 375, 725

Ellison, D. C., Berezhko, E. G., & Baring, M. G. 2000, ApJ, 540, 292

Faucher-Giguère, C.-A., & Loeb, A. 2010, JCAP, 1, 5

Feldmann, R., Hooper, D., & Gnedin, N. Y. 2012, arXiv:1205.0249

Fields, B. D., Pavlidou, V., & Prodanović, T. 2010, ApJ, 722, L199

Finke, J. D., Razzaque, S., & Dermer, C. D. 2010, ApJ, 712, 238

Fransson, C., & Kozma, C. 2002, New Astronomy Review, 46, 487

Freedman, W. L., et al. 1994, ApJ, 427, 628

Garn, T., & Alexander, P. 2009, MNRAS, 394, 105

Gehrels, N., MacCallum, C. J., & Leventhal, M. 1987, ApJ, 320, L19

Ghirlanda, G., Ghisellini, G., Tavecchio, F., Foschini, L., & Bonnoli, G. 2011, MNRAS, 418

Gilli, R., Comastri, A., & Hasinger, G. 2007, A&A, 463, 79

Gilmore, R. C., Madau, P., Primack, J. R., Somerville, R. S., & Haardt, F. 2009, MNRAS, 399, 1694

Ginzburg, V. L., & Ptuskin, V. S. 1976, Reviews of Modern Physics, 48, 161

Giommi, P., Colafrancesco, S., Cavazzuti, E., Perri, M., & Pittori, C. 2006, A&A, 445, 843

Goetz, M., Downes, D., Greve, A., & McKeith, C. D. 1990, A&A, 240, 52

Goldshmidt, O., & Rephaeli, Y. 1995, ApJ, 444, 113

Golla, G. 1999, A&A, 345, 778

Greiner, J., Mannheim, K., Aharonian, F., et al. 2011, Experimental Astronomy, 73

Guessoum, N., Ramaty, R., & Lingenfelter, R. E. 1991, ApJ, 378, 170

Habs, D., Günther, M. M., Jentschel, M., & Urban, W. 2012, Physical Review Letters, 108, 184802

Hamuy, M. 2003, ApJ, 582, 905

Harris, M. J., et al. 2005, A&A, 433, L49

Harrison, A., Henkel, C., & Russell, A. 1999, MNRAS, 303, 157

Hopkins, A. M., & Beacom, J. F. 2006, ApJ, 651, 142

Hopkins, P. F., Younger, J. D., Hayward, C. C., Narayanan, D., & Hernquist, L. 2010, MNRAS, 402, 1693

Hopkins, P. F., & Hernquist, L. 2010, MNRAS, 402, 985

Horiuchi, S., & Beacom, J. F. 2010, ApJ, 723, 329

Horiuchi, S., Beacom, J. F., Kochanek, C. S., et al. 2011, ApJ, 738, 154

Hunter, S. D., Bertsch, D. L., Catelli, J. R., et al. 1997, ApJ, 481, 205

Indriolo, N., Fields, B. D., & McCall, B. J. 2009, ApJ, 694, 257

Inoue, Y., Totani, T., & Ueda, Y. 2008, ApJ, 672, L5

Inoue, Y., & Totani, T. 2009, ApJ, 702, 523

Inoue, Y. 2011a, ApJ, 733, 66

Inoue, Y. 2011b, ApJ, 728, 11

Ivison, R. J., et al. 2010, MNRAS, 402, 245

Iwabuchi, K., & Kumagai, S. 2001, PASJ, 53, 669

Iyudin, A. F., Diehl, R., Bloemen, H., et al. 1994, A&A, 284, L1

Jerkstrand, A., Fransson, C., & Kozma, C. 2011, A&A, 530, A45

Jose, J., Hernanz, M., & Coc, A. 1997, ApJ, 479, L55

Kamae, T., Karlsson, N., Mizuno, T., Abe, T., & Koi, T. 2006, ApJ, 647, 692

Kanbach, G., Andritschke, R., Schopper, F., et al. 2004, New Astronomy Review, 48, 275

Kennicutt, R. C., Jr. 1998, ApJ, 498, 541

Keshet, U., Waxman, E., Loeb, A., Springel, V., & Hernquist, L. 2003, ApJ, 585, 128

Keshet, U., Waxman, E., & Loeb, A. 2004, JCAP, 4, 6

Kistler, M. D., Yüksel, H., Ando, S., Beacom, J. F., & Suzuki, Y. 2011, Phys. Rev. D, 83, 123008

Klein, U., Wielebinski, R., & Morsi, H. W. 1988, A&A, 190, 41

Knödlseder, J. 1999, ApJ, 510, 915

Knödlseder, J., et al. 1999, A&A, 344, 68

Kochanek, C. S., Beacom, J. F., Kistler, M. D., et al. 2008, ApJ, 684, 1336

Kovács, A., Chapman, S. C., Dowell, C. D., Blain, A. W., Ivison, R. J., Smail, I., & Phillips, T. G. 2006, ApJ, 650, 592

Kozlovsky, B., Murphy, R. J., & Ramaty, R. 2002, ApJS, 141, 523

Lacki, B. C., & Thompson, T. A. 2010a, ApJ, 717, 196

Lacki, B. C., & Thompson, T. A. 2010b, arXiv:1010.3030

Lacki, B. C., Thompson, T. A., & Quataert, E. 2010, ApJ, 717, 1

Lacki, B. C., Thompson, T. A., Quataert, E., Loeb, A., & Waxman, E. 2011, ApJ, 734, 107

Lagache, G., Dole, H., & Puget, J.-L. 2003, MNRAS, 338, 555

Lenain, J.-P., Ricci, C., Türler, M., Dorner, D., & Walter, R. 2010, A&A, 524, A72

Letaw, J. R., Silberberg, R., & Tsao, C. H. 1983, ApJS, 51, 271

Li, W., Chornock, R., Leaman, J., et al. 2011, MNRAS, 412, 1473

Lichti, G. G., Bignami, G. F., & Paul, J. A. 1978, Ap&SS, 56, 403

Lien, A., & Fields, B. D. 2012, ApJ, 747, 120

Limongi, M., & Chieffi, A. 2006, ApJ, 647, 483

Loeb, A., & Waxman, E. 2000, Nature, 405, 156

Loeb, A. & Waxman, E. 2006, Journal of Cosmology and Astroparticle Physics 5, 3

Mahoney, W. A., Ling, J. C., Wheaton, W. A., & Jacobson, A. S. 1984, ApJ, 286, 578

Makiya, R., Totani, T., & Kobayashi, M. A. R. 2011, ApJ, 728, 158

Malkov, M. A., & O'C Drury, L. 2001, Reports on Progress in Physics, 64, 429

Malyshev, D., & Hogg, D. W. 2011, ApJ, 738, 181

Mao, M. Y., Huynh, M. T., Norris, R. P., et al. 2011, ApJ, 731, 79

Massaro, F., & Ajello, M. 2011, ApJ, 729, L12

Mauersberger, R., Henkel, C., Wielebinski, R., Wiklind, T., & Reuter, H.-P. 1996, A&A, 305, 421

Melo, V. P., Pérez García, A. M., Acosta-Pulido, J. A., Muñoz-Tuñón, C., & Rodríguez Espinosa, J. M. 2002, ApJ, 574, 709

Meneguzzi, M., & Reeves, H. 1975, A&A, 40, 91

Meyer, J.-P., Drury, L. O., & Ellison, D. C. 1998, Space Sci. Rev., 86, 179

Michałowski, M., Hjorth, J., & Watson, D. 2010, A&A, 514, A67

Milne, P. A., Kroeger, R. A., Kurfess, J. D., & The, L.-S. 2002, New Astron. Rev., 46, 617

Miniati, F. 2002, MNRAS, 337, 199

Miyawaki, R., Makishima, K., Yamada, S., Gandhi, P., Mizuno, T., Kubota, A., Tsuru, T. G., & Matsumoto, H. 2009, PASJ, 61, 263

Moskalenko, I. V., & Strong, A. W. 1998, ApJ, 493, 694

Mücke, A., & Pohl, M. 2000, MNRAS, 312, 177

Murase, K., Beacom, J. F., & Takami, H. 2012, arXiv:1205.5755

Murphy, E. J. 2009, ApJ, 706, 482

Murray, N., & Rahman, M. 2010, ApJ, 709, 424

Nagashima, M., & Yoshii, Y. 2004, ApJ, 610, 23

Nagashima, M., Yahagi, H., Enoki, M., Yoshii, Y., & Gouda, N. 2005, ApJ, 634, 26

Nolan, P. L., Abdo, A. A., Ackermann, M., et al. 2012, ApJS, 199, 31

Ohm, S., & Hinton, J. A. 2012, arXiv:1202.0260

Olive, K. A., & Silk, J. 1985, Physical Review Letters, 55, 2362

Ore, A., & Powell, J. L. 1949, Physical Review , 75, 1696

Orth, C. D., & Buffington, A. 1976, ApJ, 206, 312

Padovani, P., Ghisellini, G., Fabian, A. C., & Celotti, A. 1993, MNRAS, 260, L21

Paglione, T. A. D., Marscher, A. P., Jackson, J. M., & Bertsch, D. L. 1996, ApJ, 460, 295

Palacios, A., Meynet, G., Vuissoz, C., et al. 2005, A&A, 429, 613

Parizot, E., & Lehoucq, R. 2002, A&A, 383, 987

Pavlidou, V., & Fields, B. D. 2001, ApJ, 558, 63

Pavlidou, V., & Fields, B. D. 2002, ApJ, 575, L5

Pavlidou, V., & Venters, T. M. 2008, ApJ, 673, 114

Peng, R., Zhou, S., Whiteoak, J. B., Lo, K. Y., & Sutton, E. C. 1996, ApJ, 470, 821

Persic, M., Rephaeli, Y., & Arieli, Y. 2008, A&A 486, 143.

Pohl, M. 1994, A&A, 287, 453

Porter, T. A., Moskalenko, I. V., Strong, A. W., Orlando, E., & Bouchet, L. 2008, ApJ, 682, 400

Prantzos, N., Boehm, C., Bykov, A. M., et al. 2011, Reviews of Modern Physics, 83, 1001

Prodanović, T., & Fields, B. D. 2004, Astroparticle Physics, 21, 627

Prodanović, T., Fields, B. D., & Beacom, J. F. 2007, Astroparticle Physics, 27, 10

Ramaty, R., Kozlovsky, B., & Lingenfelter, R. E. 1979, ApJS, 40, 487

Rekola, R., Richer, M. G., McCall, M. L., Valtonen, M. J., Kotilainen, J. K., & Flynn, C. 2005, MNRAS, 361, 330

Rephaeli, Y., Arieli, Y., & Persic, M. 2010, MNRAS, 401, 473

Revnivtsev, M., Sazonov, S., Churazov, E., Forman, W., Vikhlinin, A., & Sunyaev, R. 2009, Nature, 458, 1142

Robitaille, T. P., & Whitney, B. A. 2010, ApJ, 710, L11

Rodighiero, G., Daddi, E., Baronchelli, I., et al. 2011, ApJ, 739, L40

Ruiz-Lapuente, P., Cassé, M., & Vangioni-Flam, E. 2001, ApJ, 549, 483

Sacher, W., & Schoenfelder, V. 1983, Space Sci. Rev., 36, 249

Sakamoto, K., Mao, R.-Q., Matsushita, S., Peck, A. B., Sawada, T., & Wiedner, M. C. 2011, ApJ, 735, 19

Salamon, M. H., & Stecker, F. W. 1994, ApJ, 430, L21

Sanders, D. B., Mazzarella, J. M., Kim, D.-C., Surace, J. A., & Soifer, B. T. 2003, AJ, 126, 1607

Sargent, M. T., et al. 2010, ApJS, 186, 341

Sargent, M. T., Béthermin, M., Daddi, E., & Elbaz, D. 2012, ApJ, 747, L31

Schlickeiser, R. 1982, A&A, 106, L5

Schlickeiser, R. 2002, Cosmic ray astrophysics, Berlin: Springer

Schröder, R., Schlickeiser, R., & Strong, A. W. 2005, A&A, 442, L45

Seaquist, E. R., & Odegard, N. 1991, ApJ, 369, 320

Singal, J., Petrosian, V., & Ajello, M. 2011, arXiv:1106.3111

Soltan, A. M., & Juchniewicz, J. 1999, Astrophysical Letters Communications, 39, 197

Soltan, A. M., & Marcinkowski, R. 2001, Exploring the Gamma-Ray Universe, 459, 349

Sreekumar, P., et al. 1998, ApJ, 494, 523

Stanek, K. Z., & Garnavich, P. M. 1998, ApJ, 503, L131

Stecker, F. W. 1970, Ap&SS, 6, 377

Stecker, F. W., de Jager, O. C., & Salamon, M. H. 1992, ApJ, 390, L49

Stecker, F. W., Salamon, M. H., & Malkan, M. A. 1993, ApJ, 410, L71

Stecker, F. W., & Salamon, M. H. 1996, ApJ, 464, 600

Stecker, F. W. 2007, Astroparticle Physics, 26, 398

Stecker, F. W., Hunter, S. D., & Kniffen, D. A. 2008, Astroparticle Physics, 29, 25

Stecker, F. W., & Venters, T. M. 2011, ApJ, 736, 40

Strickland, D. K., & Heckman, T. M. 2007, ApJ, 658, 258

Strigari, L. E., Beacom, J. F., Walker, T. P., & Zhang, P. 2005, JCAP, 4, 17

Strong, A. W., Wolfendale, A. W., & Worrall, D. M. 1976, Journal of Physics A, 9, 1553

Strong, A. W., & Moskalenko, I. V. 1998, ApJ, 509, 212

Strong, A. W., Moskalenko, I. V., & Reimer, O. 2000a, ApJ, 537, 763

Strong, A. W., Moskalenko, I. V., & Reimer, O. 2000, American Institute of Physics Conference Series, 510, 283

Strong, A. W., Moskalenko, I. V., & Reimer, O. 2004a, ApJ, 613, 956

Strong, A. W., Moskalenko, I. V., & Reimer, O. 2004b, ApJ, 613, 962

Strong, A. W., Moskalenko, I. V., & Ptuskin, V. S. 2007, Annual Review of Nuclear and Particle Science, 57, 285

Strong, A. W., Porter, T. A., Digel, S. W., Jóhannesson, G., Martin, P., Moskalenko, I. V., Murphy, E. J., & Orlando, E. 2010, ApJ, 722, L58

Tajima, H., Kamae, T., Madejski, G., et al. 2005, IEEE Transactions on Nuclear Science, 52, 2749

Teegarden, B. J., & Watanabe, K. 2006, ApJ, 646, 965

Telesco, C. M., Joy, M., Dietz, K., Decher, R., & Campins, H. 1991, ApJ, 369, 135

Teng, S. H., Mushotzky, R. F., Sambruna, R. M., Davis, D. S., & Reynolds, C. S. 2011, ApJ, 742, 66

The, L.-S., Leising, M. D., & Clayton, D. D. 1993, ApJ, 403, 32

The, L.-S., Clayton, D. D., Diehl, R., et al. 2006, A&A, 450, 1037

Thompson, T. A. et al. 2006a, ApJ, 645, 186

Thompson, T. A., Quataert, E., Waxman, E., & Loeb, A. 2006b, arXiv:astro-ph/0608699

Thompson, T. A., Quataert, E., Waxman, E. 2007, ApJ, 654, 219

Torres, D. F., Reimer, O., Domingo-Santamaría, E., & Digel, S. W. 2004, ApJ, 607, L99

Torres, D. F. 2004, ApJ, 617, 966

Türler, M., Chernyakova, M., Courvoisier, T. J.-L., Lubiński, P., Neronov, A., Produit, N., & Walter, R. 2010, A&A, 512, A49

Turner, J. L., & Ho, P. T. P. 1983, ApJ, 268, L79

Ullio, P., Bergström, L., Edsjö, J., & Lacey, C. 2002, Phys. Rev. D, 66, 123502

Ulvestad, J. S., & Antonucci, R. R. J. 1997, ApJ, 488, 621

Ulvestad, J. S. 2000, AJ, 120, 278

Venters, T. M., & Pavlidou, V. 2011, ApJ, 737, 80

Vietri, M. 2008, Foundations of High-Energy Astrophysics, Chicago: University of Chicago Press

Vink, J., Laming, J. M., Kaastra, J. S., et al. 2001, ApJ, 560, L79

Vlahakis, C., Eales, S., & Dunne, L. 2007, MNRAS, 379, 1042

Völk, H. J. 1989, A&A, 218, 67

Wang, W., et al. 2007, A&A, 469, 1005

Warren, J. S., et al. 2005, ApJ, 634, 376

Watanabe, K., Hartmann, D. H., Leising, M. D., & The, L.-S. 1999, ApJ, 516, 285

Wdowczyk, J., Tkaczyk, W., & Wolfendale, A. W. 1972, Journal of Physics A Mathematical General, 5, 1419

Webber, W. R., & Lezniak, J. A. 1974, Ap&SS, 30, 361

Webber, W. R., Golden, R. L., & Stephens, S. A. 1987, International Cosmic Ray Conference, 1, 325

Webber, W. R., McDonald, F. B., & Lukasiak, A. 2003, ApJ, 599, 582

Weidenspointner, G., Varendorff, M., Kappadath, S. C. et al. 2000, American Institute of Physics Conference Series, 510, 467

Weidenspointner, G., Skinner, G., Jean, P., et al. 2008a, Nature, 451, 159

Weidenspointner, G., Skinner, G. K., Jean, P., et al. 2008b, New Astronomy Review, 52, 454

Weiß, A., Neininger, N., Hüttemeister, S., & Klein, U. 2001, A&A, 365, 571

Williams, B. F. 2003, AJ, 126, 1312

Williams, P. K. G., & Bower, G. C. 2010, ApJ, 710, 1462

Yin, J., Hou, J. L., Prantzos, N., et al. 2009, A&A, 505, 497

Yun, M. S., Reddy, N. A., & Condon, J. J. 2001, ApJ, 554, 803

Zdziarski, A. A., & Lightman, A. P. 1985, ApJ, 294, L79

Zdziarski, A. A. 1996, MNRAS, 281, L9

Zhang, P., & Beacom, J. F. 2004, ApJ, 614, 37

Zhou, M., Wang, J., & Gao, X. 2011, ApJ, 727, L46

TABLE 3
PREDICTED γ-RAY BACKGROUND

Model	Prim. e [a]	$f_{\rm SB}$ [b]	Predicted fraction of γ-ray background										
			100 keV %	300 keV %	1 MeV %	3 MeV %	10 MeV %	30 MeV %	100 MeV %	300 MeV %	1 GeV %	10 GeV %	100 GeV %
Normal Galaxies: Milky Way													
h = 1000 pc	e^-	H10	0.13	0.4	1.2	2.5	2.1	2.7	7.1	12	14	9.7	2.8
		15%	0.11	0.35	1.1	2.2	1.8	2.3	6.2	10	13	8.5	2.5
		T07	0.017	0.065	0.26	0.45	0.41	0.53	1.5	3	3.9	3.1	1.4
h = 2000 pc	e^-	H10	0.23	0.65	2	4.6	3.6	4	8.8	14	17	12	3.3
		15%	0.2	0.57	1.7	4	3.1	3.5	7.7	12	15	10	2.9
		T07	0.031	0.1	0.4	0.85	0.73	0.84	1.9	3.5	4.6	3.9	1.7
Starbursts: M82													
B = 50 μG	e^-	H10	0.017	0.063	0.25	0.87	0.79	0.91	1.7	2.5	3.4	3.5	0.69
		15%	0.082	0.31	1.3	4.3	3.9	4.6	8.4	13	18	19	4.4
		T07	0.45	1.7	6.7	23	21	24	44	67	90	92	16
	$e^{\pm}$	H10	0.053	0.21	0.3	0.96	0.83	0.94	1.7	2.5	3.4	3.5	0.69
		15%	0.22	1.2	1.5	4.8	4.2	4.7	8.5	13	18	19	4.4
		T07	1.3	5.4	7.9	25	22	25	44	67	90	92	16
B = 100 μG	e^-	H10	0.0066	0.026	0.11	0.39	0.41	0.54	1.1	1.8	2.4	2.5	0.86
		15%	0.032	0.13	0.54	1.9	2	2.7	5.7	9.3	13	13	5.5
		T07	0.17	0.69	2.9	10	11	14	30	48	63	64	21
	$e^{\pm}$	H10	0.024	0.098	0.13	0.44	0.43	0.56	1.1	1.8	2.4	2.5	0.86
		15%	0.097	0.56	0.65	2.1	2.1	2.8	5.8	9.4	13	13	5.5
		T07	0.59	2.5	3.4	11	11	15	30	49	63	65	21
B = 150 μG	e^-	H10	0.0038	0.015	0.059	0.2	0.22	0.32	0.78	1.4	2.1	3.3	1.9
		15%	0.018	0.075	0.3	0.99	1.1	1.6	3.9	7.1	11	17	12
		T07	0.1	0.4	1.6	5.4	5.9	8.6	21	37	55	87	45
	$e^{\pm}$	H10	0.012	0.049	0.069	0.22	0.23	0.32	0.77	1.4	2	2.8	1.4
		15%	0.049	0.28	0.35	1.1	1.1	1.6	3.8	7	10	15	8.9
		T07	0.3	1.3	1.8	5.9	6.1	8.5	20	36	53	74	33
B = 200 μG	e^-	H10	0.005	0.015	0.043	0.13	0.14	0.24	0.73	1.5	2.4	3.5	1.7
		15%	0.025	0.073	0.22	0.62	0.69	1.1	3.5	7.4	12	19	11
		T07	0.13	0.38	1.1	3.4	3.8	6.4	19	39	63	93	40
	$e^{\pm}$	H10	0.0073	0.03	0.045	0.14	0.15	0.25	0.73	1.5	2.4	3.5	1.7
		15%	0.03	0.17	0.23	0.67	0.73	1.2	3.6	7.4	12	19	11
		T07	0.18	0.77	1.2	3.6	4	6.5	20	39	63	93	39
B = 250 μG	e^-	H10	0.0038	0.012	0.034	0.094	0.11	0.2	0.64	1.4	2.3	3.8	1.9
		15%	0.019	0.058	0.18	0.45	0.53	0.93	3.1	6.9	12	20	12
		T07	0.099	0.3	0.89	2.5	2.9	5.2	17	36	61	99	45
	$e^{\pm}$	H10	0.0052	0.022	0.034	0.098	0.11	0.2	0.64	1.4	2.3	3.7	1.8
		15%	0.022	0.12	0.17	0.48	0.54	0.93	3.1	6.8	12	19	11
		T07	0.13	0.55	0.9	2.6	3	5.2	17	36	60	96	42
B = 300 μG	e^-	H10	0.0026	0.0088	0.025	0.067	0.083	0.16	0.57	1.3	2.2	3.6	1.8
		15%	0.013	0.044	0.13	0.32	0.39	0.76	2.8	6.3	11	19	11
		T07	0.069	0.23	0.67	1.8	2.2	4.3	15	34	58	95	43
	$e^{\pm}$	H10	0.0033	0.014	0.025	0.069	0.085	0.16	0.57	1.3	2.2	3.6	1.7
		15%	0.014	0.077	0.13	0.33	0.4	0.76	2.8	6.3	11	19	11
		T07	0.084	0.36	0.67	1.8	2.2	4.3	15	33	57	94	41
B = 400 μG	e^-	H10	0.0017	0.0079	0.028	0.095	0.12	0.23	0.75	1.5	2.2	2.9	1.5
		15%	0.0081	0.039	0.15	0.46	0.59	1.1	3.6	7.4	11	15	9.2
		T07	0.045	0.21	0.75	2.5	3.3	6.1	20	39	58	77	35
	$e^{\pm}$	H10	0.017	0.071	0.046	0.12	0.14	0.24	0.75	1.5	2.2	3	1.5
		15%	0.067	0.43	0.24	0.61	0.66	1.1	3.7	7.5	11	15	9.2
		T07	0.42	1.8	1.2	3.3	3.6	6.3	20	39	58	78	35
Starbursts: NGC 253 Core													
B = 50 μG	e^-	H10	0.017	0.067	0.3	1.1	1.1	1.3	2.5	4.2	6.2	7.7	2.4
		15%	0.081	0.32	1.4	5.4	5.3	6.5	13	21	32	41	15
		T07	0.45	1.8	7.8	29	28	34	67	110	160	200	56
	$e^{\pm}$	H10	0.076	0.31	0.37	1.2	1.1	1.3	2.5	4.2	6.2	7.7	2.4
		15%	0.3	1.8	1.8	6.1	5.7	6.7	13	21	32	41	15
		T07	1.9	7.9	9.7	33	30	35	67	110	160	200	56
B = 100 μG	e^-	H10	0.0068	0.028	0.13	0.5	0.55	0.76	1.7	2.9	4.2	5.3	2.4
		15%	0.032	0.14	0.63	2.4	2.7	3.7	8.3	15	22	28	15
		T07	0.18	0.75	3.4	13	15	20	44	76	110	140	57
	$e^{\pm}$	H10	0.035	0.14	0.16	0.58	0.59	0.79	1.7	2.9	4.2	5.4	2.5
		15%	0.14	0.84	0.81	2.8	2.9	3.9	8.4	15	22	28	15
		T07	0.85	3.7	4.3	15	16	21	45	77	110	140	59
B = 150 μG	e^-	H10	0.004	0.017	0.071	0.26	0.3	0.43	1	1.9	2.9	4.4	2.5
		15%	0.019	0.082	0.35	1.3	1.4	2.1	5.1	9.6	15	23	15
		T07	0.11	0.44	1.9	7	7.9	11	27	50	77	120	59
	$e^{\pm}$	H10	0.018	0.075	0.089	0.3	0.32	0.44	1	1.9	2.9	4.4	2.5
		15%	0.072	0.44	0.44	1.5	1.5	2.2	5.2	9.6	15	23	15

TABLE 3 — *Continued*

Model	Prim. e [a]	$f_{\rm SB}$[b]	Predicted fraction of γ-ray background										
			100 keV %	300 keV %	1 MeV %	3 MeV %	10 MeV %	30 MeV %	100 MeV %	300 MeV %	1 GeV %	10 GeV %	100 GeV %
		T07	0.45	1.9	2.3	7.9	8.4	12	28	50	77	120	59
$B = 200\ \mu$G	e^-	H10	0.0035	0.016	0.073	0.31	0.39	0.63	1.7	3	4.3	4.7	1.9
		15%	0.016	0.076	0.36	1.5	1.9	3.1	8.2	15	22	25	12
		T07	0.09	0.42	1.9	8.1	10	17	44	80	110	120	44
	$e^\pm$	H10	0.037	0.13	0.12	0.38	0.43	0.66	1.7	3	4.3	4.7	1.9
		15%	0.16	0.75	0.63	1.9	2.1	3.2	8.3	15	22	25	12
		T07	0.93	3.3	3.3	10	11	17	45	81	110	120	45
$B = 250\ \mu$G	e^-	H10	0.01	0.024	0.068	0.22	0.27	0.48	1.4	2.8	4	4.1	1.5
		15%	0.051	0.12	0.35	1.1	1.3	2.3	7.1	14	21	22	9.8
		T07	0.26	0.64	1.8	5.7	7.3	13	39	73	100	110	36
	$e^\pm$	H10	0.009	0.047	0.042	0.12	0.13	0.22	0.67	1.3	2	2.1	1
		15%	0.044	0.29	0.23	0.64	0.71	1.2	3.6	7.5	11	12	6.8
		T07	0.23	1.2	1.1	3.1	3.5	5.9	18	35	51	53	22
$B = 300\ \mu$G	e^-	H10	0.0022	0.0099	0.04	0.16	0.21	0.39	1.2	2.4	3.8	5.4	2.6
		15%	0.01	0.049	0.2	0.76	1	1.8	5.7	12	19	28	16
		T07	0.057	0.26	1.1	4.2	5.7	10	31	63	100	140	61
	$e^\pm$	H10	0.011	0.047	0.052	0.18	0.23	0.4	1.2	2.4	3.8	5.4	2.6
		15%	0.044	0.27	0.26	0.88	1.1	1.9	5.8	12	19	28	16
		T07	0.27	1.2	1.4	4.8	6.1	11	32	64	100	140	61
$B = 400\ \mu$G	e^-	H10	0.0016	0.0074	0.027	0.1	0.15	0.33	1.2	2.6	4.4	7	3.6
		15%	0.0075	0.037	0.14	0.47	0.72	1.5	5.7	13	22	37	23
		T07	0.042	0.2	0.71	2.7	4.1	8.7	32	69	120	180	85
	$e^\pm$	H10	0.004	0.017	0.03	0.11	0.16	0.33	1.2	2.6	4.4	7	3.6
		15%	0.017	0.098	0.15	0.51	0.74	1.5	5.7	13	22	37	23
		T07	0.1	0.45	0.79	2.8	4.2	8.8	32	69	120	180	85

[a] Denotes whether the primary electrons and positrons in the model are all electrons (e^-) or half electrons and half positrons ($e^\pm$).

[b] Starburst fraction used in the model. H10: our low starburst fraction case, with the starburst fraction in the Hopkins et al. (2010) semianalytic models; 15%: our fiducial medium starburst fraction case, where 15% of the cosmic star formation rate at all z is in starbursts; T07: our high starburst fraction case, using the values in Thompson, Quataert, & Waxman (2007).

TABLE 4
CONSTRAINTS FROM SPECTRAL SHAPE

Model	Prim. e[a]	$f_{\rm SB}$[b]	$E_{\rm norm}$[c] GeV	Scale[d]	Maximum fraction of γ-ray background[e]										
					100 keV %	300 keV %	1 MeV %	3 MeV %	10 MeV %	30 MeV %	100 MeV %	300 MeV %	1 GeV %	10 GeV %	100 GeV %
Normal Galaxies: Milky Way															
h = 1000 pc	e^-	H10	1.1	7	0.9	2.8	8.5	17	15	19	49	83	100	68	20
		15%	1.1	8	0.9	2.8	8.5	17	15	19	49	83	100	68	20
		T07	1.5	25	0.41	1.6	6.6	11	10	13	36	74	98	77	35
h = 2000 pc	e^-	H10	1.1	6	1.4	3.9	12	27	21	24	52	83	100	69	20
		15%	1.1	6.8	1.4	3.9	12	27	21	24	52	83	100	69	20
		T07	1.7	21	0.66	2.2	8.4	18	15	18	40	74	97	82	36
Starbursts: M82															
B = 50 μG	e^-	H10	4	26	0.44	1.6	6.6	22	20	24	43	65	88	91	18
		15%	4.3	4.8	0.4	1.5	6.1	21	19	22	41	63	86	93	21
		T07	3.8	0.98	0.44	1.6	6.6	23	21	24	43	66	88	91	16
	$e^\pm$	H10	4	26	1.4	5.5	7.7	25	21	24	43	65	88	91	18
		15%	4.3	4.8	1.1	5.9	7.2	23	20	23	41	63	86	93	21
		T07	3.8	0.98	1.3	5.3	7.8	25	22	24	44	66	88	91	16
B = 100 μG	e^-	H10	3.5	39	0.26	1	4.2	15	16	21	44	70	93	95	33
		15%	3.8	7.3	0.23	0.93	3.9	14	15	19	41	68	92	96	40
		T07	3.4	1.5	0.26	1	4.2	15	16	21	44	71	93	95	30
	$e^\pm$	H10	3.5	39	0.92	3.8	5	17	17	22	44	71	93	95	33
		15%	3.8	7.3	0.7	4.1	4.7	16	15	20	42	68	92	96	40
		T07	3.4	1.5	0.87	3.7	5.1	17	17	22	45	72	93	95	30
B = 150 μG	e^-	H10	22	28	0.11	0.43	1.6	5.7	6.2	9	22	39	58	92	52
		15%	25	5.2	0.096	0.39	1.6	5.2	5.7	8.2	20	37	57	90	62
		T07	22	1.1	0.11	0.43	1.6	5.7	6.2	9	22	39	58	91	47
	$e^\pm$	H10	17	34	0.41	1.7	2.4	7.6	7.8	11	26	47	69	97	48
		15%	20	6.5	0.32	1.8	2.3	7.1	7.3	10	25	45	67	96	57
		T07	18	1.3	0.39	1.6	2.4	7.6	7.9	11	27	47	69	97	44
B = 200 μG	e^-	H10	17	27	0.14	0.4	1.2	3.5	3.9	6.6	20	40	65	97	46
		15%	20	5.1	0.13	0.38	1.1	3.2	3.6	5.9	18	38	63	95	55
		T07	18	1	0.14	0.4	1.2	3.5	4	6.6	20	41	65	96	41
	$e^\pm$	H10	17	27	0.2	0.82	1.2	3.7	4.1	6.7	20	40	65	97	45
		15%	20	5.2	0.15	0.88	1.2	3.5	3.8	6	18	38	63	95	55
		T07	17	1	0.19	0.8	1.2	3.8	4.1	6.7	20	41	65	96	41
B = 250 μG	e^-	H10	19	25	0.094	0.29	0.84	2.4	2.8	4.9	16	34	58	95	47
		15%	21	4.7	0.088	0.27	0.83	2.2	2.5	4.4	15	32	56	93	56
		T07	19	0.95	0.094	0.29	0.85	2.4	2.8	5	16	35	58	95	42
	$e^\pm$	H10	18	26	0.14	0.56	0.88	2.6	3	5.2	17	36	60	96	46
		15%	21	4.9	0.11	0.6	0.86	2.4	2.7	4.6	15	34	58	94	55
		T07	18	0.99	0.13	0.55	0.89	2.6	3	5.2	17	36	60	96	42
B = 300 μG	e^-	H10	19	26	0.069	0.23	0.66	1.7	2.2	4.2	15	33	57	95	47
		15%	21	4.9	0.063	0.22	0.66	1.6	1.9	3.7	14	31	55	93	56
		T07	19	0.99	0.068	0.23	0.67	1.8	2.2	4.3	15	33	57	95	42
	$e^\pm$	H10	18	27	0.089	0.37	0.67	1.8	2.3	4.3	15	34	58	95	47
		15%	21	5	0.071	0.39	0.66	1.7	2	3.8	14	32	56	94	56
		T07	19	1	0.085	0.36	0.68	1.8	2.3	4.4	16	34	58	95	42
B = 400 μG	e^-	H10	18	33	0.057	0.26	0.93	3.1	4.1	7.5	24	48	72	97	48
		15%	20	6.2	0.05	0.24	0.9	2.8	3.7	6.7	22	46	71	95	57
		T07	18	1.2	0.056	0.26	0.94	3.1	4.1	7.6	25	49	72	96	43
	$e^\pm$	H10	18	33	0.56	2.3	1.5	4.1	4.5	7.7	25	48	72	96	48
		15%	20	6.2	0.41	2.6	1.5	3.8	4.1	6.9	23	46	70	95	57
		T07	18	1.2	0.52	2.2	1.5	4.1	4.5	7.8	25	49	72	96	43
Starbursts: NGC 253 Core															
B = 50 μG	e^-	H10	6	13	0.22	0.84	3.7	14	14	16	32	53	78	97	30
		15%	6.5	2.4	0.19	0.76	3.4	13	13	15	30	50	76	98	36
		T07	5.8	0.48	0.21	0.85	3.8	14	14	17	32	53	79	97	27
	$e^\pm$	H10	6	13	0.96	3.9	4.7	16	14	17	32	53	78	97	30
		15%	6.5	2.4	0.72	4.3	4.3	15	13	16	31	51	76	98	36
		T07	5.8	0.48	0.9	3.8	4.7	16	15	17	33	53	79	97	27
B = 100 μG	e^-	H10	9.9	19	0.13	0.54	2.4	9.5	10	14	31	54	80	100	45
		15%	11	3.6	0.12	0.49	2.2	8.7	9.7	13	30	52	78	100	53
		T07	9.9	0.72	0.13	0.54	2.4	9.6	11	15	32	55	80	100	41
	$e^\pm$	H10	10	19	0.65	2.7	3.1	11	11	15	31	54	79	100	46
		15%	11	3.5	0.48	3	2.9	9.9	10	14	30	52	77	100	54
		T07	10	0.71	0.61	2.6	3.1	11	11	15	32	55	80	100	42
B = 150 μG	e^-	H10	20	21	0.086	0.36	1.5	5.6	6.4	9.2	22	40	62	94	53
		15%	23	4	0.077	0.33	1.4	5.2	5.8	8.4	21	39	61	93	62
		T07	21	0.81	0.085	0.36	1.5	5.6	6.4	9.2	22	41	63	94	48
	$e^\pm$	H10	20	21	0.39	1.6	1.9	6.4	6.8	9.5	22	41	63	94	53
		15%	23	4	0.29	1.8	1.8	5.9	6.2	8.7	21	39	61	93	62

TABLE 4 — *Continued*

Model	Prim. e[a]	$f_{\rm SB}$[b]	$E_{\rm norm}$[c] GeV	Scale[d]	Maximum fraction of γ-ray background[e]										
					100 keV %	300 keV %	1 MeV %	3 MeV %	10 MeV %	30 MeV %	100 MeV %	300 MeV %	1 GeV %	10 GeV %	100 GeV %
		T07	21	0.81	0.36	1.6	1.9	6.4	6.8	9.5	22	41	63	94	48
$B = 200\ \mu$G	e^-	H10	4.3	21	0.073	0.33	1.5	6.5	8.3	13	35	64	91	99	40
		15%	4.6	4	0.065	0.3	1.4	5.9	7.6	12	33	61	89	99	48
		T07	4.1	0.81	0.073	0.34	1.6	6.6	8.4	14	36	65	91	99	36
	$e^\pm$	H10	4.6	21	0.78	2.7	2.6	8	9	14	35	64	91	99	40
		15%	4.7	4	0.64	3	2.5	7.4	8.2	13	33	61	89	99	48
		T07	4.2	0.8	0.75	2.6	2.6	8	9.1	14	36	65	91	99	36
$B = 250\ \mu$G	e^-	H10	2.9	23	0.24	0.57	1.6	5.1	6.4	11	34	65	93	97	36
		15%	3.2	4.4	0.22	0.55	1.5	4.7	5.8	10	31	62	91	97	43
		T07	2.8	0.9	0.24	0.57	1.6	5.1	6.5	12	35	66	93	97	32
	$e^\pm$	H10	3.3	45	0.41	2.2	1.9	5.4	6.1	10	31	61	91	97	46
		15%	3.5	7.8	0.35	2.3	1.8	5	5.6	9.3	28	59	89	98	53
		T07	3	1.8	0.42	2.1	2	5.5	6.3	11	32	63	92	97	40
$B = 300\ \mu$G	e^-	H10	17	18	0.039	0.18	0.73	2.9	3.9	7	21	43	68	97	46
		15%	20	3.4	0.034	0.17	0.69	2.6	3.5	6.3	20	41	66	96	55
		T07	17	0.69	0.039	0.18	0.73	2.9	3.9	7	22	43	68	97	42
	$e^\pm$	H10	17	18	0.2	0.85	0.94	3.3	4.1	7.2	21	43	68	97	46
		15%	20	3.4	0.15	0.94	0.89	3	3.7	6.4	20	41	66	96	55
		T07	17	0.69	0.19	0.82	0.94	3.3	4.2	7.2	22	44	68	97	42
$B = 400\ \mu$G	e^-	H10	20	13	0.022	0.1	0.36	1.4	2.1	4.4	16	35	59	94	48
		15%	22	2.5	0.019	0.094	0.35	1.2	1.8	3.9	15	33	57	93	58
		T07	20	0.51	0.022	0.1	0.36	1.4	2.1	4.5	16	35	59	94	43
	$e^\pm$	H10	20	13	0.054	0.23	0.4	1.4	2.1	4.5	16	35	59	94	48
		15%	22	2.5	0.042	0.25	0.39	1.3	1.9	3.9	15	33	57	93	58
		T07	20	0.51	0.051	0.23	0.4	1.5	2.1	4.5	16	35	59	94	43

[a] Denotes whether the primary electrons and positrons in the model are all electrons (e^-) or half electrons and half positrons ($e^\pm$).

[b] Starburst fraction used in the model. H10: our low starburst fraction case, with the starburst fraction in the Hopkins et al. (2010) semianalytic models; 15%: our fiducial medium starburst fraction case, where 15% of the cosmic star formation rate at all z is in starbursts; T07: our high starburst fraction case, using the values in Thompson, Quataert, & Waxman (2007).

[c] The energy where the ratio of the predicted γ-ray background to the observed γ-ray background reaches its maximum.

[d] Maximum allowed scaling of the predicted γ-ray background for that model that does not overproduce the observed γ-ray background; it is simply the reciprocal of the maximum ratio of the predicted γ-ray background to the observed γ-ray background.

[e] Maximum fraction of the γ-ray background at each energy allowed by the spectral shape of each model. It reaches 100% at $E_{\rm norm}$.